

Ph.D. Dissertation



**International Doctoral School in Information
and Communication Technology**

DISI - University of Trento

SVM-BASED STRATEGIES AS APPLIED TO
ELECTROMAGNETICS

Federico Viani

Advisor:
Andrea Massa, Professor
Università degli Studi di Trento

December 2010

Acknowledgements

I would like to express my deep and sincere gratitude to Professor Andrea Massa. His wide knowledge and his logical way of thinking have been, and will be, of great value for me.

I would also thank all the friends and colleagues I met during my PhD for their kind help and guidance.

My special gratitude is due to my family for the loving support. They are a role model for me to follow unconsciously and always will be my best counselors.

Finally, I have no suitable words that can fully describe how to thank Silvia for her support during these years, I am sure that life would not be so coloured without her constant presence.

Abstract

In the framework of the electromagnetic approaches based on learning-by-example (LBE) techniques, this thesis focuses on the development of a strategy for the solution of complex problems by means of support vector machine (SVM). The proposed instance-based classification method compared to more traditional optimization techniques solves the arising quadratic optimization problem with constraints in a simple and reliable way leveraging on the Statistical Learning Theory which permits the design of optimal classifiers with a solid theoretical framework. A set of input/output relations representing the training dataset permits to avoid the a-priori knowledge about the system. By exploiting the generalization capabilities, the robustness against noise and the real-time performance, this technique has been proven to be suitable for more than one real-world application. The investigated problems are addressed by integrating the measured electromagnetic field with a suitably defined classifier that is aimed at defining a real-time reconstruction of the observed domain. For each application field a set of numerical results have been reported in order to assess the effectiveness and flexibility of the proposed approach. The real-time capabilities as well as the feasibility when dealing with real data have been also verified by means of an experimental setup for the passive tracking of non-cooperative targets moving throughout the investigated area.

Keywords

Learning by example (LBE), support vector machine (SVM), buried object detection, breast cancer imaging, direction of arrival (DOA) estimation, passive localization and tracking.

Published Journals Papers

- [R1] F. Viani, L. Lizzi, P. Rocca, M. Benedetti, M. Donelli, and A. Massa, "Object tracking through RSSI measurements in wireless sensor networks," *Electron. Lett.*, vol. 44, no. 10, pp. 653654, May 2008.
- [R2] M. Donelli, F. Viani, P. Rocca, and A. Massa, "An innovative multi-resolution approach for DOA estimation based on a support vector classification," *IEEE Transactions on Antennas and Propagation*, vol. 57, no. 8, pp. 2279-2292, August 2009.
- [R3] F. Viani, P. Rocca, M. Benedetti, G. Oliveri, and A. Massa, "Electromagnetic passive localization and tracking of moving targets in a WSN-infrastructure environment," *Inverse Problems*, vol. 26, pp. 1-15, 2010.
- [R4] F. Viani, M. Donelli, P. Rocca, G. Oliveri, D. Trincherò, and A. Massa, "Localization, Tracking, and Imaging of Targets in Wireless Sensor Networks," *Radio Science*, (submitted 20/11/2010).
- [C1] F. Viani, G. Oliveri, and A. Massa, "Real-time tracking of transceiver-free objects for homeland security," *Proc. European Microw. Conf. (EuMC 2009)*, Rome, Italy, Sept. 29 2009-Oct. 1 2009, pp. 1892-1895.
- [C2] F. Viani, M. Donelli, P. Rocca, A. Massa, "A SVM-based three-dimensional multi-resolution approach for biomedical inverse scattering problems," *PIERS 2008 in Hangzhou*, Hangzhou, China, p. 866, March 24-28, 2008.
- [C3] F. Viani, M. Donelli, P. Rocca, R. Azaro, and A. Massa, "A multi-resolution three-dimensional approach based on SVM for breast cancer detection," *24th International Review of Progress in Applied Computational Electromagnetics*, ACES 2008, Niagara Falls, Canada, pp. 479-482, March 30-April 04, 2008.
- [C4] P. Rocca, F. Viani, M. Donelli, M. Benedetti, and A. Massa, "An integration between SVM classifiers and multi-resolution techniques for

-
- early breast cancer detection,” *Proc. 2008 IEEE AP-S International Symposium*, San Diego, USA, July 5-11, 2008.
- [C5] F. Viani, M. Martinelli, L. Ioriatti, L. Lizzi, G. Oliveri, P. Rocca, and A. Massa, “Real-time indoor localization and tracking of passive targets by means of wireless sensor networks,” *Proc. 2009 IEEE AP-S International Symposium*, Charleston, SC, USA, June 1-5, 2009.
- [C6] F. Viani, P. Meaney, P. Rocca, R. Azaro, M. Donelli, G. Oliveri, and A. Massa, “Numerical validation and experimental results of a multi-resolution SVM-based classification procedure for breast imaging,” *Proc. 2009 IEEE AP-S International Symposium*, Charleston, SC, USA, June 1-5, 2009.
- [C7] L. Lizzi, F. Viani, P. Rocca, G. Oliveri, M. Benedetti, and A. Massa, “Three- dimensional real-time localization of subsurface objects - From theory to experimental validation,” *Proc. 2009 IEEE International Symposium on Geoscience and Remote Sensing*, Cape Town, South Africa, pp. 121-124, July 13-17, 2009.
- [C8] F. Viani, M. Martinelli, L. Ioriatti, M. Benedetti, and A. Massa, “Passive real- time localization through wireless sensor networks,” *Proc. 2009 IEEE International Symposium on Geoscience and Remote Sensing*, Cape Town, South Africa, pp. 718- 721, July 13-17, 2009.
- [C9] F. Viani, G. Oliveri, M. Donelli, L. Lizzi, P. Rocca, and A. Massa, “WSN- based solutions for security and surveillance,” *40th European Microwave Conference 2010 (EuMC2010)*, Paris, France, pp. 1762-1765, September 26 - October 1, 2010.
- [C10] L. Lizzi, M. Pastorino, F. Viani, and A. Massa, “3D Electromagnetic subsurface imaging by means of a multi-resolution classification approach,” *2010 International Symposium on Electromagnetic Theory (EMTS 2010)*, Berlin, Germany, pp. 175- 178, August 16-19, 2010.

Contents

1	Introduction and State-of-the-Art	1
2	SVM-based Methodology	5
2.1	Definition of the Decision Function	6
2.2	Mapping of the Decision Function into the <i>A-Posteriori</i> Probability	8
3	Three-dimensional Buried Object Detection	11
3.1	Introduction	12
3.2	Mathematical Formulation	13
3.2.1	IMSA-3D SVM-based procedure	15
3.3	Numerical Results	18
3.3.1	SVM training and parameter selection	18
3.3.2	Numerical validation of the IMSA-3D procedure	20
3.3.3	Detection of multiple objects	25
3.3.4	Complex scenarios	30
3.4	Conclusions	31
4	Early Breast Cancer Imaging	33
4.1	Introduction	34
4.2	Numerical Model	36
4.3	Multi-resolution SVM-based approach	37
4.3.1	SVM Training phase	37
4.3.2	Multi-resolution Test Phase	39
4.4	Numerical Results	42
4.4.1	Training Set and Model Selection	42
4.4.2	Single Inclusion - <i>Numerical Assessment</i>	44
4.4.2.1	Validation with Random Noise added to Synthetic Data	46
4.4.2.2	Validation with Different Breast Properties	49
4.4.3	Multiple Inclusions - <i>Performance analysis</i>	50
4.5	Conclusions	51

5	Direction of Arrival Estimation	55
5.1	Introduction	56
5.2	Mathematical Formulation	58
5.3	Numerical Simulations and Results	63
5.3.1	<i>Single Signal Scenario</i> - Comparative Assessment	65
5.3.2	Complex Scenarios - Performance Analysis	71
5.3.3	Dipole Array Antenna	82
5.4	Conclusions	84
6	Real-Time Passive Localization and Tracking	87
6.1	Introduction	88
6.2	Mathematical Formulation	90
6.3	Experimental Validation	92
6.3.1	Single target tracking	96
6.3.2	Multiple target tracking	97
6.4	Discussions	100
7	Conclusions and Future Developments	105

List of Tables

3.1	<i>Single buried object, $N = 1$ - Statistics of the performance indexes (object-localization-error v and volume-occupation ξ) for BARE and IMSA approaches.</i>	23
4.1	<i>Multiple detection - Averaged error figures when applying IMSA and BARE with noisy data.</i>	52
5.1	<i>Statistics of the averaged performance indexes ($\hat{\varsigma} = \sum_{i=1}^I \varsigma^{(i)}$ and $\hat{\psi} = \sum_{i=1}^I \psi^{(i)}$) for different signal configurations ($I = 1, 2, 3, 4$).</i>	68
5.2	<i>Single signal scenario, $I = 1$ - Comparative assessment. Values of the location index ς when applying IMSA – DOA, SVR, MUSIC, and ESPRIT.</i>	69
5.3	<i>Multiple signals scenario, $I = 2$. Performance indexes when applying IMSA – DOA, single-step SVM, multi layer perceptron (MLP) neural network, and radial basis function (RBF) neural network.</i>	74
5.4	<i>Multiple signals scenario, $I = 3$ (Configuration 1/1/1). Performance indexes when applying IMSA – DOA, single-step SVM, multi layer perceptron (MLP) neural network, and radial basis function (RBF) neural network.</i>	75
5.5	<i>Multiple signals scenario, $I = 4$ (Configuration 1/1/1/1). Performance indexes when applying IMSA – DOA, single-step SVM, multi layer perceptron (MLP) neural network, and radial basis function (RBF) neural network.</i>	75
5.6	<i>Multiple signals scenario, $I = 4$ (Configuration 2/2). Performance indexes when applying IMSA – DOA, single-step SVM, multi layer perceptron (MLP) neural network, and radial basis function (RBF) neural network.</i>	77
5.7	<i>Multiple signals scenario, $I = 4$ (Configuration 1/3). Performance indexes when applying IMSA – DOA, single-step SVM, multi layer perceptron (MLP) neural network, and radial basis function (RBF) neural network.</i>	80

5.8	<i>Multiple signals scenario, $I = 18$ (Clustered Distribution)</i> . Performance indexes when applying <i>IMSA – DOA</i> , single-step <i>SVM</i> , multi layer perceptron (<i>MLP</i>) neural network, and radial basis function (<i>RBF</i>) neural network.	80
6.1	<i>Single target tracking</i> - Localization errors for the outdoor and the indoor scenarios.	99
6.2	<i>Multiple target localization - Outdoor Scenario</i> - Localization errors for the single and multiple target case.	100

List of Figures

3.1	Three-dimensional geometry.	13
3.2	<i>RoIs</i> identification at step $m = 1$ [with $k = 0$ (<i>a</i>) and $k = 1$ (<i>b</i>)] and $m = 2$ [with $k = 0$ (<i>c</i>) and $k = 1$ (<i>d</i>)].	15
3.3	<i>SVM training</i> - Number of support vectors (SVs) (<i>a</i>) and bounded support vectors (BSVs) (<i>b</i>) versus the SVM hyperparameters.	19
3.4	<i>IMSA-3D Procedure</i> - Probability map determined by the <i>IMSA</i> procedure at $m = 1$ (<i>a</i>), $m = 2$ (<i>b</i>), $m = 3$ (<i>c</i>) and $m = M_{opt} = 4$ (<i>d</i>) for single buried object ($N = 1$).	21
3.5	<i>IMSA-3D Procedure</i> - Performance indexes $v_1^{(m)}$ and $\xi_n^{(m)}$ versus the multi-resolution steps for single buried object ($N = 1$).	23
3.6	<i>IMSA-3D Procedure</i> - Probability map obtained with <i>IMSA-3D</i> approach in absence of buried objects ($N = 0$).	24
3.7	<i>IMSA-3D vs BARE</i> - Probability map determined by the <i>BARE</i> approach for $N = 1$ buried object.	24
3.8	<i>Numerical validation vs noise level</i> - Object-localization-error (<i>a</i>) and volume-occupation (<i>b</i>) determined by the <i>BARE</i> and <i>IMSA-3D</i> <i>3D</i> procedures versus the additive noise amplitude P_N	26
3.9	<i>Numerical validation vs noise level</i> - Probability maps determined by the <i>BARE</i> (<i>a</i>) and <i>IMSA-3D</i> (<i>b</i>) procedures with Noisy data [$P_N = 0.1 V/m$].	27
3.10	<i>Numerical validation vs number of objects</i> - Object-localization- error (<i>a</i>) and volume-occupation (<i>b</i>) determined by the <i>BARE</i> and <i>IMSA-3D</i> procedures versus the number of objects $n = 1, 2, 3$ with noisy data [$P_N = 0.1 V/m$].	28
3.11	<i>Numerical validation vs number of objects</i> - Probability maps de- termined by the <i>IMSA-3D</i> procedures for multiple objects [$N = 2$ <i>BARE</i> (<i>a</i>), <i>IMSA</i> (<i>b</i>) and $N = 3$ <i>BARE</i> (<i>c</i>), <i>IMSA</i> (<i>d</i>)] with noisy data [$P_N = 0.1 V/m$].	29
3.12	<i>Complex scenario</i> - Probability maps determined by the <i>IMSA-3D</i> [$m = M_{opt} = 3$] approach with small objects ($N = 2$) buried in dry sandy soil (<i>a</i>) and dry clay soil (<i>b</i>).	30

LIST OF FIGURES

4.1	Three-dimensional model geometry (a) and top view of the multi-view measurement system (b).	35
4.2	<i>IMSA Procedure</i> - AoI detection at $s = 1$ (a) and $s = 2$ (b) multi-resolution steps.	40
4.3	<i>SVM Parameter Calibration</i> - Support vector N_{NSV} and bounded support vector N_{BSV} analysis vs SVM Hyperparameters.	43
4.4	<i>IMSA Procedure</i> - Mean localization error and volume estimation vs multi-resolution steps (a) in comparison with BARE procedure (b).	45
4.5	<i>IMSA Procedure</i> - Pathology detection obtained by <i>IMSA</i> procedure at $s = 1$ (a), $s = 2$ (b), $s = 3$ (c).	47
4.6	<i>IMSA vs BARE Detection</i> - Pathology detection determined by <i>BARE</i> procedure.	48
4.7	<i>Validation vs random noise</i> - Localization error and volume estimation versus transmission power P_{tx} (-100 dBm noise floor)	48
4.8	<i>Validation vs random noise</i> - Pathology detection determined by <i>IMSA</i> procedure with noisy data [$P_{tx} = 30$ dBm (a), $P_{tx} = 25$ dBm (b), $P_{tx} = 15$ dBm (c), $P_{tx} = 10$ dBm (d)].	49
4.9	<i>Validation vs electrical properties of breast</i> - Localization error and volume estimation versus breast complex dielectric characteristics (<i>F-H-S</i>).	50
4.10	<i>Multiple detection</i> - Pathology detections determined by <i>IMSA</i> procedure at $s = 1$ (a), $s = 2$ (b), $s = 3$ (c) and by <i>BARE</i> approach (d).	51
5.1	Planar array geometry.	58
5.2	<i>IMSA-DOA Procedure</i> - Angular region partitioning and <i>ARoIs</i> identification at the steps $s = 1$ (a) and $s = 2$ (b).	60
5.3	<i>Single signal scenario</i> , $I = 1$ - Probability map determined by the <i>IMSA-DOA</i> procedure at: (a) $s = 2$, (b) $s = S_{opt} = 4$	64
5.4	<i>Single signal scenario</i> , $I = 1$ - Probability maps obtained with different classification approaches: (a) single-step <i>SVM</i> , (b) multi layer perceptron (<i>MLP</i>) neural network, and (c) radial basis function (<i>RBF</i>) neural network [$\Delta\theta = 1.25^\circ$ and $\Delta\phi = 5^\circ$].	67
5.5	<i>Single signal scenario</i> , $I = 1$ - Uniform (red points) and non-uniform (green triangles) angular training sets.	70
5.6	<i>Single signal scenario</i> , $I = 1$ - Behavior of the location index versus the number of failed array elements.	71
5.7	<i>Multiple signals scenario</i> , $I = 2$ - Probability maps obtained with different classification approaches: <i>IMSA-SVM</i> [(a) $s = 1$, (b) $s = 2$, (c) $s = S_{opt} = 3$], [$\Delta\theta = \Delta\theta_{(2)}^{(3)} = 2.5^\circ$ and $\Delta\phi = \Delta\phi_{(2)}^{(3)} = 10^\circ$].	72

5.8	<i>Multiple signals scenario, $I = 2$ - (d) single-step SVM, (e) multi layer perceptron (MLP) neural network, and (f) radial basis function (RBF) neural network [$\Delta\theta = \Delta\theta_{(2)}^{(3)} = 2.5^\circ$ and $\Delta\phi = \Delta\phi_{(2)}^{(3)} = 10^\circ$].</i>	73
5.9	<i>Multiple signals scenario, $I = 3$ (Configuration 1/1/1) - Probability maps obtained with different classification approaches: (a) IMSA – SVM [$s = S_{opt} = 3$] and (b) single-step SVM [$\Delta\theta = \Delta\theta_{(2)}^{(3)}$ and $\Delta\phi = \Delta\phi_{(2)}^{(3)}$].</i>	76
5.10	<i>Multiple signals scenario, $I = 4$ - Probability maps obtained with the IMSA – SVM. Configuration 1/1/1/1: step (a) $s = 1$, (b) $s = 2$, and (c) $s = S_{opt} = 3$.</i>	78
5.11	<i>Multiple signals scenario, $I = 4$ - Configuration 2/2: step $s = S_{opt} = 3$ (d); Configuration 1/3: step $s = S_{opt} = 3$ (e).</i>	79
5.12	<i>Multiple signals scenario ($I = 18$ - Clustered Distribution) - Probability maps obtained with different classification approaches: (a) IMSA – SVM ($s = S_{opt} = 3$), (b) single-step SVM, (c) multi layer perceptron (MLP) neural network, and (d) radial basis function (RBF) neural network [$\Delta\theta = \Delta\theta_{(2)}^{(3)}$ and $\Delta\phi = \Delta\phi_{(2)}^{(3)}$].</i>	81
5.13	<i>Multiple signals scenario ($I = 18$ - Sparse Distribution) - Probability maps determined by the IMSA – SVM at the convergence ($s = S_{opt} = 2 - \Delta\theta_{(1)}^{(2)} = 5^\circ$ and $\Delta\phi_{(1)}^{(2)} = 20^\circ$).</i>	82
5.14	<i>No-signals scenario [$I = 0$; $P_n = 20$ dB (Test Set) - $P_n = 0$ dB (Training Set)] - Probability maps obtained with different classification approaches: (a) IMSA – SVM ($s = S_{opt} = 1$), (b) multi layer perceptron (MLP) neural network, and (c) radial basis function (RBF) neural network.</i>	83
5.15	<i>Dipole Array, $I = 1$ - Probability map determined by the IMSA – DOA [$s = S_{opt} = 4$].</i>	84
5.16	<i>Dipole Array, $I = 2$ - Probability map determined by the IMSA – DOA when (a) $I_1 = (\theta_1 = 12^\circ, \phi_1 = 165^\circ)$, $I_2 = (\theta_2 = 82^\circ, \phi_2 = 165^\circ)$ [$s = S_{opt} = 3$] and (b) $I_1 = (\theta_1 = 30^\circ, \phi_1 = 60^\circ)$, $I_2 = (\theta_2 = 30^\circ, \phi_2 = 300^\circ)$ [$s = S_{opt} = 3$].</i>	85
6.1	<i>Equivalent Tracking Problem - Sketch of (a) the tracking scenario and (b) the equivalent inverse problem.</i>	89
6.2	<i>Problem Geometry - Plots of (a) the outdoor and (b) the indoor environments with WSN-based tracking system.</i>	93
6.3	<i>Calibration - Localization error as a function of the SVM control parameters: T ($\lambda = 100, C = 60$), λ ($T = 500, C = 60$), and C ($T = 500, \lambda = 100$).</i>	94
6.4	<i>Single target localization - Outdoor Scenario - Probability maps of the investigation region D obtained when the test data (a) belongs and (b) does not belong to the training data set.</i>	95

LIST OF FIGURES

6.5	<i>Single target localization - Indoor Scenario</i> - Probability maps of the investigation region D obtained when the test data (a) belongs and (b) does not belong to the training data set.	96
6.6	<i>Single target tracking - Outdoor Scenario</i> - Actual and estimated trajectories.	97
6.7	<i>Single target tracking - Outdoor Scenario</i> - Screenshots of the probability map of the investigation region D acquired during the target motion.	98
6.8	<i>Single target tracking - Indoor Scenario</i> - Actual and estimated trajectories.	99
6.9	<i>Single target localization - Outdoor Scenario</i> ($T_1 \in [0, 500]$, $T_2 \in [0, 500]$, $\lambda = 100$, $C = 60$) - Probability maps of the investigation region D when using (a) 100% T_1 and 0% T_2 , (b) 80% T_1 and 20% T_2 , (c) 60% T_1 and 40% T_2 , (d) 40% T_1 and 60% T_2 , (e) 20% T_1 and 80% T_2 , and (f) 0% T_1 and 100% T_2 of samples in the training phase.	101
6.10	<i>Multiple targets localization - Outdoor Scenario</i> ($T_1 \in [0, 500]$, $T_2 \in [0, 500]$, $\lambda = 100$, $C = 60$) - Probability maps of the investigation region D when using (a) 100% T_1 and 0% T_2 , (b) 80% T_1 and 20% T_2 , (c) 60% T_1 and 40% T_2 , (d) 40% T_1 and 60% T_2 , (e) 20% T_1 and 80% T_2 , and (f) 0% T_1 and 100% T_2 of samples in the training phase.	102
6.11	<i>Multiple targets tracking - Outdoor Scenario</i> - Actual and estimated trajectories.	103
6.12	<i>Multiple targets tracking - Outdoor Scenario</i> - Actual and estimated trajectories.	103

LIST OF FIGURES

Structure of the Thesis

The thesis is structured in chapters according to the organization detailed in the following.

The first chapter deals with an introduction to the thesis, focusing on the main motivations and on the subject of this work as well as a presentation of the state-of-the-art techniques dealing with the solution of electromagnetic problems by means of learning-by-example strategies.

Chapter 2 presents the theoretical background of the SVM-based classifier, focusing on the definition of the decision function as well as on the evaluation of the a-posteriori probability.

In Chapter 3 the proposed method is integrated with an iterative multi-scaling approach for the detection of three-dimensional buried object. The flexibility and effectiveness of such an approach are pointed out in the numerical validation for both single and multiple objects.

The customization of the approach for the early breast cancer imaging problem is described and assessed in Chapter 4 as an alternative technique looking for real-time processing. Preliminary results are presented in case of noiseless and noisy data.

Chapter 5 deals with the presentation of the direction of arrival estimation problem. The *SVM*-based approach has been used to estimate the *DOA* of each electromagnetic wave impinging on a planar antenna array.

LIST OF FIGURES

The passive detection and tracking of non-cooperative moving targets is presented in Chapter 6. The presented results show the effectiveness and the real-time capabilities of the proposed approach when dealing with real data acquired in time-varying scenarios.

Conclusions and further developments are presented in Chapter 7.

Chapter 1

Introduction and State-of-the-Art

In this chapter, a brief overview on the techniques presented in the state-of-the-art and regarding the solution of complex electromagnetic problems by means of learning-by-example methodologies is presented. Accordingly, the motivation of the thesis is pointed out.

The learning methodology has been inspired by theory of statistical learning leading up to solutions with nice mathematical properties and excellent performance. Machine learning has largely been applied to a variety of actual problems but less attention has been devoted in the field of electromagnetics. When closed form solutions do not exist, learning by example approaches represent an alternative way to solve the problem at hand. By training an SVM [1] the solution can be online predicted. To this end, when the application requires real-time performance, the use of a mathematical tool that can be trained off-line and then easily implemented in embedded devices is suggested. These properties and also other characteristics make SVM good candidate to solve optimization problems in electromagnetic areas, such as inverse scattering problems. Due to their inherent nonlinear nature and ill-posedness, the solution to inverse problems is very complex. State of the art algorithms recast the original problem into an optimization one, which is successively solved by means of iterative minimization techniques [2, 3]. Unfortunately, such procedures often make the reconstruction process unsuitable for real-time applications. Great attention has been devoted to alternative methodology based on neural networks (NNs), both multilayer perceptron (MLP) [4] and radial basis function (RBF) [5] approaches have been proposed. However, even if they show low computational complexity, NN-based approaches suffer from typical training dependent problems like overfitting resulting in an inability to correctly estimate the output in presence of input data which do not belong to the original training set. On the contrary, SVMs allow the control of the approximating function and its generalization accuracy. More in detail, the arising optimization problem is aimed at finding the best tradeoff between the learning capabilities from training data and the model complexity. Since the model complexity has a straightforward consequence on the generalization accuracy [6], this leads to the determination of models that outperform standard NNs. In [37], a SVM-based technique has been adopted for the localization of a two-dimensional cylindrical geometry with circular cross-section. The localization problem has been recast in a regression one where the unknowns (i.e., the position as well as the geometric and dielectric characteristics of the target) are directly evaluated from the data (i.e., the values of the scattered field) by approximating the data-unknowns relation through an off-line data fitting process (training phase). This approach turns out to be effective for the detection of few object since some difficulties occur when dealing with a large number of unknowns. In order to overcome this drawback, Massa et al. [38] proposed a classification approach, instead of a regression one, that moves from the detection of a single object to the definition of an a-posteriori probability of presence of objects in a two-dimensional scenario. In order to define the risk-map, during the test phase, the domain under investigation will be partitioned in a two-dimensional lattice in order to classify a finite number of cells. The prediction model tests the unknown input data and returns the estimation of the cell states, that can be empty (i.e., if any scatterer belongs to the cell) or

occupied. Unlike standard approaches that only classify the input pattern, the proposed output defines the a posteriori probability that the object belongs to a particular region of the domain. In this sense, the computational time saving provided by this methodology justifies some limitations like the estimation of the objects presence or absence instead of the complex dielectric properties. Starting from this theoretical background, the proposed approach is aimed at solving complex problems starting from the field of three-dimensional inverse scattering problems, the real-time direction finding of signals impinging on a planar array of electromagnetic sensors, up to the passive localization and tracking of targets moving throughout an area monitored by a wireless sensor network (WSN) architecture.

Chapter 2

SVM-based Methodology

This chapter presents the theoretical background of the proposed probabilistic approach for the definition of the risk map of object presence and position in the investigated domain. Starting from the measurement of an electromagnetic quantity related to the considered application, the probability of occurrence of targets is determined through a suitably defined classifier based on a Support Vector Machine (SVM). The proposed SVM-based classification approach is formulated as a two-step procedure

- *Step 1:* determining a decision function $\hat{\Phi}$ that correctly classifies an input pattern $(\underline{\Gamma}_E, m)$ (not-necessarily belonging to the training set);
- *Step 2:* mapping the decision function $\hat{\Phi}\{(\underline{\Gamma}_E, m)\}$ into an *a-posteriori* probability $Pr\{\underline{\chi} = \underline{1} | \underline{\Gamma}_E\}$.

The details of the procedure are mathematically formulated in the following sections.

2.1 Definition of the Decision Function

At this step, the status χ_m of each cell of the lattice has to be determined. Mathematically, such a problem formulates in the definition of a suitable discriminant function $\hat{\Phi}$ separating the two classes, which are labeled as $\chi = +1$ and $\chi = -1$. Since these classes are non-linearly separable, the definition of a non-linear (in terms of the original data $\underline{\Gamma}_E$) discriminant function is usually required as well as the solution of an optimization problem where multiple optima (also local optima) are present. As a matter of fact, such a solution is implemented when Artificial Neural Networks (ANN) are considered (see [84] and the references cited therein).

Unlike ANN, SVM defines a linear decision function corresponding to a hyperplane that maximizes the separating margin between the classes and it requires the solution of an optimization problem where only one minimum there exists. More in detail, the linear data-fitting is not carried out in the original input space $\Re\{\underline{\Gamma}_E\}$, but in a higher dimensional space $\aleph\{\underline{\varphi}(\underline{\Gamma}_E)\}$ (called *feature space*) where the original examples are mapped through a non-linear operator⁽¹⁾¹, $\underline{\varphi}(\bullet)$. The nonlinear SVM classifier so obtained is defined as

$$\hat{\Phi}(\underline{\varphi}(\underline{\Gamma}_E, m)) = \underline{w} \cdot \underline{\varphi}(\underline{\Gamma}_E, m) + b \quad m = 1, \dots, M \quad (2.1)$$

where \underline{w} and b are the parameters of $\hat{\Phi}$ to be determined during the training phase. The hyperplane so-defined causes the largest separation between the decision function values for the “margin” training examples from the two classes. Mathematically, such a hyperplane can be found by minimizing the following cost function

$$\Omega(\underline{w}) = \frac{1}{2} \|\underline{w}\|^2 \quad (2.2)$$

subject to the separability constraints

$$\begin{aligned} \underline{w} \cdot \underline{\varphi}(\underline{\Gamma}_E^{(n)}, m) + b &\geq +1 \quad \text{for} \quad \chi_m^{(n)} = +1 \quad m = 1, \dots, M \\ \underline{w} \cdot \underline{\varphi}(\underline{\Gamma}_E^{(n)}, m) + b &\leq -1 \quad \text{for} \quad \chi_m^{(n)} = -1 \quad n = 1, \dots, N \end{aligned} \quad (2.3)$$

In this sense, SVM can be considered as a kind of regularized network, as indicated in [8].

However, since the training data in the feature space are generally non-completely separable by a hyperplane, *slack variables* (denoted by $\xi_{(m)}^{(n)}$) are introduced to relax the separability constraints in (2.3) as follows

$$\begin{aligned} \underline{w} \cdot \underline{\varphi}(\underline{\Gamma}_E^{(n)}, m) + b &\geq 1 - \xi_{(m)+}^{(n)} \quad \text{for} \quad \chi_m^{(n)} = 1 \quad m = 1, \dots, M \\ \underline{w} \cdot \underline{\varphi}(\underline{\Gamma}_E^{(n)}, m) + b &\leq \xi_{(m)-}^{(n)} - 1 \quad \text{for} \quad \chi_m^{(n)} = -1 \quad n = 1, \dots, N \end{aligned} \quad (2.4)$$

¹⁽¹⁾Because of the formulation of the problem at hand, it is easy to verify [Eq. (2.9)] that actually one does not need to know the $\underline{\varphi}(\bullet)$ function, but only its dot product in the feature space according to the so-called “*kernel trick*” [1].

Such a procedure is justified by the Cover's theorem, a key point in the SVM methodology as indicated in [1] (p. 200).

Thus, the cost function in (2.2) turns out to be

$$\Omega(\underline{w}) = \frac{\|\underline{w}\|^2}{2} + \frac{C}{\sum_{m=1}^M \{N_{(m)}^- + N_{(m)}^+\}} \sum_{m=1}^M \left\{ \sum_{n=1}^{N_{(m)}^+} \xi_{(m)+}^{(n)} + \sum_{n=1}^{N_{(m)}^-} \xi_{(m)-}^{(n)} \right\} \quad (2.5)$$

where $N_{(m)}^+$ and $N_{(m)}^-$ indicate the number of training patterns for which $\chi_m^{(n)} = +1$ and $\chi_m^{(n)} = -1$, respectively. The user-defined hyperparameter C controls the trade-off between the *empirical risk* (i.e., the training errors) and the model complexity [the first term in (2.6)] to avoid the *overfitting*. In that case, the decision boundary too precisely corresponds to the training data. Thereby, the method is unable to deal with data outside the training set [1] (Ch. 5 and Ch. 7).

Moreover, to include *a-priori* knowledge about class distributions [9], two weighting constants can be defined $\lambda_+ = \frac{C}{\sum_{m=1}^M N_{(m)}^+}$ and $\lambda_- = \frac{C}{\sum_{m=1}^M N_{(m)}^-}$ [102], and Eq. (2.5) modifies as follows

$$\Omega(\underline{w}) = \frac{\|\underline{w}\|^2}{2} + \lambda_+ \sum_{m=1}^M \sum_{n=1}^{N_{(m)}^+} \xi_{(m)+}^{(n)} + \lambda_- \sum_{m=1}^M \sum_{n=1}^{N_{(m)}^-} \xi_{(m)-}^{(n)} \quad (2.6)$$

In order to minimize (2.6), it can be observed that a necessary condition is that \underline{w} is a linear combination of the mapped vectors $\underline{\varphi}(\underline{\Gamma}_E^{(n)}, m)$

$$\underline{w} = \sum_{m=1}^M \sum_{n=1}^N \left\{ \alpha_m^{(n)} \chi_m^{(n)} \underline{\varphi}(\underline{\Gamma}_E^{(n)}, m) \right\} \quad (2.7)$$

where $\alpha_m^{(n)} \geq 0$, $n = 1, \dots, N$, $m = 1, \dots, M$ are Lagrange multipliers to be determined. Moreover, from the Karush-Khun-Tucker conditions at the optimality [11], b turns out to be expressed as follows

$$b = \frac{\sum_{m=1}^M \sum_{n=1}^{N_{sv}} \left\{ \chi_m^{(n)} - \sum_{q=1}^M \sum_{p=1}^N \left\{ \alpha_m^{(p)} \underline{\varphi}(\underline{\Gamma}_E^{(n)}, m) \cdot \underline{\varphi}(\underline{\Gamma}_E^{(p)}, q) \right\} \right\}}{N_{sv}} \quad (2.8)$$

N_{sv} being the number of patterns $(\underline{\Gamma}_E^{(n)}, m)$ for which $\alpha_m^{(n)} \neq 0$ (called *support vectors*). Since support vectors lie on the hyperplane for which Eq. (2.4) is satisfied with equality, they are taken into account for the classification while the others are neglected. Such an event reflects the "sparsity" property of the SVM classifier allowing the use of few input patterns.

2.2. MAPPING OF THE DECISION FUNCTION INTO THE *A-POSTERIORI* PROBABILITY

Substituting (2.7) and (2.8) in (2.1) yields

$$\hat{\Phi}(\underline{\varphi}(\underline{\Gamma}_E), m) = \sum_{p=1}^M \sum_{n=1}^N \left\{ \alpha_m^{(n)} \chi_m^{(n)} \Theta(\underline{\Gamma}_E^{(n)}, \underline{\Gamma}_E, p, m) \right\} + \frac{\sum_{m=1}^M \sum_{n=1}^{N_{sv}} \left\{ \chi_m^{(n)} - \sum_{q=1}^M \sum_{p=1}^N \left\{ \alpha_m^{(p)} \Theta(\underline{\Gamma}_E^{(n)}, \underline{\Gamma}_E^{(p)}, p, m) \right\} \right\}}{N_{sv}} \quad (2.9)$$

where $\Theta(\underline{\Gamma}_E^{(i)}, \underline{\Gamma}_E^{(j)}, p, m) = \underline{\varphi}(\underline{\Gamma}_E^{(i)}, p) \cdot \underline{\varphi}(\underline{\Gamma}_E^{(j)}, m)$ is a suitable *kernel function* [12]. Then, the decision function is completely determined when the Lagrange multipliers are computed. Towards this end, the constrained optimization problem formulated in (2.6) and (2.4) is reformulated in a more practical dual form. The solution of the dual problem, which is equivalent to the solution of the primal optimization problem (2.2)-(2.3), turns out to be

$$\max_{\underline{\alpha}} \left\{ \frac{\max_{\underline{\alpha}} \{ \Omega_{Dual}(\underline{\alpha}) \}}{2} - \sum_{n=1}^N \sum_{m=1}^M \alpha_m^{(n)} \right\} \quad (2.10)$$

subject to $\sum_{n=1}^N \sum_{m=1}^M \alpha_m^{(n)} \chi_m^{(n)} = 0$, $\alpha_m^{(n)} \in [0, \lambda_-]$ if $\chi_m^{(n)} = -1$ and $\alpha_m^{(n)} \in [0, \lambda_+]$ otherwise.

Finally, since $\Omega_{Dual}(\underline{\alpha})$ is a convex and quadratic function of the unknown parameters $\alpha_m^{(n)}$, it is solved numerically by means of a standard quadratic programming technique (e.g., the Platt's SMO algorithm for classification [13]⁽²⁾). More in detail, the SMO algorithm breaks the large optimization problem at hand in a series of smaller ones characterized by only two variables and solved through an effective updating formula [13], thus inducing non-negligible computational savings.

2.2 Mapping of the Decision Function into the *A-Posteriori* Probability

Concerning standard classification, the SVM classifier labels an input pattern according to the following rule [14]

$$\chi_m = \text{sign} \left\{ \hat{\Phi}(\underline{\varphi}(\underline{\Gamma}_E), m) \right\} \quad m = 1, \dots, M \quad (2.11)$$

Unlike standard approaches, the proposed method is aimed at defining an *a-posteriori* probability. Consequently, some modifications to the standard SVM-based classification approach are needed. Towards this aim, a set of efficient solutions has been proposed (see, for instance, [12],[15]-[17]) either based on

²⁽²⁾An optimal implementation of the SMO algorithm is the “*LibSVM*” tool available at <http://www.kernel-machines.org>.

a direct training of the SVM with a logistic link function and a regularized maximum likelihood score or based on *a-posteriori* fitting probability process. The first class of approaches usually leads to non-sparse kernel machines and requires a significant modification of the SVM structure. In this paper, the *a-posteriori* probability fitting method [17] is adopted since the use of a parametric model allows a direct fitting of the *a-posteriori* probability $Pr \{ \chi = \underline{1} | \underline{\Gamma}_E \}$. More in detail, such a model approximates the *a-posteriori* probability through a sigmoid function

$$Pr \{ \chi_m = 1 | (\underline{\Gamma}_E, m) \} = \frac{1}{1 + \exp \left\{ \gamma \hat{\Phi} \left(\underline{\varphi} (\underline{\Gamma}_E, m) \right) + \delta \right\}} \quad m = 1, \dots, M \quad (2.12)$$

where γ and δ are unknown parameters to be determined.

To estimate the optimal values for the parameters of the sigmoid function, a fitting process is performed. A subset of the input patterns of the training set is chosen $\{ (\underline{\Gamma}_E, m, \chi_m; m = 1, \dots, M)^{(s)}; s = 1, \dots, S \}$, where $\hat{\Phi}_m^{(s)} = \hat{\Phi} \left(\underline{\varphi} \left(\underline{\Gamma}_E^{(s)}, m \right) \right)$. Then, the following cost function is defined

$$\begin{aligned} & \Upsilon \{ \gamma, \delta \} = \\ & = \sum_{s=1}^S \sum_{m=1}^M \left\{ \frac{\chi_m^{(s)} + 1}{2} \log \left[\frac{1}{1 + \exp(\gamma \hat{\Phi}_m^{(s)} + \delta)} \right] + \left(\frac{1 - \chi_m^{(s)}}{2} \right) \log \left[\frac{\exp(\gamma \hat{\Phi}_m^{(s)} + \delta)}{1 + \exp(\gamma \hat{\Phi}_m^{(s)} + \delta)} \right] \right\} \end{aligned} \quad (2.13)$$

and successively minimized to define γ and δ according to the numerical procedure proposed in [18]⁽³⁾ to solve the problems (i.e., the use of a kind of Levenberg-Marquardt method for unconstrained optimization) of the implementation of Platt's probabilistic outputs method pointed out in [17].

Summarizing, the SVM optimization problem needs three successive steps: (I) determining the hyper-parameters array (*model selection*), that is C and all the parameters that define the kernel function (e.g., the Gaussian width σ^2 when Gaussian kernels are used), by considering the “*training dataset*”; (II) determining the *functional parameters* \underline{a} and b starting from the “*training dataset*” and solving the dual problem (2.10); (III) determining the *a-posteriori fitting parameters* γ and δ starting from a subset of the “*training dataset*” (*validation phase*); (4) testing the SVM on a different dataset (*test phase*).

³⁽³⁾ Available at <http://www.csie.ntu.edu.tw/~cjlin/libsvmtools/>.

2.2. MAPPING OF THE DECISION FUNCTION INTO THE
A-POSTERIORI PROBABILITY

Chapter 3

Three-dimensional Buried Object Detection

In this chapter, a multi-resolution approach for the detection of three-dimensional buried objects is proposed. The geometrical features as size and position of single and multiple scatterers are estimated starting from the electromagnetic field data. The methodology is based on a support vector machine classifier integrated with a iterative procedure that increases the detection resolution only in those regions where target objects are supposed to be located. The definition of a multi-resolution probability map of objects presence that gives a simple and computationally effective estimation of the subsurface environment is provided. The real-time detection capabilities as well as the current limitations of the approach, concerned with both single and multiple objects, are verified by showing selected numerical results.

3.1 Introduction

The retrieval of information from underground by means of noninvasive techniques is of huge interest in many areas of science and engineering such as geology, hydrology and environmental engineering. A variety of methods, both two- and three-dimensional, have been provided to reconstruct geometrical and electric features of buried objects from measures of scattered field data collected with different kind of sensors such as the most widely used magnetometers, electromagnetic induction (EMI) or ground penetrating radar (GPR) [19]-[26]. Depending on the applications, the received signal can be studied both in time domain or frequency domain in order to profitably distinguish the object signatures from potential false detections [27],[28]. Whichever the methodology, the common goal can be brought back in correctly localize and characterize single or multiple targets in a fast and effective way. However, standard inversion algorithms that utilize numerical techniques for theoretical forward models, are accurate but more challenging too [21],[29]. Usually, these techniques fall in the class of pixel-based inverse methods that estimate the unknown physical properties of the medium over a dense discretization of the domain requiring the solution of large scale and ill-posed problems. Alternatively, geometric inverse methods require lower computational complexity providing only geometrical informations such as position, shape and size of the targets [20, 25]. However, they still rely on accurate numerical or analytical models that tend to be time consuming. In the framework of computationally efficient approaches, machine learning provides a number of computational algorithms for data analysis designed to directly tune themselves in response to a set of available data and to be easily implemented on hardware architectures [30]. In the scientific literature, several solutions to subsurface problems have been proposed by applying *learning-by-example* techniques as online processing tools, for example to characterize geologic facies [31] or classify buried exploded ordnance [32]-[35].

In [59]-[38], procedures based on support vector machine (SVM) [6, 1] that outperform methods based on neural networks (NNs) [both multilayer perceptron (MLP) and radial basis function (RBF)] have been shown. The subsurface detection problem has been successfully recast both as a regression and a classification problem in order to identify single and multiple scatterers. As pointed out in [38], the regression-based approaches are suitable in dealing with a limited number of unknowns since SVMs have been developed to solve one-output learning problems. On the other hand, the classification approach deals also with complex configurations of multiple scatterers in two-dimensional scenarios.

In this work, an innovative multi-resolution procedure for real-time detection of three-dimensional buried objects is presented. The problem of object detection is solved by means of a suitable SVM-based classifier integrated with a multi step process [80] in order to increase the resolution of the reconstructions and also to further decrease the computational time of the SVM test phase. More specifically,

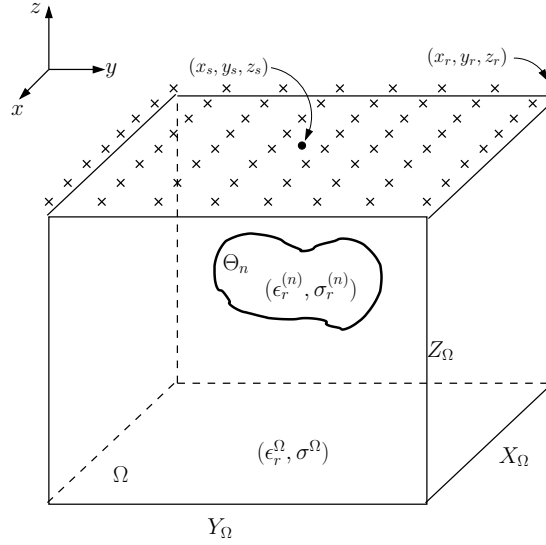


Figure 3.1: Three-dimensional geometry.

a more precise detection is obtained by means of an iterative synthetic zooming performed on those spatial regions where the objects are supposed to be located according to the results obtained at the previous step. At the end of the online iterative procedure, a multi-resolution map with an high-order detection accuracy is obtained. It has to be noticed that the SVM is trained only once starting from a finite set of labeled feature vectors representing the training samples. Each sample connects the available a-priori information about the object positions with the corresponding measured data. Once the learning process is completed, the test data related to objects located in unknown positions are iteratively classified according to the offline generated decision function and the proposed multi-resolution procedure.

The remaining of the chapter is organized as follows. The mathematical formulation of the proposed procedure is described in detail Section 3.2. Section 3.3 deals with an exhaustive numerical validation aimed at assessing the effectiveness of the proposed technique. Some final remarks are drawn in Section 3.4.

3.2 Mathematical Formulation

Let us consider a typical three-dimensional subsurface scenario as shown in Fig. 3.1. The homogeneous lossy soil is characterized by known relative dielectric permittivity ϵ_r^Ω and by a conductivity σ^Ω . The investigation domain $\Omega = \{0 \leq x \leq X_\Omega, 0 \leq y \leq Y_\Omega, 0 \leq z \leq Z_\Omega\}$ lies in the subsurface region and has size constrained by the overall dimension of the planar array and by a maximum depth Z_Ω . A x -directed dipole located in (x_s, y_s, z_s) , with $x_s = X_\Omega/2$ and $y_s = Y_\Omega/2$,

3.2. MATHEMATICAL FORMULATION

acts as electromagnetic source illuminating the scenario, while a planar array of R isotropic probes gather the data at given positions (x_r, y_r, z_r) , $r = 1, \dots, R$. Let $\underline{E}_{void}(x, y, z)$ be the field collected in a reference configuration, i.e. without objects, and $\underline{E}_{full}(x, y, z)$ be the field measured in the perturbed scenario. This latter configuration is characterized by the presence of N scattering regions Θ_n belonging to Ω with arbitrary shapes, permittivity $\varepsilon_r^{(n)}$ and conductivity $\sigma^{(n)}$, $n = 1, \dots, N$. The relationship between \underline{E}_{full} and \underline{E}_{void} can be mathematically expressed by the scattering equation, i.e.

$$\begin{aligned} \underline{E}_{full}(x_r, y_r, z_r) = & \underline{E}_{void}(x_r, y_r, z_r) + \\ & + k^2 \int_{\Omega} \underline{E}(x, y, z) \cdot \underline{G}(x_r, y_r, z_r) \Upsilon \left\{ (x, y, z) | \Theta_n, \left(\varepsilon_r^{(n)}, \sigma^{(n)} \right) \right\} dx dy dz \end{aligned} \quad (3.1)$$

where $\underline{E}(x, y, z)$ is the electric field inside Ω for the perturbed scenario, \underline{G} is the Green's function of the inhomogeneous medium [100], and Υ is the dielectric profile defined as

$$\Upsilon(x, y, z) = \begin{cases} \varepsilon_r^{(n)} - \varepsilon_r^{\Omega}(x, y, z) - j \frac{\sigma^{(n)} - \sigma^{\Omega}(x, y, z)}{2\pi f \varepsilon_0}, & \text{if } (x, y, z) \in \Theta_n; n = 1, \dots, N \\ 0, & \text{otherwise.} \end{cases} \quad (3.2)$$

Starting from the knowledge of the following differential quantity

$$\underline{\Gamma}(x_r, y_r, z_r) = \frac{|\underline{E}_{full}(x_r, y_r, z_r) \cdot \hat{x}| - |\underline{E}_{void}(x_r, y_r, z_r) \cdot \hat{x}|}{|\underline{E}_{void}(x_r, y_r, z_r) \cdot \hat{x}|}; \quad r = 1, \dots, R \quad (3.3)$$

representing the normalized field contribution scattered by Θ_n , $n = 1, \dots, N$ in the r -th measurement point, $r = 1, \dots, R$ along the \hat{x} direction, the detection problem can be recast as the definition of a probability map of objects presence inside Ω . Toward this end, let us partition the investigation domain into a three-dimensional lattice of C cubic cells whose center coordinates are (x_c, y_c, z_c) , $c = 1, \dots, C$ and to which a probability value of object presence $h_c = Pr\{\chi_c = +1 | \underline{\Gamma}\}$ can be associated, where $\chi_c = \pm 1$ is the binary cell state, that is ‘‘occupied’’ (i.e., $\chi_c = +1$) if $(x_c, y_c, z_c) \in \Theta_n$, $n = 1, \dots, N$, or ‘‘empty’’ (i.e., $\chi_c = -1$), otherwise. Starting from the input data $\underline{\Gamma}$, the problem can be thought as the retrieval of the probability presence function

$$H(x, y, z) = \sum_{c=1}^C h_c(x_c, y_c, z_c) J_c(x, y, z) \quad (3.4)$$

expressed as a linear combination of non-overlapping basis functions $J_c(x, y, z) = 1$ if (x, y, z) belongs to the c -th cubic cell, and $J_c(x, y, z) = 0$, otherwise.

The spatial resolution of the unknown probability presence function is improved by means of a three-dimensional multi-resolution (*IMSA-3D*) representation

$$H^{(m)}(x, y, z) = \sum_{k=0}^{K(m)} \sum_{c(k)=1}^{C(k)} h^{(m)}(x_{c(k)}, y_{c(k)}, z_{c(k)}) J_{c(k)}(x, y, z) \quad m = 1, \dots, M_{opt} \quad (3.5)$$

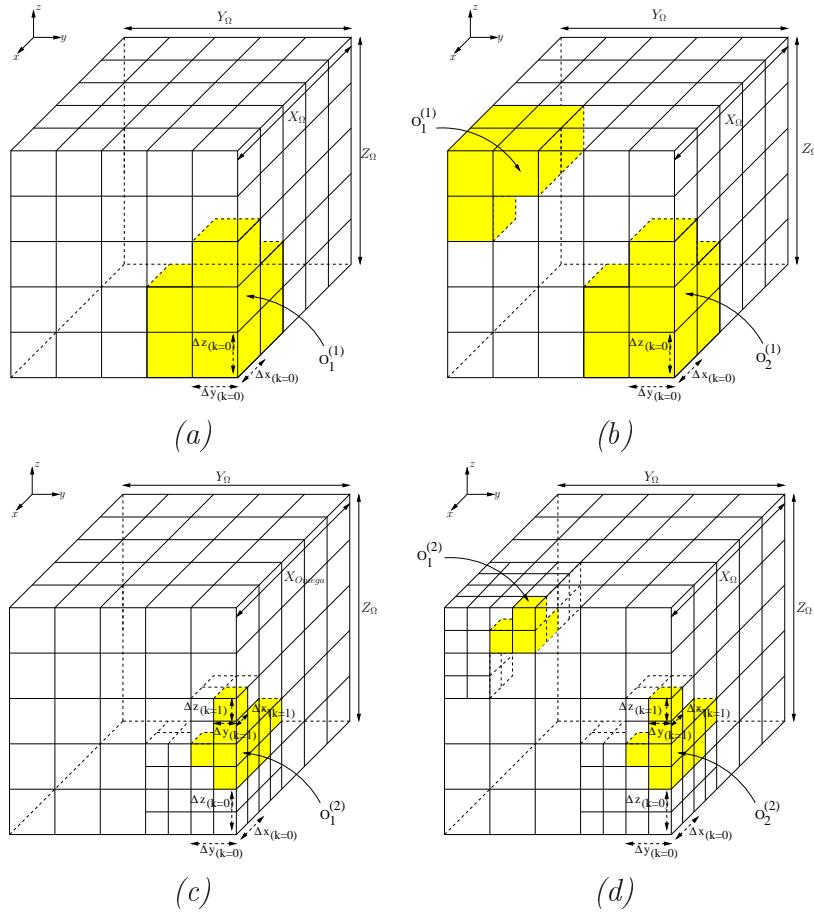


Figure 3.2: *RoIs* identification at step $m = 1$ [with $k = 0$ (a) and $k = 1$ (b)] and $m = 2$ [with $k = 0$ (c) and $k = 1$ (d)].

m being the index of the iterative procedure that stops at the optimal step M_{opt} when the requirement on the resolution level $k = 0, \dots, K(m)$ is reached. Therefore, for a given value of k , $C(k)$ cells identify those regions of interest (RoIs) (as shown in Fig. 3.2) where the probability of presence $h^{(m)}(x_{c(k)}, y_{c(k)}, z_{c(k)})$ is higher.

3.2.1 IMSA-3D SVM-based procedure

In order to evaluate the multi-resolution representation of the unknown probability presence function, the proposed *IMSA-3D* procedure is performed by means of a SVM-based methodology detailed in the following.

Training Phase. The learning process aims at defining the unknown inverse mapping $H^{(m)}(x, y, z) = \Psi(\underline{\Gamma})$. Assuming the knowledge of a finite set of T

3.2. MATHEMATICAL FORMULATION

training scenarios

$$\left\{ [\chi_p, (x_p, y_p, z_p), \underline{\Gamma}; p = 1, \dots, P]^{(t)}, t = 1, \dots, T \right\}. \quad (3.6)$$

P being the number of training cells, the states χ_p , $p = 1, \dots, P$ are assigned as an *a-priori* information related to each training configuration. More in detail, for a given t -th training example, a set of N scatterers can reside into the investigation domain producing a known combination of states χ_p , $p = 1, \dots, P$. The instances constituting the training set are called *input-output pairs*. The available measured data are the *input* $\underline{\alpha}_p^{(t)} = \left\{ [(x_p, y_p, z_p), \underline{\Gamma}; p = 1, \dots, P]^{(t)}, t = 1, \dots, T \right\}$ and the associated truth the *output* $\underline{\beta}_p^{(t)} = \left\{ \chi_p^{(t)}; p = 1, \dots, P; t = 1, \dots, T \right\}$. Starting from these known relations, the problem at hand turns out to be the definition of the decision function $\Psi(\bullet)$ which learns the mapping

$$\Psi : \underline{\alpha}_p^{(t)} \mapsto \underline{\beta}_p^{(t)}; p = 1, \dots, P; t = 1, \dots, T \quad (3.7)$$

in order to successively classify the unseen *input* test data

$$\underline{\alpha}_{test} = \{(x_c, y_c, z_c), \underline{\Gamma}; c = 1, \dots, C\}.$$

According to the statistical learning theory [6], let us define the decision function

$$\Psi(\underline{\alpha}_{test}) = (\underline{w} \cdot \phi(\underline{\alpha}_{test})) + b \quad (3.8)$$

$\phi(\cdot)$ being the nonlinear operator mapping the input data into an higher dimensional space, called *feature space*. Among all hyperplanes separating the positive training data $\underline{\alpha}_p^{(t)} \Big|_{\underline{\beta}_p^{(t)}=1}$ from the negative ones $\underline{\alpha}_p^{(t)} \Big|_{\underline{\beta}_p^{(t)}=-1}$ there exists unique one yielding the maximum separating margin between the classes. This optimal hyperplane is constructed by solving an optimization problem, switched to a Lagrangian formulation [39], respect to \underline{w} and b . The problem reduces to find the optimal solution through an expansion in terms of a subset of examples belonging to the training set, namely those examples whose Lagrange multipliers are $0 < \iota_p^{(t)} < C^{(SVM)}$, called *support vectors* (SVs). The hyperparameter $C^{(SVM)}$ controls the tradeoff between training error minimization and margin maximization. If $\iota_p^{(t)} = C^{(SVM)}$ the corresponding SVs are called *bound support vectors* (BSVs) which lie inside the margin producing non-negative slack variables [1]. In this sense, the number of BSVs is an indication of training errors amount. Moreover, many slack variables with large values mean strongly overlapped classes and hence limited generalization capabilities. Unfortunately, the $C^{(SVM)}$ hyperparameter is unintuitive and has to be calibrated as well as the other kernel parameters (e.g.: the gaussian width γ for the RBF kernel function) during the model selection phase.

Test phase - Step ($m = 1$). At first, the whole domain Ω is considered and the multi-resolution procedure generates a coarse estimation of the probability

presence function with resolution level initialized to $k = 0$. The probability values $h^{(m)}(x_{c(k)}, y_{c(k)}, z_{c(k)})$ are evaluated by mapping the unthresholded output of the decision function $\Psi(\underline{\alpha}_{test})$ into a parametric form of a sigmoid function

$$h^{(m)}(x_{c(k)}, y_{c(k)}, z_{c(k)}) = \frac{1}{1 + \exp(\eta\Psi(\underline{\alpha}_{test}) + \mu)} \quad (3.9)$$

η and μ being parameters determined by solving the regularized maximum likelihood problem as in [58] by means of a subset of the available training set.

Test phase - Steps ($m > 1$), ($m < M_{opt}$). These steps are aimed at increasing the resolution of the lattice, by which the probability function is evaluated, only in those regions where the objects are supposed to be located. The method is formulated as the following two-step procedure:

A. RoIs Identification: starting from the probability evaluated at the previous step $m - 1$, a scaled representation of the probability function

$$U^{(m-1)}(x, y, z) = \sum_{k=0}^{K(m-1)} \sum_{c(k)=1}^{C(k)} u^{(m-1)}(x_{c(k)}, y_{c(k)}, z_{c(k)}) J_{c(k)}(x, y, z) \quad (3.10)$$

is determined by introducing the normalized probability coefficients

$$u^{(m-1)}(x_{c(k)}, y_{c(k)}, z_{c(k)}) = \frac{h^{(m-1)}(x_{c(k)}, y_{c(k)}, z_{c(k)}) - h_{min}^{(m-1)}}{h_{max}^{(m-1)} - h_{min}^{(m-1)}}, \quad \begin{array}{l} c(k) = 1, \dots, C(k), \\ k = 0, \dots, K(m) \end{array} \quad (3.11)$$

where $h_{min}^{(m-1)} = \min_{k=0, \dots, K(m)} \{ \min_{c(k)=1, \dots, C(k)} [h^{(m-1)}(x_{c(k)}, y_{c(k)}, z_{c(k)})] \}$ and $h_{max}^{(m-1)} = \max_{k=0, \dots, K(m)} \{ \max_{c(k)=1, \dots, C(k)} [h^{(m-1)}(x_{c(k)}, y_{c(k)}, z_{c(k)})] \}$. The RoIs $O_b^{(m)}$ $b = 1, \dots, B(m)$, where $B(m)$ is the total number of regions at step m , are identified by thresholding the normalized probability function and nulling the values smaller than the user-defined probability threshold ϵ_{th} . Each RoI has an occupation volume $V_b^{(m)}$, $b = 1, \dots, B(m)$ proportional to the number of adjacent basis functions $J_{c(k)}$ whose probability $u^{(m-1)}(x_{c(k)}, y_{c(k)}, z_{c(k)}) > \epsilon_{th}$.

B. Multi-resolution probability evaluation: once the RoIs are identified, the resolution level is increased ($k \leftarrow k + 1$) when $(x, y, z) \in O_b^{(m)}$, $b = 1, \dots, B(m)$ and a new set of $C(k) = \sum_{b=1}^{B(m)} C_b(k)$ smaller cells is generated in order to partition the volume of each RoI with a number of cells

$$C_b(k) = \frac{V_b^{(m)}}{\sum_{b=1}^{B(m)} V_b^{(m)}} C(k), \quad b = 1, \dots, B(m). \quad (3.12)$$

Therefore, the probability function (3.5) is updated by computing the probability coefficients $h^{(m)}(x_{c(k)}, y_{c(k)}, z_{c(k)})$ in the new higher-resolution cells.

Test phase - Step ($m = M_{opt}$). The iterative methodology repeats the steps *A* (*RoIs Identification*) and *B* (*Multi-resolution probability evaluation*) until the total volume of the RoIs decreases [$\sum_{b=1}^{B(m-1)} V_b^{(m-1)} - \sum_{b=1}^{B(m)} V_b^{(m)} > 0$] or the RoIs number $B(m)$ changes [$B(m) - B(m-1) \neq 0$].

3.3 Numerical Results

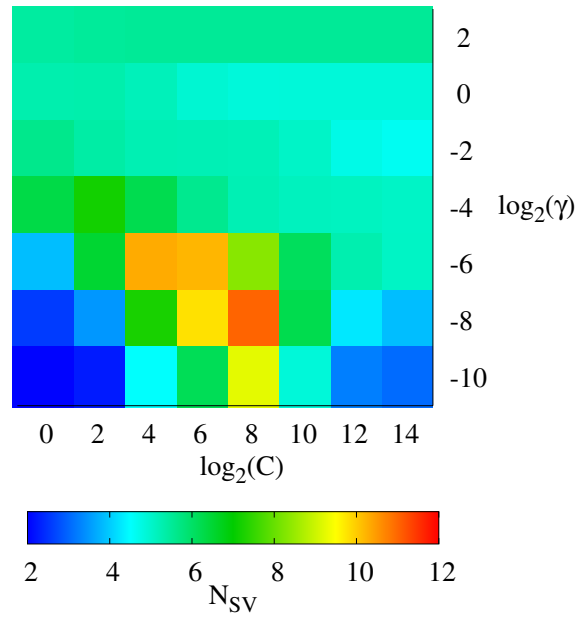
The results of a selected set of numerical examples are reported in order to assess the effectiveness and reliability of the proposed approach when dealing with three-dimensional realistic scenarios. In Section 3.3.1 the training of the SVM is described and some considerations about SVM parameter calibration are pointed out. In Section 3.3.2 the behavior of the multi-resolution (*IMSA-3D*) procedure is shown and the performance are also compared with the single-step (*BARE*) approach. The validation of the methodology with noisy data is also considered. Sect. 3.3.3 investigates the potentialities and the current limitations of the *IMSA-3D* in detecting multiple objects. In order to verify the reliability of the proposed methodology in correspondence with various and realistic subsurface configurations, more complex scenarios with smaller objects and different soil characteristics are considered (Sect. 3.3.4).

With reference to the problem geometry shown in Fig. 3.1, the homogeneous subsurface region with dielectric parameters $\varepsilon_r^\Omega = 4.0$ and $\sigma^\Omega = 4.0 \times 10^{-3}$ [41] and geometrical size $X_\Omega = 3.66 \lambda$, $Y_\Omega = 3.66 \lambda$, $Z_\Omega = 0.64 \lambda$ is considered, λ being the wavelength at the working frequency $f = 500 \text{ MHz}$. A set of target regions Θ_n , $n = 1, \dots, N$ with dielectric characteristics different from those of the background can assume whatever shape and position inside Ω . As a preliminary configuration, let us consider three-dimensional target regions as finite-length lossless cylinders of radius $R_{obj}^{(n)} = 0.19 \lambda$, height $H_{obj}^{(n)} = 0.19 \lambda$ [42] and with relative permittivity $\varepsilon_r^{(n)} = 2.5$, $n = 1, \dots, N$ [28][32]. The considered domain is illuminated by a x -oriented short-dipole probe located in $x_s = y_s = 1.83 \lambda$ at a distance $z_s = 0.11 \lambda$ above the air-soil interface. At the same height is placed a planar array of $R = 100$ ideal receivers equally spaced and covering the whole $X_\Omega \times Y_\Omega$ upper horizontal surface of Ω .

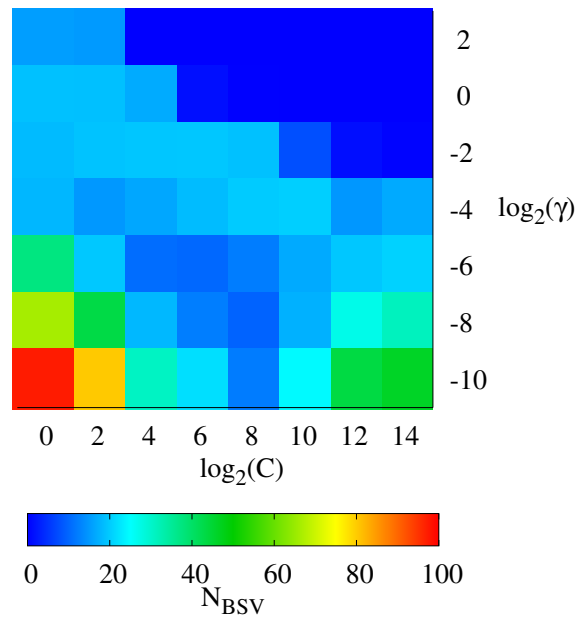
3.3.1 SVM training and parameter selection

Concerning the training sets, three different data sets have been considered, each one composed by $T = 300$ scenarios and characterized by a fixed number of buried objects. More specifically, $n = 1, \dots, N_{max}$, where $N_{max} = 3$ is the maximum number of objects, training sets have been synthetically generated. The positions of the objects have been randomly chosen and mapped into the binary class indexes $\chi_p^{(t)}$ determining the states (occupied or empty) of the $P = 100$ training cells. The training phase is performed by adopting a RBF kernel function whose gaussian width γ has to be calibrated as well as the user-defined SVM hyperparameter $C^{(SVM)}$ in order to solve the model selection issue. In order to point out the influence of the parameters calibration on the decision function generation, Fig. 3.3(a) shows the number of SVs

$$N_{SV} = \frac{SV_s}{T \times C} \times 100 \quad (3.13)$$



(a)



(b)

Figure 3.3: *SVM training* - Number of support vectors (SVs) (a) and bounded support vectors (BSVs) (b) versus the SVM hyperparameters.

3.3. NUMERICAL RESULTS

as the percentage of total training samples, and the number of BSVs [Fig. 3.3(b)]

$$N_{BSV} = \frac{BSVs}{SVs} \times 100 \quad (3.14)$$

obtained during the grid search over the couple of parameters $C^{(SVM)}$ and γ . In particular, the training set generated with $N_{max} = 1$ has been considered. The sparseness of the SVM solution depends on the number of SVs, given that small N_{SV} leads to a structural simplification of the classifier thanks to the removing of the irrelevant components. In this sense, limiting the number of SVs through the parameter selection turns out to be a simple and effective solution to control the generalization capabilities of the classifier. Besides the N_{SV} as a generalization performance indicator, the number of BSVs is equivalent to the amount of training errors. Since the SVM-based algorithm has to tolerate a certain fraction of outliers, the BSVs number represents those training samples that can crucially affect the hyperplane. Nevertheless, the best separating function leads to the minimal number of training errors. As it can be seen in Fig. 3.3, in the range of $2^{-4} < \gamma < 2^2$ and $2^6 < C^{(SVM)} < 2^{14}$ both the N_{SV} and N_{BSV} indicators are small. It means that the generated hyperplane correctly separates the positive and negative training samples in this range of parameters. Starting from this analysis of SVs and BSVs, that gives a preliminary estimation of the best SVM parameters, the optimal values $C^{(SVM)} = 2^{10}$ and $\gamma = 2^0$ have been chosen.

3.3.2 Numerical validation of the IMSA-3D procedure

The first representative experiment deals with the detection of a single-scatterer ($N = 1$) in noiseless data condition. A test set of $\bar{T}_1 = 50$ scenarios randomly chosen and not belonging to the training set has been considered. Fig. 3.4 shows the probability maps obtained with the *IMSA-3D* approach for one example of the test set. The three orthogonal planes passing through the center of the object at $(x_{obj}^{(1)} = y_{obj}^{(1)} = 1.16\lambda, z_{obj}^{(1)} = -0.32\lambda)$ show the probability evaluated during the multi-resolution process, from the first step [$m = 1$, Fig. 3.4(a)] until the stationary condition is achieved at step $m = 4$ [Fig. 3.4(d)]. At the initial step, the resolution level is set to $k = 0$ and the domain is partitioned into $C(0) = 72$ cubic cells in order to evaluate a coarse estimation of the probability function. The following steps identify a single RoI $O_1^{(m)}$ where the resolution improve from $\Delta_k = 0.61\lambda, k = 0$ up to $\Delta_3 = 7.64 \times 10^{-2}\lambda$ in the RoI $O_1^{(4)}$. In order to quantitatively evaluate the improved accuracy provided by the multi-resolution procedure, let us define the *object-localization-error*

$$v_n^{(m)} = \sqrt{\left(x_{obj}^{(n)} - \tilde{x}_n^{(m)}\right)^2 + \left(y_{obj}^{(n)} - \tilde{y}_n^{(m)}\right)^2 + \left(z_{obj}^{(n)} - \tilde{z}_n^{(m)}\right)^2} \quad (3.15)$$

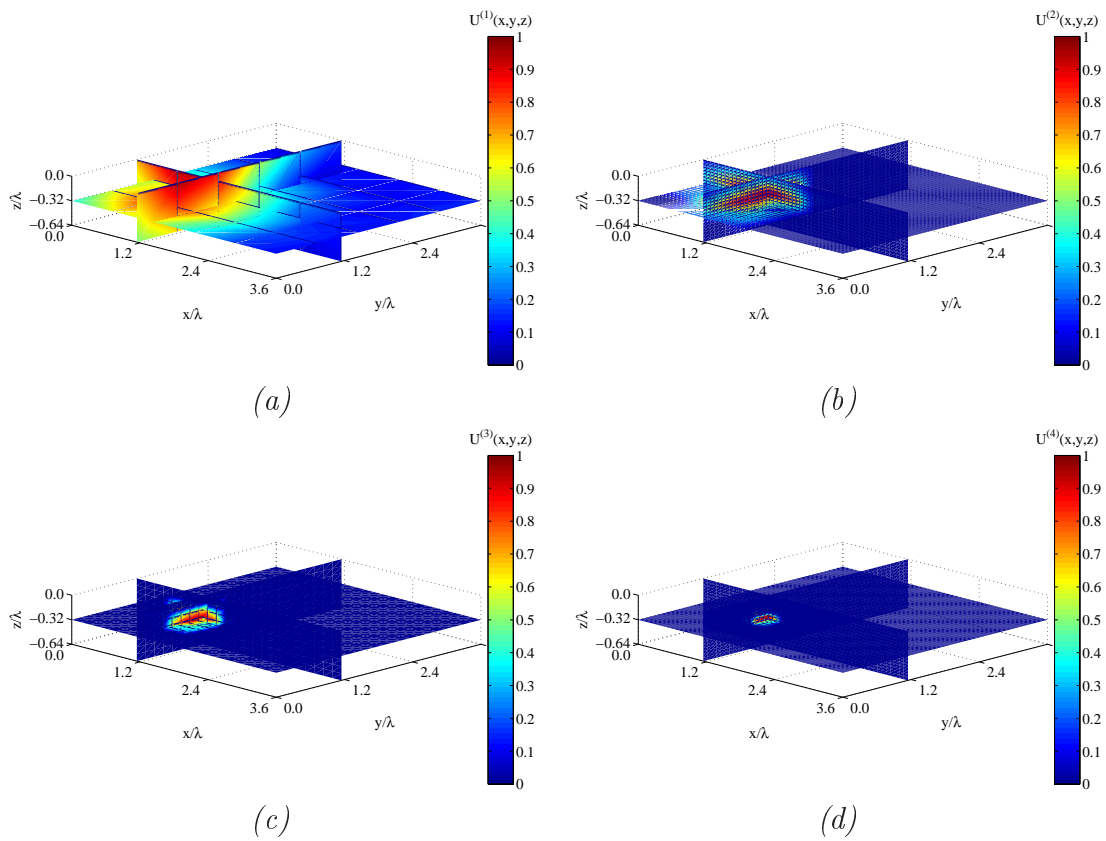


Figure 3.4: *IMSA-3D Procedure* - Probability map determined by the *IMSA* procedure at $m = 1$ (a), $m = 2$ (b), $m = 3$ (c) and $m = M_{opt} = 4$ (d) for single buried object ($N = 1$).

3.3. NUMERICAL RESULTS

as the geometrical distance between the actual barycenter of the n -th object $(x_{obj}^{(n)}, y_{obj}^{(n)}, z_{obj}^{(n)})$ and the estimated one $(\tilde{x}_n^{(m)}, \tilde{y}_n^{(m)}, \tilde{z}_n^{(m)})$, where

$$\begin{aligned}\tilde{x}_n^{(m)} &= \frac{\sum_{k=0}^{K(m)} \sum_{c(k)=1}^{C(k)} h^{(m)}(x_{c(k)}, y_{c(k)}, z_{c(k)}) x_{c(k)}}{\sum_{k=0}^{K(m)} \sum_{c(k)=1}^{C(k)} h^{(m)}(x_{c(k)}, y_{c(k)}, z_{c(k)})}, \\ \tilde{y}_n^{(m)} &= \frac{\sum_{k=0}^{K(m)} \sum_{c(k)=1}^{C(k)} h^{(m)}(x_{c(k)}, y_{c(k)}, z_{c(k)}) y_{c(k)}}{\sum_{k=0}^{K(m)} \sum_{c(k)=1}^{C(k)} h^{(m)}(x_{c(k)}, y_{c(k)}, z_{c(k)})}, \\ \tilde{z}_n^{(m)} &= \frac{\sum_{k=0}^{K(m)} \sum_{c(k)=1}^{C(k)} h^{(m)}(x_{c(k)}, y_{c(k)}, z_{c(k)}) z_{c(k)}}{\sum_{k=0}^{K(m)} \sum_{c(k)=1}^{C(k)} h^{(m)}(x_{c(k)}, y_{c(k)}, z_{c(k)})}\end{aligned}\quad (3.16)$$

are calculated as the normalized average of the test cell barycenters at m -th step weighted by the corresponding probabilities of presence $h^{(m)}(x_{c(k)}, y_{c(k)}, z_{c(k)}) > 0$. Let us also define the *volume-occupation*

$$\xi_n^{(m)} = \frac{\tilde{\kappa}_n^{(m)}}{\kappa_n} \quad (3.17)$$

where

$$\tilde{\kappa}_n^{(m)} = \frac{4}{3}\pi \left\{ \frac{\sum_{k=0}^{K(m)} \sum_{c(k)=1}^{C(k)} \left[\frac{h^{(m)}(x_{c(k)}, y_{c(k)}, z_{c(k)}) v_{c(k)}^{(m)}}{\max_{c(k)} \{h^{(m)}(x_{c(k)}, y_{c(k)}, z_{c(k)})\}} \right]}{\sum_{k=0}^{K(m)} \sum_{c(k)=1}^{C(k)} \left[\frac{h^{(m)}(x_{c(k)}, y_{c(k)}, z_{c(k)})}{\max_{c(k)} \{h^{(m)}(x_{c(k)}, y_{c(k)}, z_{c(k)})\}} \right]} \right\}^3 \quad (3.18)$$

and κ_n is the actual volume of the considered n -th object, an analytically evaluated index that quantify the estimated volume in terms of probabilities, where

$$v_{c(k)}^{(m)} = \sqrt{\left(x_{c(k)} - \tilde{x}_n^{(m)}\right)^2 + \left(y_{c(k)} - \tilde{y}_n^{(m)}\right)^2 + \left(z_{c(k)} - \tilde{z}_n^{(m)}\right)^2}. \quad (3.19)$$

In such a case, the values of the error figures turn out to be equal to $v_1^{(1)} = 0.16 \lambda$ and $\xi_1^{(1)} = 21.03$ at the first step and both decrease down to $v_1^{(4)} = 0.07 \lambda$ and $\xi_1^{(4)} = 0.68$, as shown in Fig. 3.5. The considered test configuration is effectively representative if compared with the error statistics reported in Tab. 3.1, calculated by considering the whole test set of $T_1 = 50$ configurations.

In order to guarantee a high probability of detection and a corresponding low probability of false alarm, the behavior of *IMSA-3D* approach has been also assessed in absence of objects inside Ω . It has to be noticed that the free-object configuration is not included in the training set. As shown in Fig. 3.6, the SVM-based methodology did not detect any object. The obtained probability map shows very small and not focused values, thus confirming the right identification of the free-objects scenario.

The improved detection capabilities of the multi-resolution strategy is further pointed out if compared with the *BARE* approach (Fig. 3.7) applied on the same test configuration and with the same classifier (i.e. the same training set

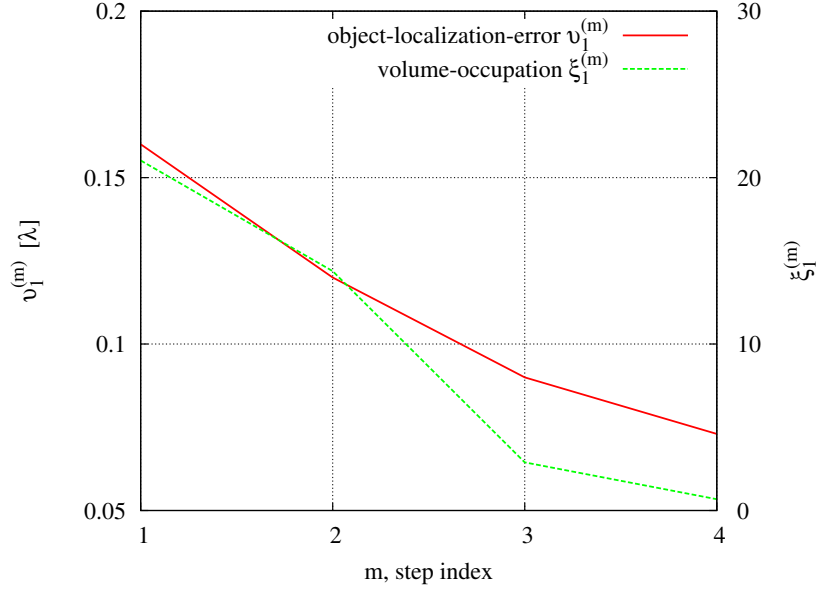


Figure 3.5: *IMSA-3D Procedure* - Performance indexes $v_1^{(m)}$ and $\xi_n^{(m)}$ versus the multi-resolution steps for single buried object ($N = 1$).

Method	$v_1^{(m)}$ [λ]			$\xi_1^{(m)}$		
	min	max	mean	min	max	mean
<i>IMSA</i>						
$m = 1$	4.68×10^{-2}	1.18	0.54	3.48	35.42	16.91
$m = 2$	2.99×10^{-2}	1.06	0.23	2.18	29.76	12.49
$m = 3$	2.32×10^{-2}	0.46	0.22	0.96	24.59	4.93
$m = 4$	2.21×10^{-2}	0.41	0.21	0.09	8.13	1.92
<i>BARE</i>	9.76×10^{-2}	1.16	0.59	2.81	28.93	16.88

Table 3.1: *Single buried object, $N = 1$* - Statistics of the performance indexes (*object-localization-error* v and *volume-occupation* ξ) for *BARE* and *IMSA* approaches.

3.3. NUMERICAL RESULTS

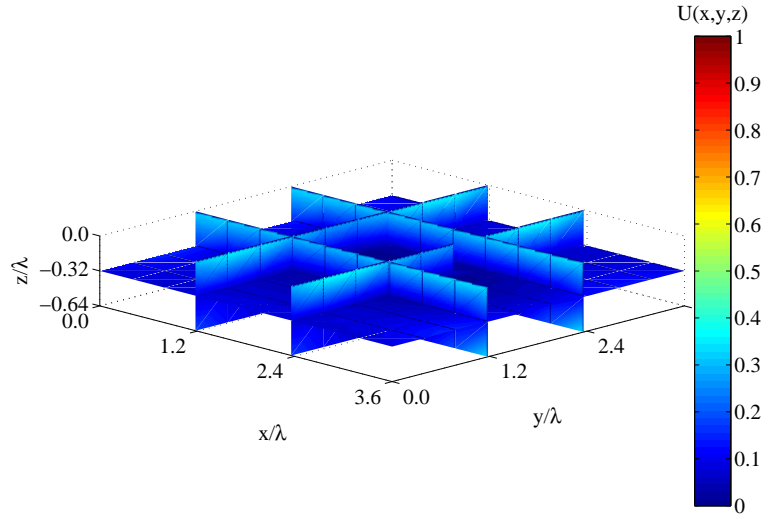


Figure 3.6: *IMSA-3D Procedure* - Probability map obtained with *IMSA-3D* approach in absence of buried objects ($N = 0$).

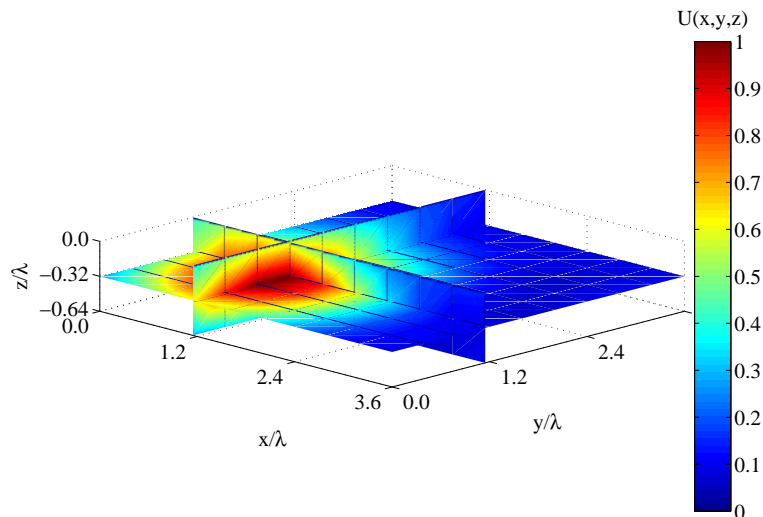


Figure 3.7: *IMSA-3D vs BARE* - Probability map determined by the *BARE* approach for $N = 1$ buried object.

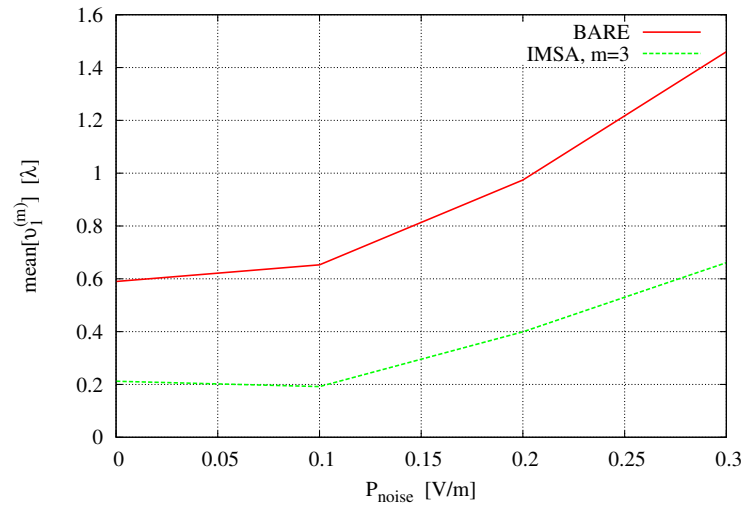
and SVM hyperparameter settings). In order to compare the results at the same resolution level, the *BARE* solution has been obtained with the highest resolution $\Delta_{BARE} = \Delta_3 = 7.64 \times 10^{-2} \lambda$ applied to all the investigation domain instead of to the single RoI $O_1^{(m)}$, $m = 1, \dots, M_{opt}$. Besides the *object-localization-error* is slightly greater ($v_1^{(BARE)} = 0.21 \lambda$), the *volume-occupation* is significantly larger ($\xi_1^{(BARE)} = 22.48$) as well as the number of decision function evaluations that is strictly related to the number of test cells ($C_{BARE} = 36864$ vs $\sum_{k=0}^{K=3} C(k) = 288$). Even if the computational load of a single SVM testing is very low, the *BARE* approach turns out to be more time consuming, thus reducing the real-time capabilities of such a methodology.

In order to point out the generalization capabilities of the proposed *IMSA-3D* approach in dealing with noisy data, a gaussian random noise with zero-mean and variance $\sigma^2 = P_{noise}$ is added to the total field $\underline{E}_{full}(x_r, y_r, z_r)$ and the noisy differential quantity $\widehat{\Gamma}(x_r, y_r, z_r)$ is used to generate the test set. The averaged error figures obtained with increasing noise amplitude have been evaluated and reported in Fig. 3.8. As it can be seen, both *object-localization-error* and *volume-occupation* of the *IMSA-3D* approach are always smaller if compared with the *BARE* results, thus confirming a stable behavior of the methodology also in noisy conditions. As a representative result, the probability map of the single-object configuration obtained with the *BARE* and *IMSA-3D* approaches with noisy data ($P_{noise} = 0.1 V/m$) are shown in Fig. 3.9(a) and 3.9(b), respectively. Even if the *IMSA-3D* method points out a slightly greater *object-localization-error* ($v_1^{(4)} \Big|_{P_{noise}=0.1} = 0.11 \lambda$) if compared with the noiseless test case, the actual position of the object still resides into the high-probability region.

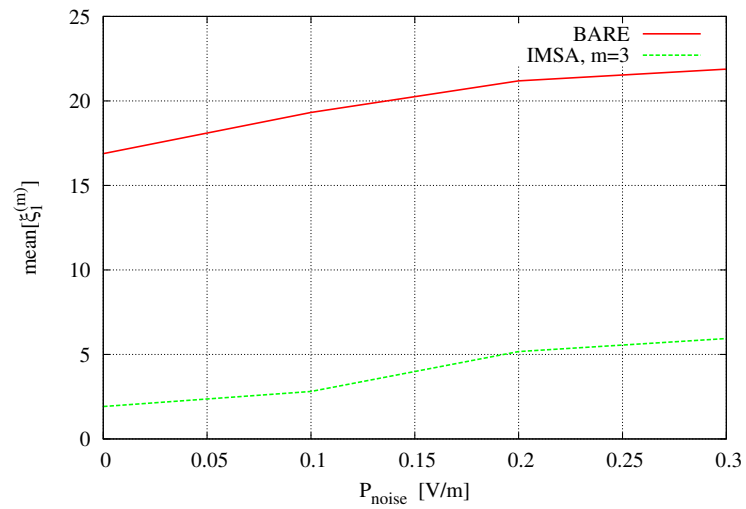
3.3.3 Detection of multiple objects

This section is aimed at confirming the capabilities of the proposed approach in detecting multiple scatterers. As expected, these scenarios are more complex if compared with the single-object test case and the SVM-based methodology provides higher *object-localization-error* values even if it is still able to localize the objects with an acceptable degree of accuracy. In Figure 3.10, the averaged *object-localization-error* [Fig. 3.10(a)] and *volume-occupation* [Fig. 3.10(b)] of *BARE* and *IMSA-3D* are compared when dealing with $n = 1, \dots, N_{max}$ number of objects, where $N_{max} = 3$ and with noisy data ($P_{noise} = 0.1 V/m$). The bar charts clearly show the outperforming capabilities of the multi-resolution technique in locating multiple scatterers and pointing out an *object-localization-error* always smaller than one wavelength. Concerning the *volume-occupation* index, the optimal step of the *IMSA-3D* procedure overestimates the object volumes of the most complex scenario ($N = 3$) with a maximum of $mean_n \left\{ \xi_n^{(3)} \right\} = 7.31$ respect to the widely greater volume overestimation obtained with the *BARE* approach [$mean_n \left\{ \xi_n^{(BARE)} \right\} = 24.32$]. In order to better appreciate the im-

3.3. NUMERICAL RESULTS

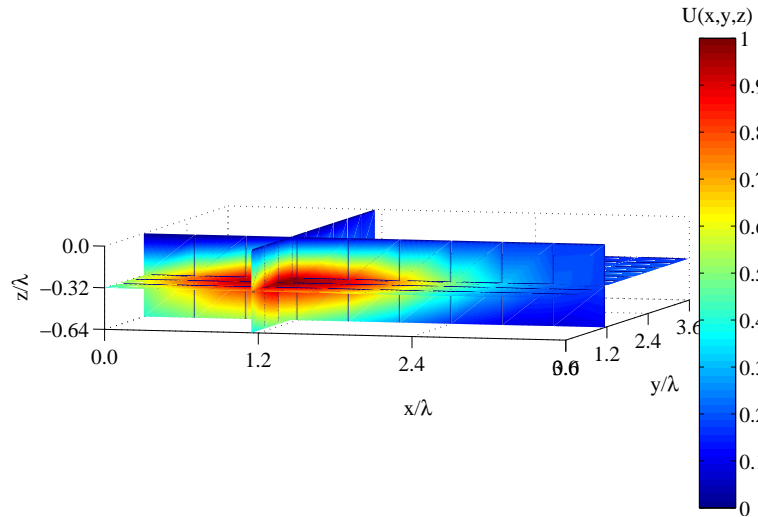


(a)

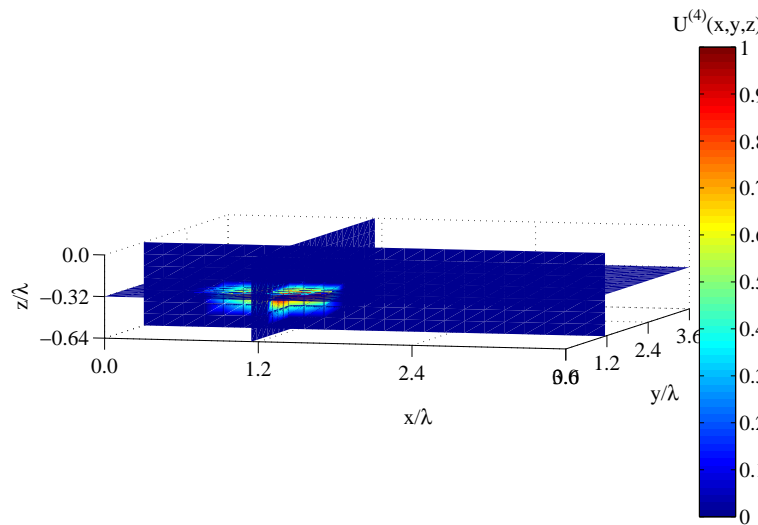


(b)

Figure 3.8: Numerical validation vs noise level - Object-localization-error (a) and volume-occupation (b) determined by the *BARE* and *IMSA-3D* procedures versus the additive noise amplitude P_N .



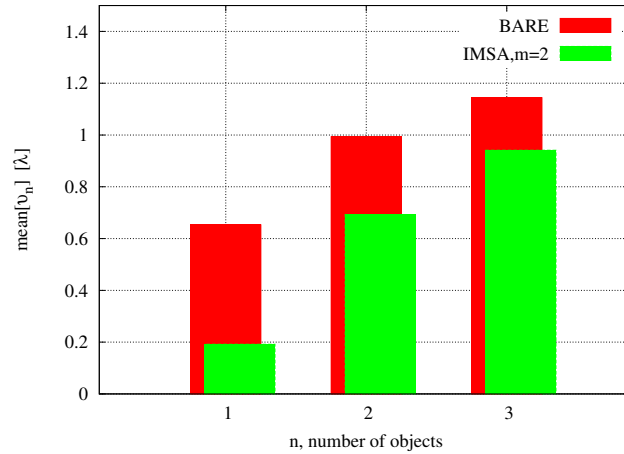
(a)



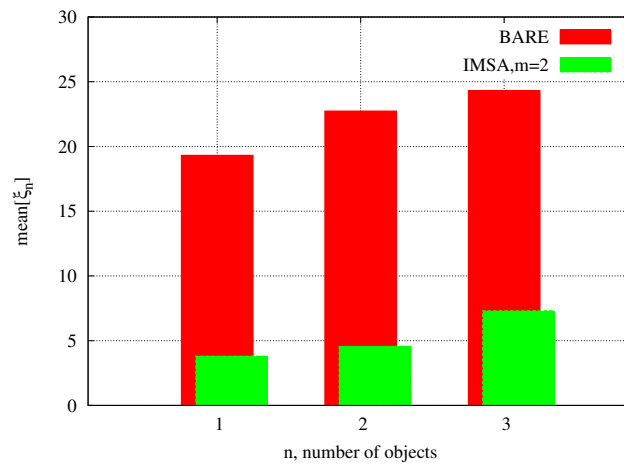
(b)

Figure 3.9: Numerical validation vs noise level - Probability maps determined by the BARE (a) and IMSA-3D (b) procedures with Noisy data [$P_N = 0.1 V/m$].

3.3. NUMERICAL RESULTS



(a)



(b)

Figure 3.10: *Numerical validation vs number of objects* - Object-localization-error (a) and volume-occupation (b) determined by the *BARE* and *IMSA-3D* procedures versus the number of objects $n = 1, 2, 3$ with noisy data $[P_N = 0.1 V/m]$.

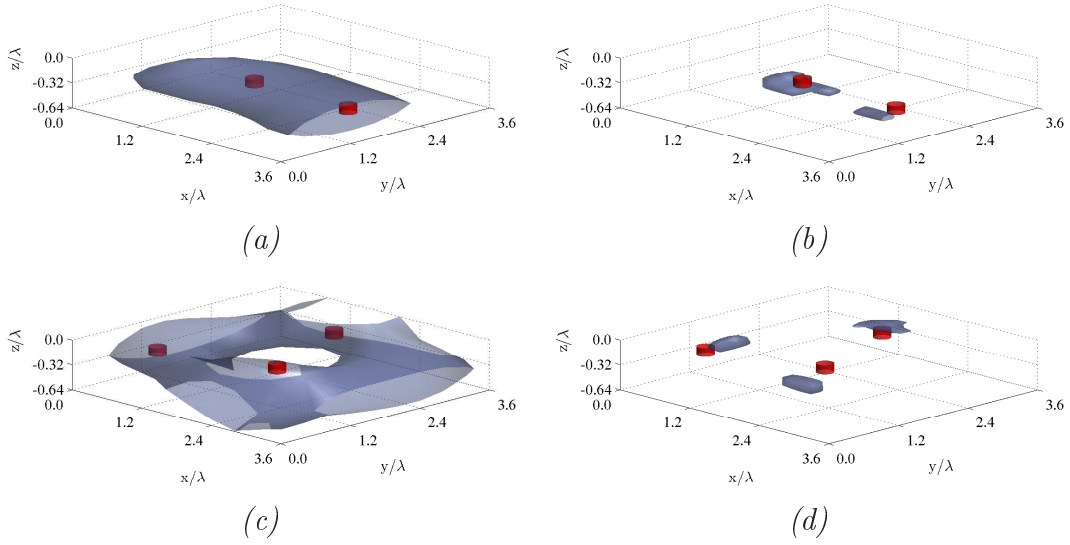


Figure 3.11: *Numerical validation vs number of objects* - Probability maps determined by the *IMSA-3D* procedures for multiple objects [$N = 2$ *BARE* (a), *IMSA* (b) and $N = 3$ *BARE* (c), *IMSA* (d)] with noisy data [$P_N = 0.1 V/m$].

proved resolution and detection capabilities of the *IMSA-3D* approach in multiple object scenarios, the maps obtained with the *BARE* and *IMSA-3D* approaches with $N = 2$ scatterers ($x_{obj}^{(1)} = 3.23 \lambda$, $y_{obj}^{(1)} = 1.61 \lambda$, $z_{obj}^{(1)} = -0.39 \lambda$), ($x_{obj}^{(2)} = 1.69 \lambda$, $y_{obj}^{(2)} = 1.51 \lambda$, $z_{obj}^{(2)} = -0.33 \lambda$) have been compared [Fig. 3.11(a) and Fig. 3.11(b)]. The *IMSA-3D* approach correctly identifies two RoIs and estimates the object positions with good precision in *object-localization-error* ($v_1^{(2)} = 0.41 \lambda$ and $v_2^{(2)} = 0.19 \lambda$) and a slightly overestimated *volume-occupation* ($\xi_1^{(2)} = 3.03$ and $\xi_2^{(2)} = 1.82$). On the contrary, the *BARE* approach estimates only one dilated high-probability region with a very high *volume-occupation* [$mean_n \{ \xi_n^{(BARE)} \} = 29.23$] which contains both the objects. The enhanced capabilities of the multi-resolution approach compared with the single-resolution method are confirmed also when $N = N_{max} = 3$ scatterers are present. A representative result provided by the *BARE* and the *IMSA-3D* approaches dealing with this more critical scenario are shown in Fig. 3.11(c) and Fig. 3.11(d), respectively. As it can be observed, the *IMSA-3D* is still able to detect three RoIs and to fairly estimate the object positions, although the object located in ($x_{obj}^{(3)} = 2.40 \lambda$, $y_{obj}^{(3)} = 1.20 \lambda$, $z_{obj}^{(3)} = -0.18 \lambda$) is detected with a greater *object-localization-error* $v_3^{(2)} = 0.92 \lambda$ if compared with the two remaining objects [$v_1^{(2)} = 0.52 \lambda, v_2^{(2)} = 0.41 \lambda$]. Once again, the performance of the multi-resolution procedure outperforms the single-step approach capabilities in discerning multiple objects as clearly pointed out by the very high *volume-occupation* index of the single RoI identified by the *BARE* approach [$\xi_1^{(BARE)} = 28.74$].

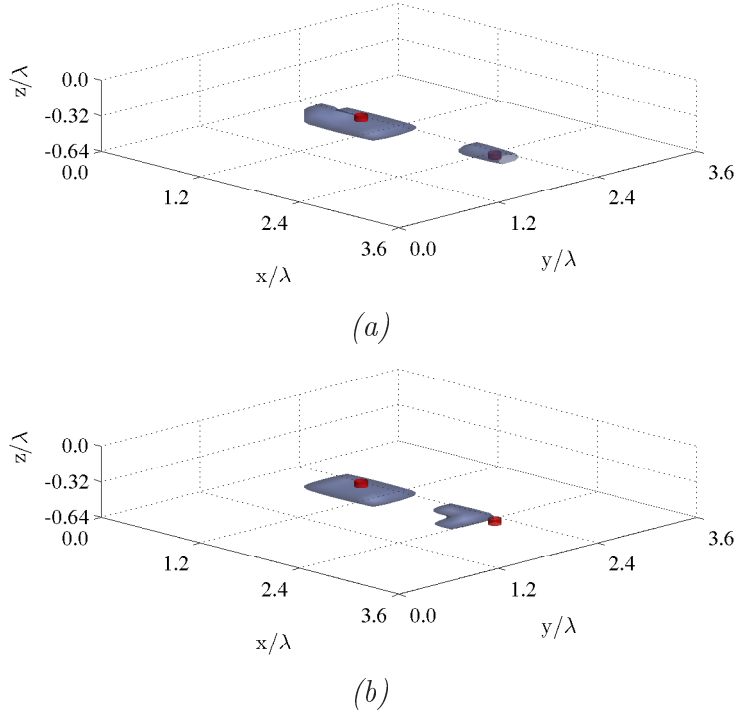


Figure 3.12: *Complex scenario* - Probability maps determined by the *IMSA-3D* [$m = M_{opt} = 3$] approach with small objects ($N = 2$) buried in dry sandy soil (a) and dry clay soil (b).

3.3.4 Complex scenarios

The multiple object detection performance have been also tested with different electric and geometrical characteristics of the scatterers and the background. As an example, a more complex scenario with smaller objects ($R_{obj}^{(n)} = 0.1 \lambda$ and $H_{obj}^{(n)} = 0.09 \lambda$, $n = 1, \dots, N$) is considered both for training and test dataset. Figure 3.12 shows the results provided by the *IMSA-3D* in correspondence of two different background characteristics with multiple objects ($N = 2$) and noisy data ($P_{noise} = 0.1 V/m$). The first example [Fig. 3.12(a)] refers to a configuration with small objects buried into dry sandy soil ($\varepsilon_r^\Omega = 4.0$ and $\sigma^\Omega = 4.0 \times 10^{-3}$), while the second [Fig. 3.12(b)] deals with the same objects in a soil background with an increased water content that causes an increase in relative permittivity ($\varepsilon_r^\Omega = 16.0$) and in conductivity ($\sigma^\Omega = 3.0 \times 10^{-2}$) [43]. The comparison in terms of *object-localization-error* points out a slightly worst detection of smaller objects in sandy soil. Nevertheless, there is not a significant change in the error statistics with the considered soils and objects, since the average value of *object-localization-error* remains always lower than $mean_n \left\{ v_n^{(2)} \right\} = 0.98 \lambda$, $n = 1, 2$.

3.4 Conclusions

The proposed method consists of a multi-resolution approach for the real-time detection of three-dimensional buried objects. An SVM-based classifier has been suitably trained with available labeled data in order to obtain a probability map of single and multiple objects presence. Starting from a coarse resolution map, the iterative procedure performs a synthetic zoom on those spatial regions where potential objects are supposed to be located, thus increasing the detection resolution only in the RoIs. The effectiveness of the proposed methodology has been preliminary assessed with different subsurface scenarios, characterized by single and multiple objects, both in noiseless and noisy conditions.

The obtained results confirm that the SVM-based methodology allows one to estimate the objects presence in real-time and with a good degree of accuracy in terms of localization error. The multi-resolution strategy detects and locates single and multiple targets not belonging to the training set and also estimates the objects size with outperforming precision if compared with the single-step approach.

3.4. CONCLUSIONS

Chapter 4

Early Breast Cancer Imaging

Microwave imaging for breast cancer screening is an emerging technique as a valuable alternative to standard X-ray mammography. Usually, the solution to the nonlinear inverse problem is provided with iterative methods which require a forward solver execution at each iteration and particular attention to computational efficiency is fundamental. Recently, alternative techniques based on learning-by-example methodologies have been applied to imaging problems looking for real-time processing. In this chapter, a multiresolution approach for real-time detection of breast cancer is presented. A SVM-based classifier is integrated in an iterative multistep strategy to obtain a probability map of presence with enhanced spatial resolution where targets are supposed to be located. The scattering matrix measured at the output of a three-dimensional imaging system represents the input data of the customized classifier. A selected set of numerical results is provided in order to assess the effectiveness of the proposed approach dealing with both single and multiple inclusions. The performance of the method in cases of noisy data is also investigated.

4.1 Introduction

Breast cancer detection by means of microwave imaging has been developed rapidly in the last years because of the well-known limitations of the standard screening X-ray mammography in terms of sensitivity and false positive detections [44]. Among the advantages of microwave imaging are the non-ionizing and low-power radiation [45] as well as the absence of compression that means patient comfort as already proven during clinical investigations [46]. This imaging modality is based on the contrast between the constitutive parameters of healthy and malignant breast tissues in the microwave frequency range, the reason that why the detection with high accuracy of small tumors is possible [47]. In microwave tomography, nonlinear inverse scattering techniques based on Maxwell's equations are often used [57, 60] and they are usually based on iterative algorithms in which a full scattering problem must be solved at each iteration leading to considerable computational load [50], especially when three-dimensional geometries with large number of unknowns are considered. Alternatively, moving from deterministic to stochastic methods such as Particle Swarm Optimization (PSO) and Genetic Algorithms (GAs), the detection problem is recast as an optimization problem [51]. However, even if these methodologies find global minimum of a given cost function, the computational load is still high.

Nowadays, progress in machine learning suggests the solution of medical imaging problems by means of Learning-by-Example (LBE) methodologies [52]-[54]. These kind of classification or regression-based algorithms are particularly appropriate for a wide-range of real-time applications thanks to their high-speed properties and generalization capabilities. Given a learning task and a finite set of training samples, the inverse problem can be recast as a constrained quadratic optimization problem whose optimal solution can be found avoiding the ill-posedness and nonlinearity of the inverse scattering problem.

In this work, the inversion process is reformulated as a multiresolution classification procedure based on a binary support vector machine (SVM) classifier integrated in an iterative multistep strategy [59]. Accordingly, a multiresolution probability map of pathology presence is estimated with increased accuracy in those high-probability spatial regions where the inclusions are supposed to be located. More specifically, starting from the knowledge of a finite-size training set where the pathology is randomly positioned, the first step is aimed at defining a coarse probability map. The successive steps iteratively identify the areas with highest probability values where the resolution level increases. Concerning the training phase, it is performed only once after an ad-hoc calibration procedure that finds the best parameters in order to maximize the generalization capabilities of the optimal separating hyperplane. Numerical differential data have been calculated starting from the elements of the scattering matrix available at the output of the considered multiview imaging system.

This chapter is organized as follows. The geometry and the characteristics of

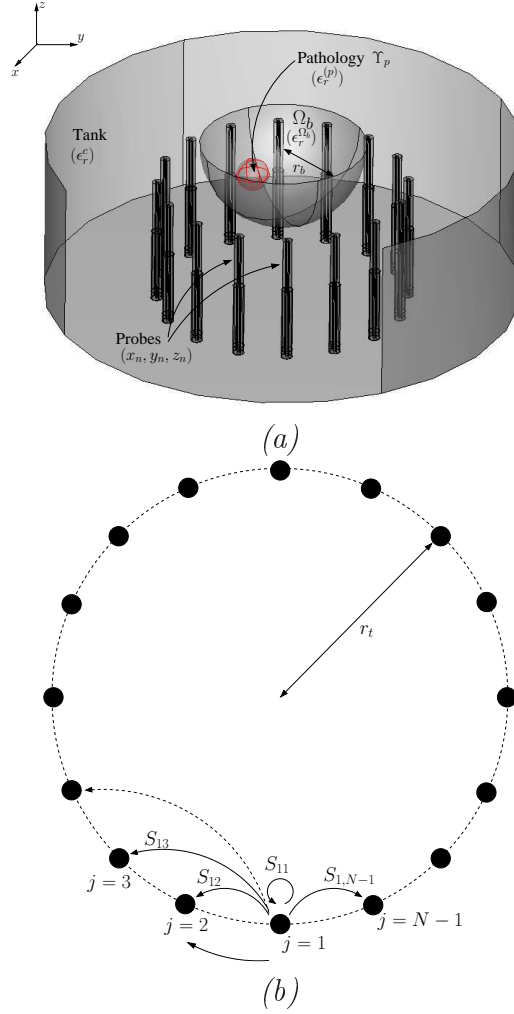


Figure 4.1: Three-dimensional model geometry (a) and top view of the multi-view measurement system (b).

the measurement system as well as the format of the simulated numerical data are described in Section 4.2. In Sect. 4.3 the proposed multiresolution based on a SVM classifier is formulated. In order to show the effectiveness and the current limitations of the proposed approach, a selected set of numerical results concerned with the detection of both single and multiple inclusions is reported (Sect. 4.4). The robustness and the generalization capabilities in presence of noisy data and different breast characteristics have been also tested. Finally, some conclusion about the innovative features of the approach are drawn in Sect. 4.5.

4.2 Numerical Model

Let us consider a three-dimensional imaging system as shown in Fig. 4.1(a). It consists of N monopole probes disposed in a circular array of radius r_t at known positions (x_n, y_n, z_n) , $n = 1, \dots, N$. The antennas are placed in a tank filled with a coupling liquid in order to minimize the reflection from air-breast skin interface [55]. The complex relative dielectric properties of the coupling medium can be expressed as

$$\varepsilon_r^c = \varepsilon_r' - j\varepsilon_r'' \quad (4.1)$$

ε_r' being the relative permittivity and $\varepsilon_r'' = \frac{\sigma}{\varepsilon_0 2\pi f}$ the out-of-phase loss factor, where σ is the conductivity, ε_0 the free-space permittivity and f the working frequency. The coupling liquid has dielectric properties similar to those of the breast, which is modeled as a hemispherical domain Ω_b , suspended on the top of the tank and with radius r_b . Assuming a reference system with origin in the centre of the hemisphere representing Ω_b , a set of regions $\Upsilon_p \in \Omega_b$, $p = 1, \dots, P$ centered in $(x, y, z)_{\Upsilon}^{(p)}$ can reside into the imaging domain defining the dielectric profile of the breast

$$\Pi(x, y, z) = \begin{cases} \varepsilon_r^{(p)} - \varepsilon_r^{\Omega_b}(x, y, z), & \text{if } (x, y, z) \in \Upsilon_p; p = 1, \dots, P \\ 0, & \text{otherwise} \end{cases} \quad (4.2)$$

with $\varepsilon_r^{(p)}$, $p = 1, \dots, P$ and $\varepsilon_r^{\Omega_b}$ being the complex relative dielectric constant of Υ_p , $p = 1, \dots, P$ and Ω_b , respectively.

Each antenna acts as transmitter and receiver in order to perform a multiview measurement of the total electromagnetic field

$$\underline{E}_{tot}(\underline{r}_{rx}|\underline{r}_{tx}) = \underline{E}_{inc}(\underline{r}_{rx}|\underline{r}_{tx}) + j2\pi f \varepsilon_r^{\Omega_b} \int_{\Omega_b} \underline{G}(\underline{r}_{rx}; \underline{r}) \cdot \Pi\{\underline{r}|\Upsilon_p, \varepsilon_r^{(p)}\} \cdot \underline{E}(\underline{r}|\underline{r}_{tx}) \cdot d\underline{r} \quad (4.3)$$

where $\underline{r}_{rx} = (x_{rx}, y_{rx}, z_{rx})$, $rx = 1, \dots, N|_{rx \neq tx}$ and $\underline{r}_{tx} = (x_{tx}, y_{tx}, z_{tx})$, $tx = 1, \dots, N$ are the positions of the receiving and transmitting probes, respectively. $\underline{E}_{inc}(\underline{r}_{rx}|\underline{r}_{tx})$ is the field measured in absence of regions Υ_p inside Ω_b , \underline{G} is the Green's function of the inhomogeneous medium [100] and $\underline{E}(\underline{r}|\underline{r}_{tx})$ is the electric field inside Ω_b in presence of scattering regions Υ_p ; $p = 1, \dots, P$.

Since a realistic imaging system is simulated, let us suppose to measure the field in the form of scattering parameters $s_{rx,tx}$, $rx, tx = 1, \dots, N$ at the ports of the receiving probes (also reflection coefficients $s_{tx,tx}$, $tx = 1, \dots, N$ are available) [Fig. 1(b)]. As formulated by Yu *et al.* in [57], the fields \underline{E}_{tot} and \underline{E}_{inc} can be related to the s -parameters as

$$s_{rx,tx}^{tot} = C_0 \hat{a}_{rx} \cdot \underline{E}_{tot}(\underline{r}_{rx}|\underline{r}_{tx}) \quad (4.4)$$

and

$$s_{rx,tx}^{inc} = C_0 \hat{a}_{rx} \cdot \underline{E}_{inc}(\underline{r}_{rx}|\underline{r}_{tx}), \quad (4.5)$$

taking into account the orientations [i.e., \hat{a}_{rx}] of the receiving antennas and a complex calibration parameter C_0 .

Hence, from the knowledge of the scattering matrices $\underline{\underline{S}}^{tot} \in \mathbb{C}^{N \times N}$ and $\underline{\underline{S}}^{inc} \in \mathbb{C}^{N \times N}$ measured in presence and absence of the scattering regions Υ_p ; $p = 1, \dots, P$, respectively, the following differential quantity

$$s_{rx,tx}^\Delta = \frac{s_{rx,tx}^{tot} - s_{rx,tx}^{inc}}{s_{rx,tx}^{inc}} \quad rx, tx = 1, \dots, N \quad (4.6)$$

represents the normalized contribution scattered by Υ_p ; $p = 1, \dots, P$. The inverse scattering problem can be thought as the retrieval of target positions $(x, y, z)_{\Upsilon}^{(p)}$ on the basis of the known $\frac{N(N-1)}{2}$ elements

$$\underline{\underline{\Gamma}}_s = \{s_{rx,tx}^\Delta; rx = 1, \dots, N; tx = 1, \dots, N; tx \leq rx\}$$

of the lower triangular part of $\underline{\underline{S}}^\Delta$, since the elements of the scattering matrix $\underline{\underline{S}}^\Delta \in \mathbb{C}^{N \times N}$ are supposed to be $s_{rx,tx}^\Delta = s_{tx,rx}^\Delta$, $rx, tx = 1, \dots, N$. It can be profitably solved by means of the learning-by-example methodology that estimates the unknown inverse mapping following the guidelines of the multi-step strategy detailed in the following.

4.3 Multi-resolution SVM-based approach

The arising problem is that of determining a probability risk-map of Ω_b starting from the knowledge of the measured data. Towards this end, a three-dimensional domain enclosing Ω_b is partitioned in a uniform lattice of C training cells whose barycenters are (x_c, y_c, z_c) , $c = 1, \dots, C$. Each cell can assume a binary state $\alpha_c \in \{-1, +1\}$ in order to recast the detection problem in a binary classification problem whose classes stand for presence [$\alpha_c = +1$] and absence [$\alpha_c = -1$] of the target inside the cells. Once the training of the SVM-based procedure is completed, unseen input test data $\underline{\underline{\Gamma}}_s$ can be classified and the a-posteriori probability $P_m = Pr\{\alpha_m = +1 | \underline{\underline{\Gamma}}_s\}$, $m = 1, \dots, M$ is evaluated, M being the number of test cells that can differ from the C training cells. The training phase of the proposed method as well as the iterative procedure for the multi-resolution risk-map evaluation are detailed in the following sections.

4.3.1 SVM Training phase

Let us consider a supervised binary classification problem. The training set composed by T samples $\underline{x}_t \in \mathbb{R}^L$, $t = 1, \dots, T$, $L = \frac{N(N-1)}{2} + 3$ being the dimension of the input features space \mathcal{X} , is associated with output labels $y_t \in \{-1, +1\}$, $t = 1, \dots, T$ and represented as

$$\begin{aligned} \Psi &= \{\underline{x}_t, y_t; t = 1, \dots, T\} = \\ &= \left\{ [(x_c, y_c, z_c), \underline{\underline{\Gamma}}_s, \alpha_c; c = 1, \dots, C]^{(t)}, t = 1, \dots, T \right\}. \end{aligned} \quad (4.7)$$

4.3. MULTI-RESOLUTION SVM-BASED APPROACH

Since the measured data $\underline{\Gamma}_s^{(t)}$ are highly linearly nonseparable as commonly happens for real-world data, the input vectors are mapped with a kernel method in a higher L' -dimensional space \mathcal{X}' ($L' > L$) through the nonlinear function $\underline{\rho}(\bullet)$ in order to find the linear decision function

$$\Phi [(x_m, y_m, z_m), \underline{\Gamma}_s] = \underline{w} \cdot \underline{\rho} [(x_m, y_m, z_m), \underline{\Gamma}_s] + b, \quad m = 1, \dots, M \quad (4.8)$$

in the transformed space \mathcal{X}' able to correctly classify the unseen test data $[(x_m, y_m, z_m), \underline{\Gamma}_s; m = 1, \dots, M]$. The unknown weight vector $\underline{w} \in \mathbb{R}^{L'}$ and the threshold b univocally define the optimal hyperplane associated with $\Phi(\bullet)$ and are evaluated through the minimization of the cost function

$$\Theta(\underline{w}, \underline{\xi}) = \frac{1}{2} \|\underline{w}\|^2 + \zeta \sum_{t=1}^T \sum_{c=1}^C \xi_c^{(t)} \quad \begin{array}{l} t = 1, \dots, T \\ c = 1, \dots, C \end{array} \quad (4.9)$$

subject to the constraints

$$\begin{aligned} \alpha_c^{(t)} \left(\underline{w} \cdot \underline{\rho} [(x_c, y_c, z_c), \underline{\Gamma}_s^{(t)}] + b \right) &\geq 1 - \xi_c^{(t)} \\ \xi_c^{(t)} &\geq 0 \end{aligned} \quad (4.10)$$

where the constant ζ is a user-defined regularization parameter that controls the trade-off between margin maximization and training errors minimization, regulated by the first and the second terms of (4.9), respectively, $\underline{\xi}$ is the vector of slack variables used to relax the separation constraint in (4.10) and thus allowing the possibility of examples violating it. Making slack variables large enough, it is always possible to minimize the cost function in (4.9) but large values of $\xi_c^{(t)}$ are consequences of strongly overlapped classes and it is possible that the hyperplane will not generalize well [1]. The minimization of the cost function is an optimization problem that can be reformulated through the Lagrangian

$$\mathcal{L}(\underline{w}, b, \underline{\mu}) = \frac{1}{2} \|\underline{w}\|^2 - \sum_{t=1}^T \sum_{c=1}^C \mu_c^{(t)} \left[\alpha_c^{(t)} \left(\underline{w} \cdot \underline{\rho} [(x_c, y_c, z_c), \underline{\Gamma}_s^{(t)}] + b \right) - 1 \right] \quad (4.11)$$

with lagrange multipliers vector $\underline{\mu} = (\mu_c^{(t)}, c = 1, \dots, C; t = 1, \dots, T)$ that can be found by means of a dual form of the optimization problem

$$\max_{\underline{\mu}} \left\{ \sum_{t=1}^T \sum_{c=1}^C \mu_c^{(t)} - \frac{1}{2} \sum_{t=1}^T \sum_{c=1}^C \sum_{t'=1}^T \sum_{c'=1}^C \mu_c^{(t)} \mu_{c'}^{(t')} \alpha_c^{(t)} \alpha_{c'}^{(t')} \mathcal{K} [(x_c, y_c, z_c), \underline{\Gamma}_s^{(t)}; (x_{c'}, y_{c'}, z_{c'}), \underline{\Gamma}_s^{(t')}] \right\} \quad (4.12)$$

under the constraints

$$\begin{aligned} \mu_c^{(t)} &\geq 0 \\ \sum_{t=1}^T \sum_{c=1}^C \mu_c^{(t)} \alpha_c^{(t)} &= 0 \end{aligned} .$$

$\mathcal{K}(\cdot; \cdot)$ being the kernel function. The support vectors (*SVs*) are those examples in the training set for which $0 < \mu_c^{(t)} \leq \zeta$. In particular, they can be splitted in normal support vectors (*NSVs*) [$0 < \mu_c^{(t)} < \zeta$] and bounded support vectors (*BSVs*) [$\mu_c^{(t)} = \zeta$]. In particular, the *BSVs* are examples that lie in margin and represent the aforementioned training errors.

Once the training phase is terminated, the decision function can be expressed in terms of the test data in the original input space

$$\begin{aligned} & \Phi[(x_m, y_m, z_m), \underline{\Gamma}_s] = \\ & = \sum_{t=1}^{\hat{T}} \sum_{c=1}^{\hat{C}} \mu_c^{(t)} \alpha_c^{(t)} \mathcal{K}[(x_c, y_c, z_c), \underline{\Gamma}_s^{(t)}; (x_m, y_m, z_m), \underline{\Gamma}_s] + b, \quad m = 1, \dots, M \end{aligned}$$

where $\hat{T} \leq T$ and $\hat{C} \leq C$ quantify the subset of data for which $0 < \mu_c^{(t)} \leq \zeta$, i.e., the sum of *NSVs* and *BSVs*.

4.3.2 Multi-resolution Test Phase

The test phase is aimed at the detection of regions Υ_p ; $p = 1, \dots, P$ starting from unseen test data $[(x_m, y_m, z_m), \underline{\Gamma}_s]$, $m = 1, \dots, M$. According to the Platt's probabilistic outputs for SVM [58], the output of the unthresholded decision function $\Phi([(x_m, y_m, z_m), \underline{\Gamma}_s])$ can be mapped in a sigmoid function in order to define the probability

$$P_m = \frac{1}{1 + \exp(a \Phi[(x_m, y_m, z_m), \underline{\Gamma}_s] + d)} \quad m = 1, \dots, M \quad (4.13)$$

that the object belongs to the m -th cell, a and d being parameters evaluated according to the algorithm in [58]. The approximation of the probability distribution

$$\mathcal{P}(x, y, z) = \sum_{m=1}^M P_m F_m(x, y, z) \quad (4.14)$$

is the linear combination of non-overlapping spatial basis-functions

$$F_m(x, y, z) = \begin{cases} 1 & \text{if } (x, y, z) \in m\text{-th cell} \\ 0 & \text{otherwise} \end{cases} \quad (4.15)$$

weighted by the probability values.

In order to improve the achievable spatial resolution, the estimation of $\mathcal{P}(x, y, z)$ is evaluated exploiting the iterative process [59] aimed at defining a multiresolution lattice of test cells leading to the multiresolution representation

$$\mathcal{P}^{(s)}(x, y, z) = \sum_{r=0}^{R(s)} \sum_{m(r)=1}^{M(r)} P_{m(r)}^{(s)} F_{m(r)}(x, y, z); \quad s = 1, \dots, S \quad (4.16)$$

where $s = 1, \dots, S$ is the step index of the iterative procedure that stops when the desired spatial resolution regulated by the resolution index $r = 0, \dots, R(s)$

4.3. MULTI-RESOLUTION SVM-BASED APPROACH

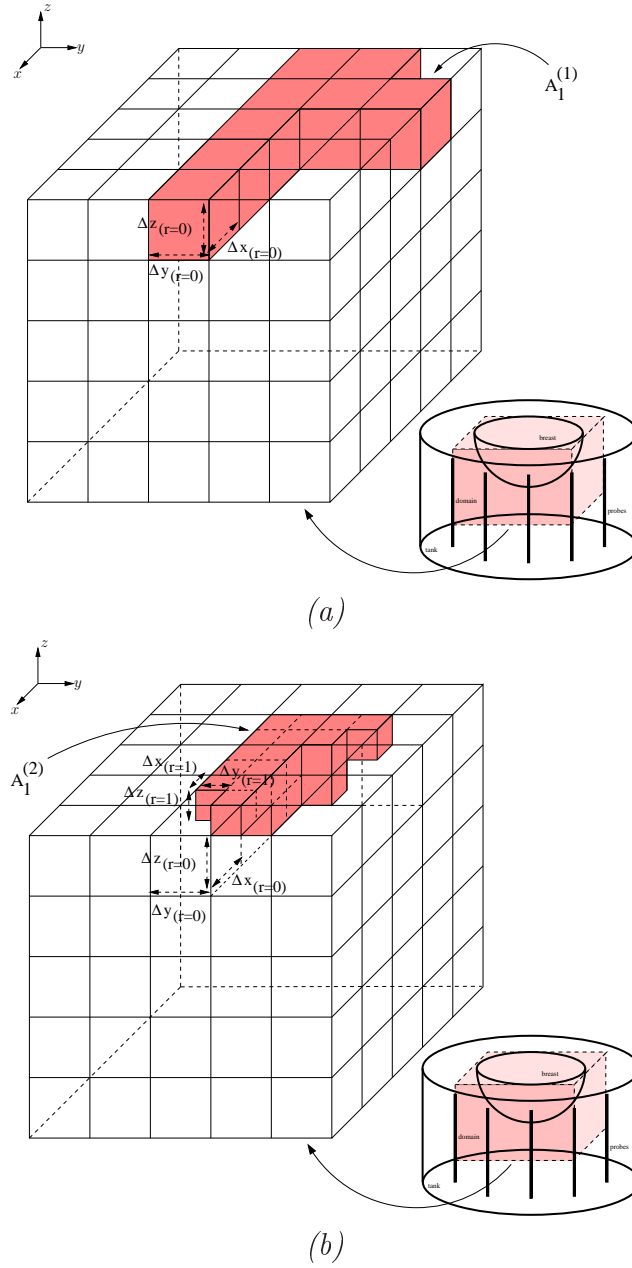


Figure 4.2: *IMSA Procedure* - AoI detection at $s = 1$ (a) and $s = 2$ (b) multi-resolution steps.

is achieved and $R(s) = s - 1$. At the r -th resolution level and s -th scaling step, $m(r) = 1, \dots, M(r)$ basis-functions are generated, being $r(s) = s - 1$. Figure 2 pictorially shows the generation of the so-called areas of interest (*AoIs*) $A_k^{(s)}$, $k = 1, \dots, K(s)$, $K(s)$ being the total *AoIs* at step s , at step $s = 1$ [Fig. 4.2(a)] and step $s = 2$ [Fig. 4.2(b)]. In order to better understand the definition of the multiresolution probability function, the iterative classification procedure is detailed for the first step $s = 1$ and higher steps $s > 1$.

Step $s = 1$ - Coarse Detection. At the first step the *AoI* $A_1^{(1)}$ is equivalent to the whole three-dimensional domain that encloses Ω_b and the basis-functions defining the $M(r)$ test cells are of the largest characteristic length scale [$r = 0$, Fig. 4.2(a)]. This step provides a first and inaccurate estimation of the a-posteriori probability upon which the successive steps aim at locating the small length scale *AoIs*.

Step $s > 1$ - *AoIs* Identification. From the knowledge of the probabilities evaluated at the previous step $s - 1$, the resolution of the lattice is increased only in those cells where the probability of target presence is higher than a predefined threshold ϵ . In order to obtain a suitable thresholded probability function, a normalized version is introduced

$$\mathcal{P}_{norm}^{(s-1)}(x, y, z) = \sum_{r=0}^{R(s-1)} \sum_{m(r)=1}^{M(r)} Q_{m(r)}^{(s-1)} F_{m(r)}(x, y, z) \quad (4.17)$$

where

$$Q_{m(r)}^{(s-1)} = \frac{P_{m(r)}^{(s-1)} - P_{min}^{(s-1)}}{P_{max}^{(s-1)} - P_{min}^{(s-1)}}, \quad \begin{array}{l} m(r) = 1, \dots, M(r) \\ r = 0, \dots, R(s) \end{array} \quad (4.18)$$

$P_{min}^{(s-1)}$ and $P_{max}^{(s-1)}$ being the minimum and maximum probability values evaluated until step $s - 1$, respectively. The normalized values $Q_{m(r)}^{(s-1)} \geq \epsilon$ are the probabilities associated to those cells constituting the *AoIs* $A_k^{(s)}$, $k = 1, \dots, K(s)$, the remaining $Q_{m(r)}^{(s-1)} < \epsilon$ are nulled.

Step $s > 1$ - Multiresolution detection. The spatial resolution is enhanced in the identified *AoIs* $A_k^{(s)}$, $k = 1, \dots, K(s)$ by increasing the resolution index ($r \leftarrow r + 1$) and thus refining the probability function representation only where needed. To this end, (4.16) is updated by computing the coefficients $P_{m(r)}^{(s)}$ only if $(x, y, z)_{m(r)} \in A_k^{(s)}$, $k = 1, \dots, K(s)$. The iterative synthetic zooming is stopped when the number of the *AoIs* do not change between two consecutive steps [$K(s) = K(s - 1)$] and the size changes of the *AoIs* are smaller than the highest resolution level [$\Delta_s^{\Omega_b} < \min \{ \Delta x_{m(r)}^{(s)}, \Delta y_{m(r)}^{(s)}, \Delta z_{m(r)}^{(s)} \}$].

4.4 Numerical Results

The presented numerical experiments deal with the three-dimensional tomographic configuration as shown in Fig. 4.1. The imaging system consists of a circular array composed by $N = 16$ monopole antennas equally spaced on a $r_t = 0.27\lambda$ radius circle, λ being the wavelength at the working frequency $f = 1.1\text{GHz}$. The probes surround the hemispherical domain Ω_b of radius $r_b = 0.18\lambda$ simulating a *Heterogeneously Dense* breast with relative dielectric constant $\varepsilon_r^b = 17.72 - j15.41$. Spherical inclusions of radius $r_p = 3.67 \times 10^{-2}\lambda$ and electric characteristic $\varepsilon_r^p = 53.46 - j18.26$ represent the regions $\Upsilon_p \in \Omega_b$, $p = 1, \dots, P$ centered in $(x, y, z)_{\Upsilon}^{(p)}$. The breast as well as the probes are immersed in a coupling liquid ($\varepsilon_r^c = 23.43 - j18.48$) mimicking the average constitutive parameters of the breast.

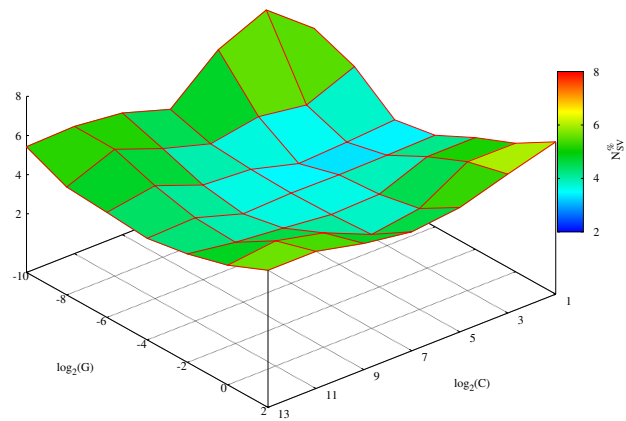
In the following section the SVM training procedure and the parameter selection are described (Sect. 4.4.1). Successively, the advantages and the current limitations of the proposed approach when dealing with single inclusion are analyzed (Sect. 4.4.2). In such a framework, the performances in presence of both noisy data and different breast characteristics are evaluated. Finally, the reliability of the proposed approach in correspondence with multiple inclusions is verified (Sect. 4.4.3).

4.4.1 Training Set and Model Selection

The collection of $T_p = 100$, $p = 1, \dots, P$ training configurations is obtained by randomly varying the position of Υ_p , $p = 1, \dots, P$ inside Ω_b , where $P = 2$ is the maximum number of considered regions. The imaging system collects the data $\underline{\Gamma}_s^{(t)}$, $t = 1, \dots, T_p$ for each configuration and the corresponding pathology positions are mapped into the states α_c , $c = 1, \dots, C$, $C = 108$ being the number of training cells. Two independent SVMs has been trained for single target ($P = 1$) and multiple targets ($P = 2$) test cases. Because of the good performances generally achieved by nonlinear SVM with gaussian kernel, the considered examples deal with the kernel

$$\begin{aligned} & \mathcal{K} \left[(x_c, y_c, z_c), \underline{\Gamma}_s^{(t)}; (x_{c'}, y_{c'}, z_{c'}), \underline{\Gamma}_s^{(t')} \right] = \\ & = \exp \left\{ -\gamma \left\| \left[(x_c, y_c, z_c), \underline{\Gamma}_s^{(t)} \right] - \left[(x_{c'}, y_{c'}, z_{c'}), \underline{\Gamma}_s^{(t')} \right] \right\|^2 \right\} \end{aligned} \quad (4.19)$$

where γ represents the width. In order to optimize the performances of the SVM-based methodology, the model selection issue has to be solved through the determination of the best regularization parameter ζ and kernel parameter γ . Frequently, the parameter selection is done empirically leading to suboptimal performances of classifiers. In this work, a cause and effect analysis of parameters influence on the decision function generation has been performed. In particular,



(a)

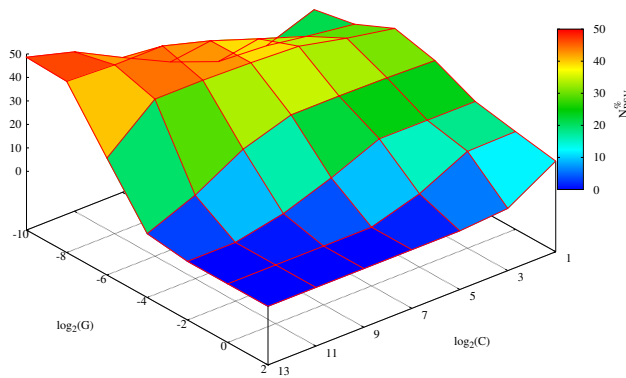


Figure 4.3: *SVM Parameter Calibration* - Support vector N_{NSV} and bounded support vector N_{BSV} analysis vs SVM Hyperparameters.

4.4. NUMERICAL RESULTS

the number of support vectors N_{SV} and bounded support vectors N_{BSV} are considered good indicators of SVM generalization capabilities since small N_{SV} leads to a structural simplification of the decision function thanks to the removal of the redundant elements [6]. Moreover, small N_{BSV} means less training errors as previously explained in Sect. 4.3.1. Therefore, the percentage indexes

$$N_{SV}^{\%} = \frac{N_{SV}}{(T_p \times C)} \times 100 \quad (4.20)$$

and

$$N_{BSV}^{\%} = \frac{N_{BSV}}{N_{SV}} \times 100 \quad (4.21)$$

are evaluated versus the user-defined parameters ζ and γ as shown in Fig. 4.3. As it can be seen, a range where both the indexes $N_{SV}^{\%}$ and $N_{BSV}^{\%}$ are low exists leading to a simple decision function and with few training errors. The reported results have been obtained with training parameters belonging to the aforementioned range. In particular, they have been set to $\zeta = 100$ and $\gamma = 1$.

4.4.2 Single Inclusion - Numerical Assessment

This section deals with the detection of a single inclusion by means of the proposed multiresolution procedure (*IMSA*) compared with the standard single resolution probability estimation (*BARE*). The performances have been evaluated on a test set composed by $T_{test} = 50$ examples and are quantified by computing the analytical indexes

$$\varepsilon_p^{(s)} = \sqrt{\left(x_{\Upsilon}^{(p)} - \hat{x}_p^{(s)}\right)^2 + \left(y_{\Upsilon}^{(p)} - \hat{y}_p^{(s)}\right)^2 + \left(z_{\Upsilon}^{(p)} - \hat{z}_p^{(s)}\right)^2} \quad (4.22)$$

and

$$\tilde{v}_p^{(s)} = \frac{4}{3}\pi \left\{ \frac{\sum_{r=0}^{R(s)} \sum_{m(r)=1}^{M(r)} \left[\frac{Q_{m(r)}^{(s)} \varepsilon_{m(r)}^{(s)}}{\max_{m(r)} \{Q_{m(r)}^{(s)}\}} \right]}{\sum_{r=0}^{R(s)} \sum_{m(r)=1}^{M(r)} \left[\frac{Q_{m(r)}^{(s)}}{\max_{m(r)} \{Q_{m(r)}^{(s)}\}} \right]} \right\}^3 \times v_p^{-1} \quad (4.23)$$

representing the *localization index* and the *inclusion volume*, respectively. The *localization index* points out the geometrical distance between the actual inclusion positions $(x, y, z)_{\Upsilon}^{(p)}$ and the estimated coordinates

$$\begin{aligned} \hat{x}_p^{(s)} &= \frac{\sum_{r=0}^{R(s)} \sum_{m(r)=1}^{M(r)} Q_{m(r)}^{(s)} x_{m(r)}}{\sum_{r=0}^{R(s)} \sum_{m(r)=1}^{M(r)} Q_{m(r)}^{(s)}}, \\ \hat{y}_p^{(s)} &= \frac{\sum_{r=0}^{R(s)} \sum_{m(r)=1}^{M(r)} Q_{m(r)}^{(s)} y_{m(r)}}{\sum_{r=0}^{R(s)} \sum_{m(r)=1}^{M(r)} Q_{m(r)}^{(s)}}, \\ \hat{z}_p^{(s)} &= \frac{\sum_{r=0}^{R(s)} \sum_{m(r)=1}^{M(r)} Q_{m(r)}^{(s)} z_{m(r)}}{\sum_{r=0}^{R(s)} \sum_{m(r)=1}^{M(r)} Q_{m(r)}^{(s)}} \end{aligned} \quad (4.24)$$

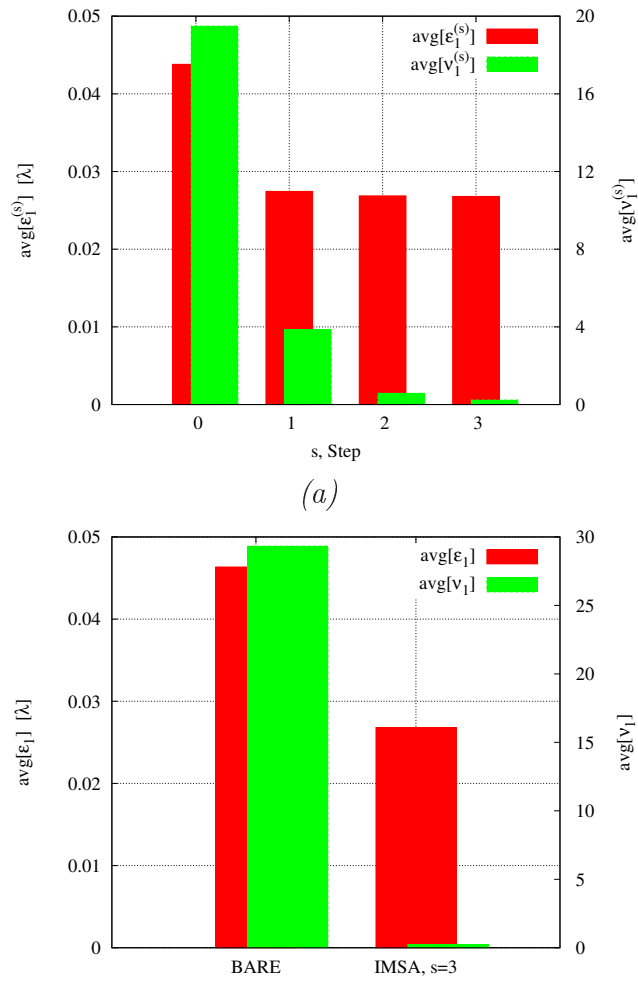


Figure 4.4: *IMSA Procedure* - Mean localization error and volume estimation vs multi-resolution steps (a) in comparison with BARE procedure (b).

4.4. NUMERICAL RESULTS

where the inclusions are supposed to be located. The *inclusion volume* index estimates the physical volume of the reconstructions normalized to the actual inclusion volumes v_p , $p = 1, \dots, P$, whereas

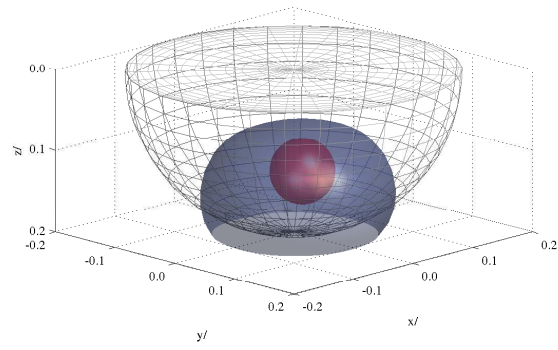
$$\varepsilon_{m(r)}^{(s)} = \sqrt{\left(x_{m(r)} - \hat{x}_p^{(s)}\right)^2 + \left(y_{m(r)} - \hat{y}_p^{(s)}\right)^2 + \left(z_{m(r)} - \hat{z}_p^{(s)}\right)^2}. \quad (4.25)$$

As a matter of fact, the behavior of the performance indexes points out that the *IMSA* strategy iteratively increases the detection capabilities both in terms of mean detection accuracy ($avg \left\{ \varepsilon_p^{(s)} \right\}$) and mean volume estimation ($avg \left\{ \tilde{v}_p^{(s)} \right\}$) as shown in Fig. 4.4(a) and also that it outperforms the *BARE* approach [Fig. 4.4(b)]. As a representative result, Fig. 4.5 graphically shows the estimated probability function of a test configuration with inclusion centered in $x_{\Upsilon}^{(1)} = 2.18 \times 10^{-4} \lambda$, $y_{\Upsilon}^{(1)} = 1.34 \times 10^{-2} \lambda$, $z_{\Upsilon}^{(1)} = -2.81 \times 10^{-2} \lambda$. The target reconstruction is represented by the surface that encloses the values of the probability function $\mathcal{P}_{norm}^{(s-1)}(x, y, z) > \varepsilon_{pr}$, where $\varepsilon_{pr} = 0.5$ is a user-defined probability threshold. As it can be noticed, the spherical region Υ_1 is correctly localized with *localization index* and *inclusion volume* both decreasing from $\varepsilon_1^{(1)} = 3.28 \times 10^{-2} \lambda$ and $\tilde{v}_1^{(1)} = 17.69$ to $\varepsilon_1^{(3)} = 1.95 \times 10^{-2} \lambda$ and $\tilde{v}_1^{(3)} = 1.13$, respectively.

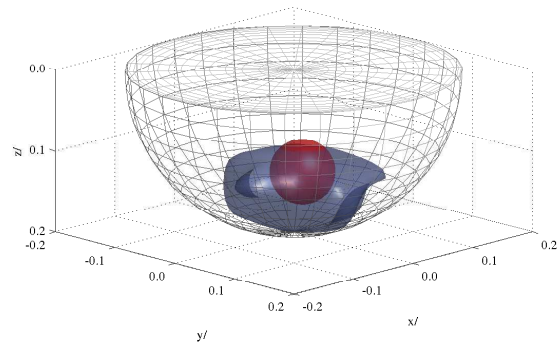
As a comparative result, the *BARE* approach has been applied to the same test example and starting from the same training set. The resolution level has been set to the highest achieved with the *IMSA* strategy, i.e., with discretization $\Delta x = \Delta y = \Delta z = \Delta_3^{\Omega_b}$ over all the domain Ω_b instead of only inside the *AoI* $A_1^{(3)}$. As it can be observed (Fig. 4.6), the volume of the reconstruction is significantly wider [$\tilde{v}_1^{(bare)} = 16.18$] and also the *localization index* is slightly worse [$\varepsilon_1^{(bare)} = 2.43 \times 10^{-2} \lambda$]. Moreover, it should be pointed out the computational save provided by the multiresolution approach that evaluates the decision function twenty times less than the *BARE* method and results to be more effective in terms of real-time capabilities.

4.4.2.1 Validation with Random Noise added to Synthetic Data

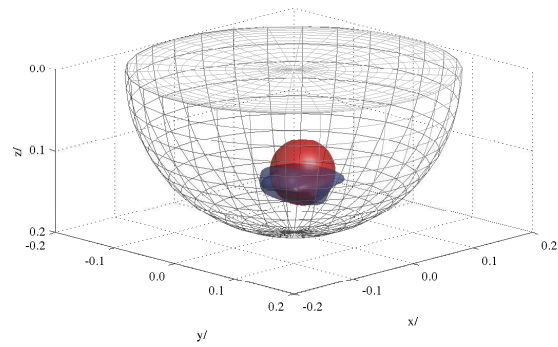
In order to test the robustness of the methodology in various and more realistic working conditions, also noisy measurements have been simulated by adding a Gaussian noise with an amplitude mimicking a noise floor of -100 dBm [60]. The transmission power has been varied in the range $10 \text{ dBm} \leq P_{tx} \leq 30 \text{ dBm}$ to simulate realistic field measurements with different signal-to-noise ratio (*SNR*) that depends from the chosen source power. The behavior of the error figures versus P_{tx} is shown in Fig. 4.7 in order to further confirm the detection accuracy of the proposed *IMSA* approach in dealing with noisy data. It can be noticed that the pathology is correctly localized with small *localization index* $avg \left\{ \varepsilon_1^{(3)} \Big|_{P_{tx}=15 \text{ dBm}} \right\} \leq 2.83 \times 10^{-2} \lambda$ and well-estimated *inclusion volume*



(a)



(b)



(c)

Figure 4.5: *IMSA Procedure* - Pathology detection obtained by *IMSA* procedure at $s = 1$ (a), $s = 2$ (b), $s = 3$ (c).

4.4. NUMERICAL RESULTS

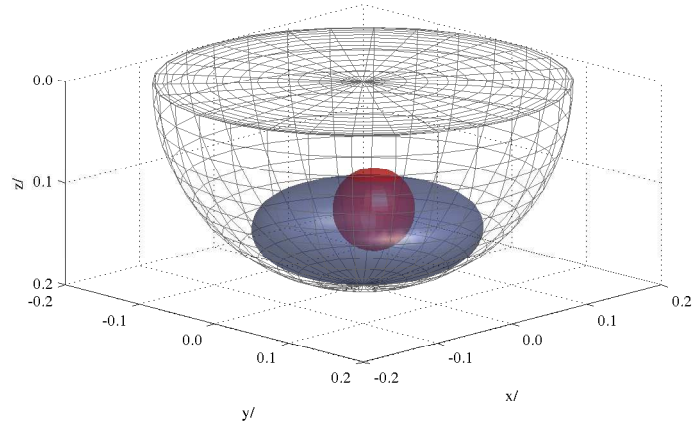


Figure 4.6: *IMSA vs BARE Detection* - Pathology detection determined by *BARE* procedure.

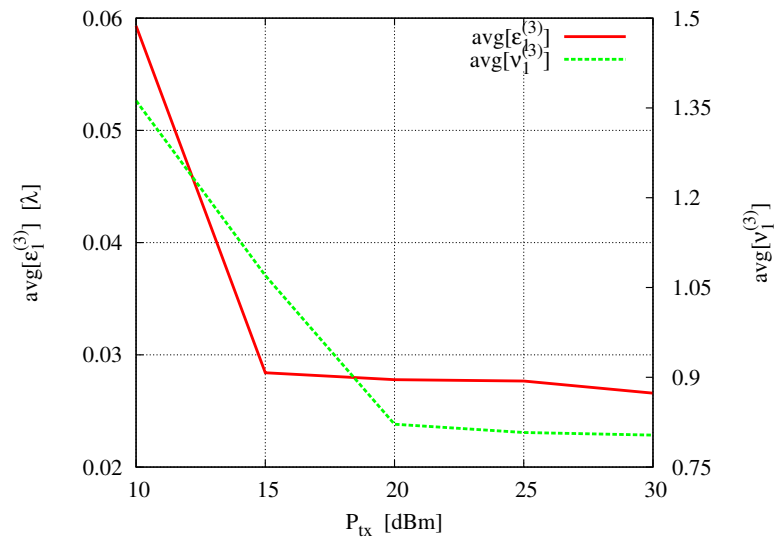


Figure 4.7: *Validation vs random noise* - Localization error and volume estimation versus transmission power P_{tx} (-100 dBm noise floor) .

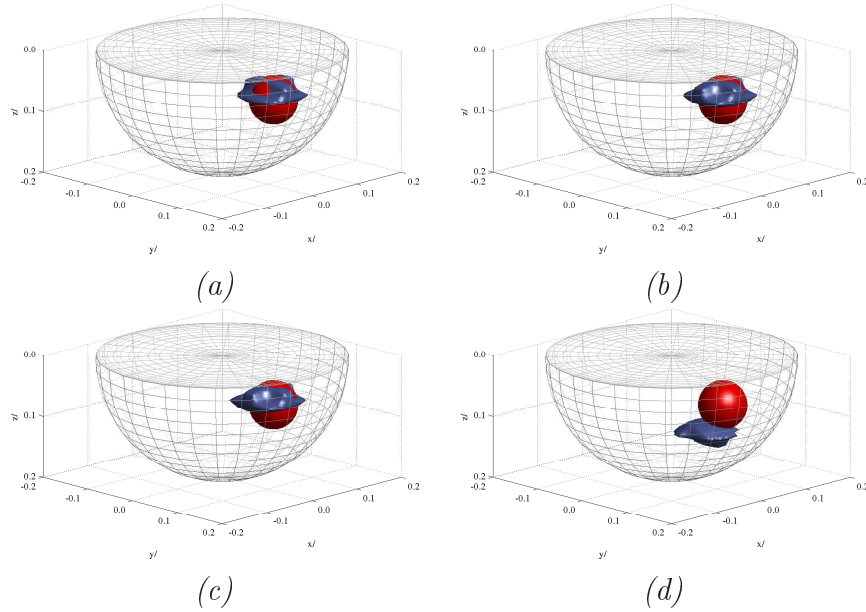


Figure 4.8: *Validation vs random noise* - Pathology detection determined by IMSA procedure with noisy data [$P_{tx} = 30 \text{ dBm}$ (a), $P_{tx} = 25 \text{ dBm}$ (b), $P_{tx} = 15 \text{ dBm}$ (c), $P_{tx} = 10 \text{ dBm}$ (d)].

$\left\{ \text{avg} \left\{ \tilde{v}_1^{(3)} \Big|_{P_{tx}=15\text{dBm}} \right\} \leq 1.11 \right.$ when $P_{tx} > 15 \text{ dBm}$, whereas for lower P_{tx} values the accuracy decreases showing maximum error values $\text{avg} \left\{ \varepsilon_1^{(3)} \Big|_{P_{tx}=10\text{dBm}} \right\} = 5.93 \times 10^{-2} \lambda$ and $\text{avg} \left\{ \tilde{v}_1^{(3)} \Big|_{P_{tx}=10\text{dBm}} \right\} = 1.36$. Figure 4.8 shows, in a comparative fashion, the inclusion reconstructions of a noisy test example obtained with different power values ranging from $P_{tx} = 30 \text{ dBm}$ [Fig. 4.8(a)] down to $P_{tx} = 10 \text{ dBm}$ [Fig. 4.8(d)]. Even if the reduction in detection accuracy is evident, the methodology still identifies the presence of the inclusion with acceptable errors [$\varepsilon_1^{(3)} \Big|_{P_{tx}=10\text{dBm}} = 5.24 \times 10^{-2} \lambda$ and $\tilde{v}_1^{(3)} \Big|_{P_{tx}=10\text{dBm}} = 1.09$].

4.4.2.2 Validation with Different Breast Properties

The examples under test are concerned with breast characteristics different from those in the training set. The aim of this section is to verify how the performances of a trained SVM changes when dealing with test data that belong to different test cases. More specifically, in addition to the *Heterogeneously Dense* (H) breast adopted for training data generation, let us consider also *Fatty* (F) [$\varepsilon_r^F = 9.06 - j6.90$] and *Scattered* (S) [$\varepsilon_r^S = 14.16 - j12.57$] breast models. The electrical characteristics of the inclusion are unchanged [$\varepsilon_r^p = 53.46 - j18.26$], leading to different contrasts between pathology and surrounding mediums. As for the

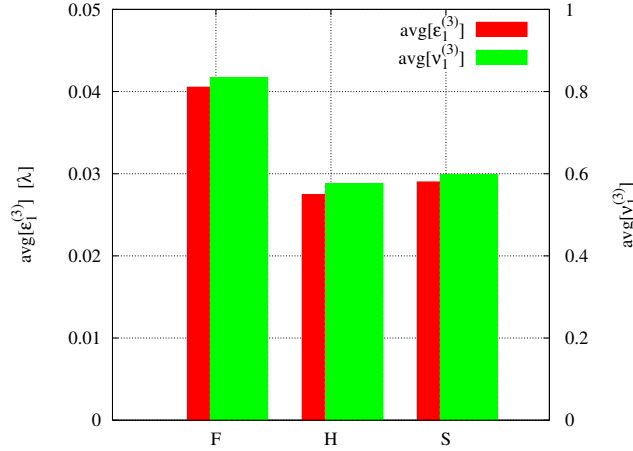


Figure 4.9: *Validation vs electrical properties of breast* - Localization error and volume estimation versus breast complex dielectric characteristics (F - H - S).

already considered H -breast test case, a test set composed by $T_{test} = 50$ examples has been generated both for F -breast and S -breast and the error figures obtained with the *IMSA* methodology have been evaluated. Fig. 4.9 compares the mean *localization index* and *inclusion volume* of the three considered test cases (F , H , S) pointing out that the algorithm provides good reconstructions even if the change in electrical characteristics causes an error increase of $(\Delta\epsilon_1^{(3)})^F = 47\%$ and $(\Delta\tilde{v}_1^{(3)})^F = 44\%$ for the F -breast and of $(\Delta\epsilon_1^{(3)})^S = 6\%$ and $(\Delta\tilde{v}_1^{(3)})^S = 4\%$ for the S -breast respect to the H -breast initial test case.

4.4.3 Multiple Inclusions - *Performance analysis*

This section aims at assessing the effectiveness of the proposed *IMSA* methodology in detecting multiple inclusions. The imaging system configuration as well as the characteristics of the the breast and the inclusions are unchanged respect to the single-inclusion test case (with *Heterogeneously Dense* breast). Dealing with the detection of two equal inclusions, both in terms of electric and geometrical characteristics, the training and test data sets have been generated with the same number of regions ($P = 2$) and with the constraint on the randomly-chosen positions of the regions that cannot be overlapped. The generated data have been still blurred with random Gaussian noise, reproducing the same noise floor (-100 dBm) as for the previous noisy test cases and a source power $P_{tx} = 20$ dBm has been used. A representative test case has been chosen among the test set in order to show the probability maps estimated by the *IMSA* approach at different steps [Fig. 4.10(a)-(c)] together with that obtained with the single-resolution *BARE* classification procedure [Fig. 4.10(d)]. In such a

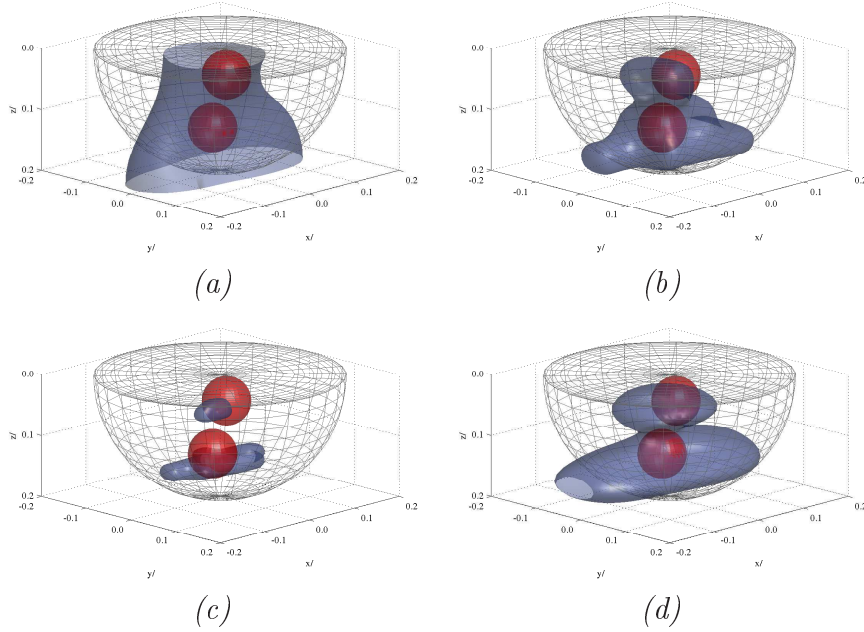


Figure 4.10: *Multiple detection* - Pathology detections determined by *IMSA* procedure at $s = 1$ (a), $s = 2$ (b), $s = 3$ (c) and by *BARE* approach (d).

case, the values of the error figures turn out to be equal to $\varepsilon_1^{(3)} = 2.91 \times 10^{-2} \lambda$, $\varepsilon_2^{(3)} = 3.08 \times 10^{-2} \lambda$ and $\tilde{v}_1^{(3)} = 0.89$, $\tilde{v}_2^{(3)} = 1.68$ when *IMSA* approach is applied, while the *BARE* method provides higher *localization index* $\varepsilon_1^{(bare)} = 3.12 \times 10^{-2} \lambda$, $\varepsilon_2^{(bare)} = 4.14 \times 10^{-2} \lambda$ and *inclusion volume* $\tilde{v}_1^{(bare)} = 5.71$, $\tilde{v}_2^{(bare)} = 9.93$. As expected, the outperforming behavior of the *IMSA* approach in comparison with the *BARE* procedure came out for the single-inclusion analysis is confirmed also for the multiple inclusions test case. The multi-step classification process correctly identifies the multiple *AoIs* and significantly enhance the resolution where the probability is higher. As it can be observed, the *IMSA* strategy avoids the clustering effect produced by the single-step resolution that is unable to identify two independent areas and estimates only one high-probability region. For completeness, by considering the whole test set, the statistics of the error figures are given in Tab. 4.1.

4.5 Conclusions

In this chapter, a multiresolution approach for the detection of breast cancer based on a SVM classifier has been presented. Once the training phase is completed, the detection of the pathology is real-time estimated through the generation of a multiresolution probability map of presence. The spatial resolution is iteratively enhanced only in those regions where the probability is higher.

4.5. CONCLUSIONS

<i>Method</i>	<i>Average Error Figures</i>			
	$\varepsilon_1^{(s)} \lambda$	$\tilde{v}_1^{(s)}$	$\varepsilon_2^{(s)} \lambda$	$\tilde{v}_2^{(s)}$
<i>IMSA</i>				
$s = 1$	3.89	15.41	4.59	16.33
$s = 2$	3.40	7.65	4.02	6.13
$s = S_{opt} = 3$	3.05	1.13	3.79	0.96
<i>BARE</i>	3.77	10.49	4.31	8.92

Table 4.1: *Multiple detection* - Averaged error figures when applying *IMSA* and *BARE* with noisy data.

The effectiveness of the approach has been numerically assessed showing a selected set of experiments dealing with single and multiple inclusions. A comparative analysis with the single resolution approach (*BARE*) has been carried out in order to underline the outperforming resolution accuracy provided by the *IMSA* multistep procedure.

The generalization capabilities of the learning-by-example methodology has been verified by testing the SVM-based classifier with noisy data as well as with measured data related to different breast characteristics respect to the training set.

It has to be noticed that three-dimensional reconstruction has been obtained starting from the measurement performed with fixed probe height. Usually, this configuration is typical for two-dimensional problem geometries since a 2D plane at the same source height is defined. As a matter of fact, the information enclosed in the measured scattering matrix is sufficient for the estimation of the pathology position in a 3D domain.

Chapter 5

Direction of Arrival Estimation

Dealing with the proposed LBE approach, this chapter presents an innovative multi-resolution approach for the real-time *DOA* estimation of multiple signals impinging on a planar array is presented. The method is based on a support vector classifier and it exploits a multi-scaling procedure to enhance the angular resolution of the detection process in the regions of incidence of the incoming waves. The data acquired from the array sensors are iteratively processed with a support vector machine (*SVM*) customized to the problem at hand. The final result is the definition of a map of the probability that a signal impinges on the antenna from a fixed angular direction. Selected numerical results, concerned with both single and multiple signals, are provided to assess potentialities and current limitations of the proposed approach.

5.1 Introduction

In the last decades, the technology of adaptive antenna arrays has been greatly advanced and applied to many mobile and wireless communication systems [61][62]. Within this framework, the antenna beam-forming plays an important role and the estimation of the directions of arrival (*DOAs*) of signals impinging on the array is a crucial task in order to enhance the spatial diversity and consequently the spectral efficiency. As a matter of fact, such an information enables the generation or steering of the radiation pattern with a maximum towards the desired signals and nulls along the directions of interfering signals [63][64]. The effects of interferences are mitigated and both the gain and the performance of the whole communication system are enhanced. For such reasons, the estimation of the *DOAs* of unknown interfering and desired signals is of great interest and it is still an open problem as confirmed by the number of papers published on this topic.

In the scientific literature, several methods have been proposed for the direction finding of multiple signals impinging on an array of narrow band sensors. Among them, the most widely known and used are *ESPRIT* (Estimation of Signal Parameters via Rotational Invariance Technique) [65]-[67] and *MUSIC* (Multiple Signal Classification) [68][69]. Other approaches based on the maximum likelihood (*ML*) *DOA* estimation have been proposed [70][71], as well.

In the last years, great attention has been also paid to the use of learning-by-examples (*LBE*) techniques. *LBE*-based approaches are able to provide a good trade-off between accuracy and convergence, which is mandatory for real time systems where fast reactions are required. Furthermore, they satisfactorily deal with unknown configurations (i.e., different from those “learned” during the training process) thanks to their generalization capability. Within this framework, the benefits of using radial basis function neural networks (*RBFNN*) have been carefully analyzed in [72]. As a matter of fact, neural networks (*NNs*) are suitable in approximating non-linear functions as those in *DOAs* estimation. Moreover, they can be easily implemented in analog circuits. An improved *RBFNN*-based approach has been presented by the same authors of [72] in [73] to address the problem of tracking an unknown number of multiple sources when no *a-priori* information on the number of impinging signals is available. More specifically, the region above the antenna has been partitioned into angular sectors and each sector “assigned” to a simpler *NN*, thus reducing with respect to [72] the problem complexity as well as the computational burden of the learning phase. Towards this end, each network has been trained to detect the subset of incoming signals that impinge on the corresponding angular sector. Accordingly, only those *NNs* of the regions where the signals have been detected in the first stage of the process are activated in the second one to estimate the *DOAs* of the incoming signals.

More recently, some techniques based on support vector machines (*SVMs*) [74]

have been analyzed to profitably exploit their solid mathematical foundation in statistical learning theory [6]. The main advantages of those approaches lie in their ability to deal with various and complex electromagnetic problems [75][38], and, analogously to *NNs*, in an easy hardware implementation [76]. As far as the *DOA* estimation is concerned, a support vector regression (*SVR*) procedure has been presented in [77] when dealing with linear arrays. In such a case, a *SVM* has been used to estimate the *DOA* of each impinging electromagnetic wave starting from a set of known input-output examples where the *DOAs* of the signals were uniformly distributed in the whole angular region above the receiver. Despite the generalization capability of the *SVR*-based method, an *a-priori* information on the number of sources and pre-fixed angular separations between the *DOAs* (as in [72]) have been considered to increase the reliability of the estimation procedure. An extension of such a model has been presented in [78] and experimentally validated in [79] successively.

In this paper, an innovative procedure for real-time direction finding of signals impinging on a planar array of electromagnetic sensors is presented. The problem of the *DOAs* estimation is formulated as a two step procedure, where the first step is aimed at determining the decision function that correctly classifies whatever input pattern by means of a *SVM*-based approach. In the second step, the output of the decision function is mapped into the *a-posteriori* probability that a signal impinges on the antenna from a fixed direction. In order to increase the accuracy of the estimation process and to reduce the computational burden affecting other *DOAs* procedures, the proposed two-step strategy is nested into an iterative multi-scaling process [80]. Accordingly, the resolution accuracy is improved only in those angular regions where the unknown sources are supposed to be located at the previous iteration. More specifically, the algorithm first determines a coarse probability map of the *DOAs* starting from a training set where the incoming signals are non-uniformly distributed along the elevation direction, θ , and the azimuthal one, ϕ . Then, the *SVM* is used to classify the input test dataset at successive resolution levels by performing a kind of synthetic zoom in the angular regions of interest (*ARoIs*) where a higher probability is detected and considering the same training set, thus performed only once and off-line. Concerning the antenna architecture and unlike [73] and [78], planar arrays of sensors are considered since linear arrays lack the ability to scan in 3*D*-space and the estimation of both the elevation θ and the azimuth ϕ angles is crucial and has many applications in various fields of engineering. For instance, a complete *DOA* information it is possible to improve the coverage of transmission in wireless communications by avoiding interferences and enhancing the system capacity [81]. More specifically, planar arrangements are very attractive in mobile communications with portable devices where the main beam must be scanned in any direction [82]. Moreover, the number of impinging signals is unknown as well as their directions belonging to the whole angular range above the planar antenna system (i.e., $\theta \in [0 : 90^\circ]$ and $\phi \in [0 : 360^\circ]$).

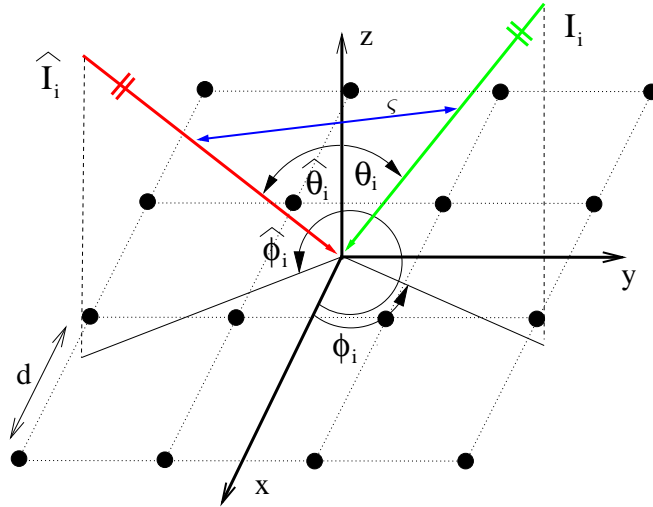


Figure 5.1: Planar array geometry.

The chapter is organized as follows. The formulation of the iterative two-step multi-resolution *DOA* approach (in the following denoted by the acronym *IMSA – SVM*) is described in Section 5.2. In order to show the innovative features of the approach and to assess its effectiveness, a selected set of numerical results concerned with both single and multiple signals is reported and discussed (Sect. 5.3). Moreover, some comparisons with state-of-the-art techniques are also reported. Finally, some conclusions are drawn in Sect. 5.4.

5.2 Mathematical Formulation

Let us consider a planar array of M isotropic elements displaced on a regular and rectangular grid with inter-element spacing d on the $x - y$ plane. A set of I electromagnetic waves impinge on the array from unknown angular directions (θ_i, ϕ_i) , $i = 1, \dots, I$, as sketched in Fig. 5.1. The signals, supposed to be narrow-band and centered at the carrier frequency f (λ being the corresponding free-space wavelength), are generated by a set of electromagnetic sources placed in the far-field of the receiving antenna. The open-circuit voltage at the output of the m -th sensor can be expressed as [78]

$$v_m = \sum_{i=1}^I \{a_m(\theta_i, \phi_i) [\underline{\mathbf{E}}_i(x_m, y_m) \cdot \underline{\mathbf{e}}_m]\} + g_m, \quad m = 1, \dots, M \quad (5.1)$$

where $a_m(\theta_i, \phi_i) = e^{j\frac{2\pi}{\lambda} \sin\theta_i(x_m \cos\phi_i + y_m \sin\phi_i)}$, (x_m, y_m) being the location of the m -th sensor expressed in wavelength, and g_m is the background random noise at the m -th locations. The noise samples are supposed to be statistically independent and characterized by a random Gaussian distribution with zero mean value.

Moreover, \underline{E}_i and \underline{e}_m are the electric field associated to the i -th impinging wave and the effective length of the m -th array element.

According to the guidelines described in [63] and [64] about the control of adaptive/smart antennas, the solution of the *DOAs* estimation problem is based also in this work on the measurement of the total correlation matrix, defined as

$$\underline{\Phi} = E \{ \underline{v} \cdot \underline{v}^* \} \quad (5.2)$$

where $\underline{v} = \{v_m; m = 1, \dots, M\}$ and the superscript $*$ stands for complex conjugation, at the output of the planar array since it contains sufficient information on the received signals [73].

From a statistical point of view, the problem at hand can be formulated as the definition of the probability map of the angular incidence of the incoming waves starting from the knowledge of the total correlation matrix $\underline{\Phi}$. Towards this end, let us partition the angular region above the array into a two-dimensional lattice of $H = H_\theta \times H_\phi$ cells, each one corresponding to an angular sector of sides $\Delta\theta$ and $\Delta\phi$ [Fig. 5.2(a)]. The status χ_h of each cell can be *empty* [$\chi_h = \chi(\theta_h, \phi_h) = -1$], if any signal impinges on the array from the angular region identified by the same cell, or *occupied* [$\chi_h = \chi(\theta_h, \phi_h) = 1$], otherwise. Accordingly, the original problem can be stated as follows: “*find the a-posteriori probability function $Q(\theta, \phi)$ given a measured value of the total correlation matrix $\underline{\Phi}$ at the receiver*”. Mathematically, $Q(\theta, \phi)$ can be also expressed as the linear combination of the non-overlapping basis functions $B_h(\theta, \phi)$, $h = 1, \dots, H$ defined over the angular lattice

$$Q(\theta, \phi) = \sum_{h=1}^H q(\theta_h, \phi_h) B_h(\theta, \phi) \quad (5.3)$$

where the weighting coefficient $q(\theta_h, \phi_h)$ is the probability value that a wave impinges on the array from the h -th angular sector [i.e., $q(\theta_h, \phi_h) = Pr \{ \chi_h = 1; \underline{\Phi} \}$] and $B_h(\theta, \phi) = 1$ if (θ, ϕ) belongs to the h -th cell and $B_h(\theta, \phi) = 0$ otherwise.

In order to improve the achievable angular resolution, a multi-resolution representation of the unknown function $Q(\theta, \phi)$ is looked for [Fig. 5.2(b) - $r = 1$] by exploiting an iterative process analogously to [80]. More specifically, the probability function is expressed at the s -th step of the iterative procedure as a twofold summation of shifted and dilated spatial basis functions

$$Q^{(s)}(\theta, \phi) = \sum_{r=0}^{R(s)} \sum_{h(r)=1}^{H(r)} q^{(s)}(\theta_{h(r)}, \phi_{h(r)}) B_{h(r)}(\theta, \phi); s = 1, \dots, S_{opt} \quad (5.4)$$

r being the resolution index and $R(s) = s - 1$. The summation over r ranges from 0 [Fig. 5.2(a)], which corresponds to the largest characteristic length scale, to $R(s)$ [Fig. 5.2(b)], which corresponds to the smallest angular basis-function support at the s -th scaling step. For a given value of r , $H(r) = H_\theta^{(r)} \times H_\phi^{(r)}$ is the number of non-overlapped basis functions centered in the angular sub-domain represented at the r -th resolution. Accordingly, the iterative *DOA* detection

5.2. MATHEMATICAL FORMULATION

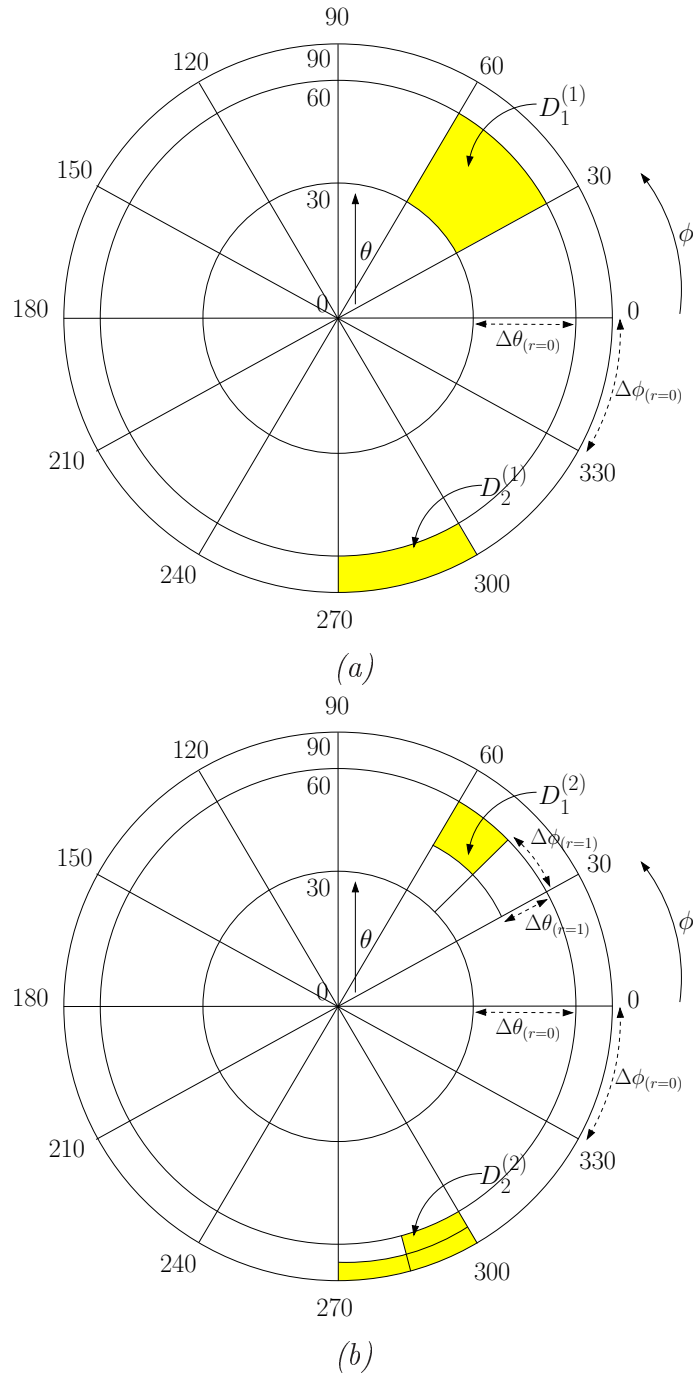


Figure 5.2: *IMSA – DOA Procedure* - Angular region partitioning and *ARoIs* identification at the steps $s = 1$ (a) and $s = 2$ (b).

procedure is aimed at locating the terms of small length scale at those *ARoIs* [e.g., the yellow cells in Figs. 2(a)-2(b)] where the signals are supposed to impinge with higher probability.

In order to profitably exploit the multiresolution representation of the *a-posteriori* probability function (5.4) and solving the arising *DOA* problem, the following multistep classification process is performed by means of a *SVM*-based technique. More in detail,

- **Step 0 - SVM Training Phase.** The *SVM* is trained once and off-line starting from the knowledge of a set of known examples (i.e, input/output relationships)

$$\left\{ \left[\underline{\Phi}, (\theta_n, \phi_n), \chi_n = \chi(\theta_n, \phi_n); n = 1, \dots, N \right]^{(t)} ; t = 1, \dots, T \right\} \quad (5.5)$$

called *training set*, where T is the number of training data. The N samples of each training data are composed by $I(t)$ examples concerned with angular positions (θ_i, ϕ_i) , $i = 1, \dots, I(t)$, $I(t) \leq I_{max}$ where a signal impinges on the array [i.e., *occupied* directions - $\chi(\theta_i, \phi_i) = 1$; $i = 1, \dots, I(t)$], while the remaining $F(t) = N - I(t)$ are related to *empty* directions [i.e., $\chi(\theta_f, \phi_f) = -1$; $f = 1, \dots, F(t)$].

Starting from the knowledge of the *training set*, the problem turns out to be the definition of a suitable discriminant function $\hat{\mathfrak{S}}$

$$\hat{\mathfrak{S}} : \underline{\Phi} \rightarrow [\chi(\theta_h, \phi_h); h = 1, \dots, H] \quad (5.6)$$

that separates the two classes $\chi(\theta, \phi) = 1$ and $\chi(\theta, \phi) = -1$ on the basis of the total correlation matrix $\underline{\Phi}$ measured at the output of the planar array. In order to approach the problem with a single classifier, the problem at hand is reformulated as that of building the following single output function

$$\hat{\mathfrak{S}} : \left[\underline{\Phi}, (\theta_n, \phi_n); n = 1, \dots, N \right] \rightarrow \chi(\theta_h, \phi_h), \quad h = 1, \dots, H. \quad (5.7)$$

Towards this purpose and according to the *SVM* theory [6], the following linear decision function is adopted

$$\hat{\mathfrak{S}} \left\{ \underline{\varphi}(\underline{\Phi}, (\theta_n, \phi_n)) \right\} = \underline{w} \cdot \underline{\varphi}(\underline{\Phi}, (\theta_n, \phi_n)) + b, \quad n = 1, \dots, N. \quad (5.8)$$

$\hat{\mathfrak{S}}$ is determined in a space (called “*feature space*”) with a higher dimensionality than the original input data space and obtained through the non-linear operator $\underline{\varphi}(\cdot)$ [6]. The unknown terms \underline{w} and b , which unequivocally define the decision hyperplane $\hat{\mathfrak{S}}$, are the normal vector and a bias, respectively. They are computed during the *Training Phase* according to the guidelines described in [38];

5.2. MATHEMATICAL FORMULATION

- **Step 1 - Low-Order DOA Estimation** ($s = 1$). At the first step, a coarse probability map [Eq. (5.4) - $s = 1$] is determined by means of the SVM classifier mapping the decision function $\hat{\mathfrak{S}}$ into the *a-posteriori* probability function.

The unknown probability coefficients $q^{(s)}(\theta_h, \phi_h) \Big|_{s=1}$, $h = 1, \dots, H$ are approximated with a sigmoid function [6] as follows

$$q^{(s)}(\theta_h, \phi_h) = \frac{1}{1 + \exp \left[\gamma \hat{\mathfrak{S}} \left\{ \underline{\varphi}(\underline{\Phi}, (\theta_h, \phi_h)) \right\} + \nu \right]} \quad (5.9)$$

where γ and ν are two parameters computed according to a fitting process [38] starting from a subset of the T training data of the *Training Set*;

- **Step 2 - IMSA – SVM Process** ($s \geq 1$).
 - **Step 2.a - Angular Regions of Interest (ARoIs) Identification** ($s \leftarrow s + 1$). Starting from the probability map previously (i.e., at the $s - 1$ -th iteration) determined, such a step is aimed at identifying the angular sectors $D_\ell^{(s)}$, $\ell = 1, \dots, L(s)$ where the signals are supposed to impinge in order to improve the resolution only in those regions and enhance the accuracy of the DOA estimation. Towards this end, first the values of the function $Q^{(s-1)}(\theta, \phi)$ are scaled, thus defining the following new set of normalized probability coefficients

$$p^{(s-1)}(\theta_{h(r)}, \phi_{h(r)}) = \frac{q^{(s-1)}(\theta_{h(r)}, \phi_{h(r)})}{q_M - q_m} + \frac{q_m}{q_m - q_M}, \quad \begin{matrix} h(r) = 1, \dots, H(r) \\ r = 0, \dots, R(s) \end{matrix} \quad (5.10)$$

where $q_M = \max_{r=0, \dots, R(s)} \left\{ \max_{h(r)=1, \dots, H(r)} \left[q^{(s-1)}(\theta_{h(r)}, \phi_{h(r)}) \right] \right\}$ and $q_m = \min_{r=0, \dots, R(s)} \left\{ \min_{h(r)=1, \dots, H(r)} \left[q^{(s-1)}(\theta_{h(r)}, \phi_{h(r)}) \right] \right\}$. Successively, the new probability function

$$P^{(s-1)}(\theta, \phi) = \sum_{r=0}^{R(s-1)} \sum_{h(r)=1}^{H(r)} p^{(s-1)}(\theta_{h(r)}, \phi_{h(r)}) B_{h(r)}(\theta, \phi)$$

is thresholded by nulling the scaled coefficients greater than a user-defined threshold η . Finally, the thresholded function

$$P_{th}^{(s-1)}(\theta, \phi) = \sum_{r=0}^{R(s-1)} \sum_{h(r)=1}^{H(r)} p_{th}(\theta_{h(r)}, \phi_{h(r)}) B_{h(r)}(\theta, \phi) \quad (5.11)$$

where $p_{th}(\theta_{h(r)}, \phi_{h(r)}) = p^{(s-1)}(\theta_{h(r)}, \phi_{h(r)})$ if $p^{(s-1)}(\theta_{h(r)}, \phi_{h(r)}) > \eta$ and $p_{th}(\theta_{h(r)}, \phi_{h(r)}) = 0$ otherwise, allows one to identify the ARoIs, $D_\ell^{(s)}$, $\ell = 1, \dots, L(s)$ defined as those angular sub-domains where $P_{th}^{(s-1)}(\theta, \phi) \neq 0$;

- **Step 2.b** - *Multiresolution DOA Estimation*. A synthetic zoom is performed by refining the representation of the unknown function $Q^{(s)}(\theta, \phi)$ and increasing the angular resolution ($r \leftarrow r + 1$) only in the *ARoIs* identified at (*Step 2.a*). Therefore, the multiresolution *a-posteriori* probability function (5.4) is updated⁽¹⁾ by setting $Q^{(s)}(\theta, \phi) = P_{th}^{(s-1)}(\theta, \phi)$ and computing the new highest resolution coefficients, $q^{(s)}(\theta_{h(r)}, \phi_{h(r)})$, when $(\theta, \phi) \in D_\ell^{(s)}$, $\ell = 1, \dots, L(s)$ as in (5.9);
- **Step 3** - *Termination Criterion* ($s = S_{opt}$). The sequence of operations of *Step 2* is repeated until both the dimensions and the number of *ARoIs* between two consecutive cycles are stationary [i.e., $L(s) = L(s-1)$] and the variations of the dimensions of the *ARoIs* are not greater than the highest angular resolution at the s -th step, $\Delta_{min}^{(s)} = \min \left\{ \Delta\theta_{R(s)}^{(s)}, \Delta\phi_{R(s)}^{(s)} \right\}$.

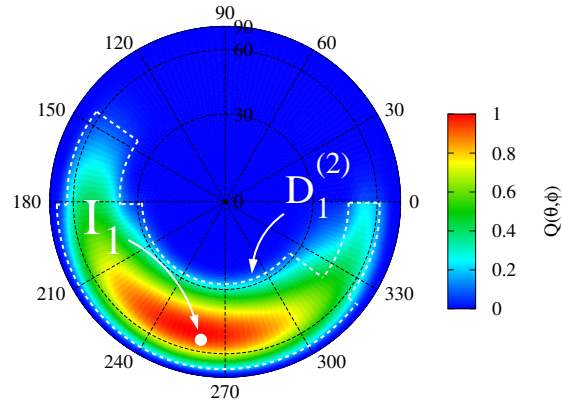
5.3 Numerical Simulations and Results

In order to assess the effectiveness and reliability of the proposed approach, an exhaustive set of numerical experiments has been performed and some selected results will be reported in the following for illustrative purposes. The remaining of this section will firstly (Sect. 5.3.1) illustrate the behavior of the multi-scaling procedure also in comparison with other state-of-the-art approaches for *DOA* estimation. The second part (Sect. 5.3.2) will be devoted to analyze the potentialities and current limitations of the *IMSA – SVM* approach when dealing with various and challenging electromagnetic scenarios. In such a framework, some configurations in which conventional state-of-the-art signal subspace-based array processing techniques cannot be applied are also dealt with in order to point out the enhanced range of applicability of *SVM* approaches. Finally, a uniform array of $\frac{\lambda}{2}$ -dipoles is considered (Sect. 5.3.3) to verify the suitability and reliability of the proposed method in correspondence with a realistic array modelling.

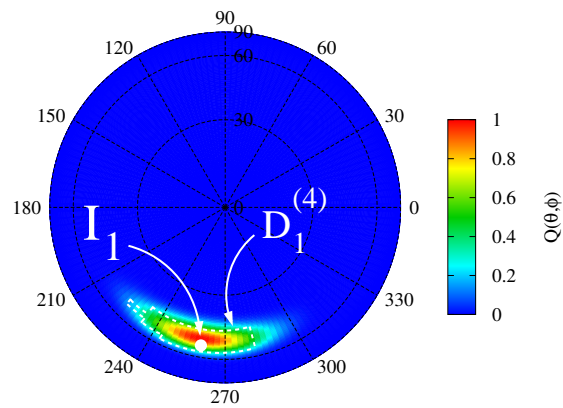
With reference to the geometry shown in Fig. 5.1, a square planar array of $M = 16$ isotropic radiators spaced by $d = \frac{\lambda}{2}$ is considered. The power of the impinging signals has been set to $P_i = 30 \text{ dB}$, $i = 1, \dots, I$ above the level of the background noise.

Concerning the training set, the following setup $T = 400$ and $I_{max} = 4$ has been assumed and the *SVM* classifier has been trained once and off-line on the same data set whatever the test experiment. As regards to the $T = \sum_{i=1}^{I_{max}} T_i$ training examples, different scenarios have been considered, $T_i = 100$ being the number

¹ (1) It is worth noting that at the s -th step of the multi-scaling procedure only the angular ranges belonging to the *ARoIs* are processed by the *SVM* classifier with a non-negligible saving of computational resources.



(a)



(b)

Figure 5.3: *Single signal scenario, $I = 1$* - Probability map determined by the *IMSA – DOA* procedure at: (a) $s = 2$, (b) $s = S_{opt} = 4$.

of configurations with i signals. Moreover, the actual *DOAs* of the signals of the training data have been randomly chosen in a discrete grid of locations (θ_n, ϕ_n) , $n = 1, \dots, N$ belonging to the the angular region above the antenna

$$\begin{cases} \theta_n = \theta_0 + \left\lfloor \frac{n-1}{\sqrt{N}} \right\rfloor \Delta\theta \\ \phi_n = \phi_0 + \left\lceil \frac{n-1}{\sqrt{N}} \right\rceil \Delta\phi \end{cases}, \quad n = 1, \dots, N \quad (5.12)$$

$\lfloor \cdot \rfloor$ and $\lceil \cdot \rceil$ being the floor function and the ceiling function, respectively. Moreover, in order to fully assess the generalization properties of the *SVM*-based approach, the *DOAs* of the test examples are different from those of the training dataset.

5.3.1 Single Signal Scenario - Comparative Assessment

The first experiment deals with the *DoA* detection of a single signal and a *test set* of $T_1^{(test)} = 100$ examples related to the single-signal scenario has been considered. An illustrative description of the behavior of the proposed *IMSA – SVM* approach is shown in Fig. 5.3 dealing with the “representative” (of the method performance on the whole test dataset) configuration of a signal coming from $(\theta_1 = 53^\circ, \phi_1 = 260^\circ)$. At the first step ($s = 1$), the planar angular region $D^{(1)}$ is partitioned into $H^{(s)} = 81$ cells (being $\Delta\theta_{(r)}^{(s)} = 10^\circ$ and $\Delta\phi_{(r)}^{(s)} = 40^\circ$, $r = 0$, the angular steps along the elevation direction, θ , and the azimuthal one, ϕ , respectively) and a coarse *DOA* probability map is determined following the procedure described in Sect. ?? (*Step 1*). Then, the multi-scaling procedure takes place ($s \geq 2$). The *ARoIs* are identified and partitioned into $H_{R^{(s)}}^{(2)} \Big|_{R^{(s)}=s-1} = 81$ cells with an angular resolution of $\Delta\theta_{(1)}^{(2)} = 5^\circ$ and $\Delta\phi_{(1)}^{(2)} = 20^\circ$. For the sake of space, only the *DOA* probability map obtained at the end of the second step ($s = 2$) is shown in Fig. 5.3(a). The procedure is then iterated until $s = S_{opt} = 4$ [$R(S_{opt}) = 3$] with the final result reported in Fig. 5.3(b) characterized by an angular resolution in $D_1^{(4)}$ equal to $\Delta\theta_{(3)}^{(4)} = 1.25^\circ$ and $\Delta\phi_{(3)}^{(4)} = 5^\circ$. As it can be observed (Fig. 5.3), the region with higher probability of incidence turns out to be closer and closer to the actual angular location of the signal when increasing the step number. Quantitatively such an event can be analytically quantified by computing the values of the *location index* $\varsigma^{(s)}$ (Fig. 5.2) and of the *incidence area* $\psi^{(s)}$ defined as follows

$$\varsigma^{(s)} = \frac{\Phi^{(s)}}{\max\{\Phi^{(s)}\}} \times 100 \quad (5.13)$$

where

$$\Phi^{(s)} \triangleq \sqrt{\left(\sin\theta\cos\phi - \sin\hat{\theta}^{(s)}\cos\hat{\phi}^{(s)}\right)^2 + \left(\sin\theta\sin\phi - \sin\hat{\theta}^{(s)}\sin\hat{\phi}^{(s)}\right)^2 + \left(\cos\theta - \cos\hat{\theta}^{(s)}\right)^2}$$

and

$$\psi^{(s)} = \pi \left\{ \frac{\sum_{r=0}^{R(s)} \sum_{h(r)=1}^{H(r)} \left\{ \frac{\zeta_{h(r)}^{(s)} q^{(s)}(\theta_{h(r)}, \phi_{h(r)})}{\max_{h(r)} \{q^{(s)}(\theta_{h(r)}, \phi_{h(r)})\}} \right\}}{\sum_{r=0}^{R(s)} \sum_{h(r)=1}^{H(r)} \left\{ \frac{q^{(s)}(\theta_{h(r)}, \phi_{h(r)})}{\max_{h(r)} \{q^{(s)}(\theta_{h(r)}, \phi_{h(r)})\}} \right\}} \right\}^2 \quad (5.14)$$

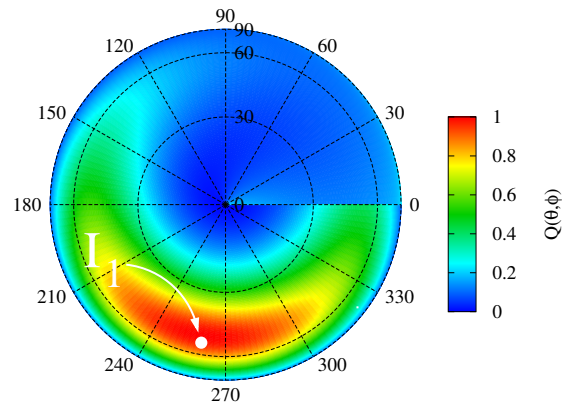
being $\zeta_{h(r)}^{(s)} = \left[\left(\sin \theta_{h(r)} \cos \phi_{h(r)} - \sin \hat{\theta}^{(s)} \cos \hat{\phi}^{(s)} \right)^2 + \left(\sin \theta_{h(r)} \sin \phi_{h(r)} - \sin \hat{\theta}^{(s)} \sin \hat{\phi}^{(s)} \right)^2 + \left(\cos \theta_{h(r)} - \cos \hat{\theta}^{(s)} \right)^2 \right]^{\frac{1}{2}}$, (θ, ϕ) are the actual coordinates of the signal incidence point, whereas $(\hat{\theta}, \hat{\phi})$

$$\begin{aligned} \hat{\theta}^{(s)} &= \frac{\sum_{r=0}^{R(s)} \sum_{h(r)=1}^{H(r)} \{ \theta_{h(r)} q^{(s)}(\theta_{h(r)}, \phi_{h(r)}) \}}{\sum_{r=0}^{R(s)} \sum_{h(r)=1}^{H(r)} \{ q^{(s)}(\theta_{h(r)}, \phi_{h(r)}) \}} \hat{\phi}^{(s)} = \\ &= \frac{\sum_{r=0}^{R(s)} \sum_{h(r)=1}^{H(r)} \{ \phi_{h(r)} q^{(s)}(\theta_{h(r)}, \phi_{h(r)}) \}}{\sum_{r=0}^{R(s)} \sum_{h(r)=1}^{H(r)} \{ q^{(s)}(\theta_{h(r)}, \phi_{h(r)}) \}} \end{aligned} \quad (5.15)$$

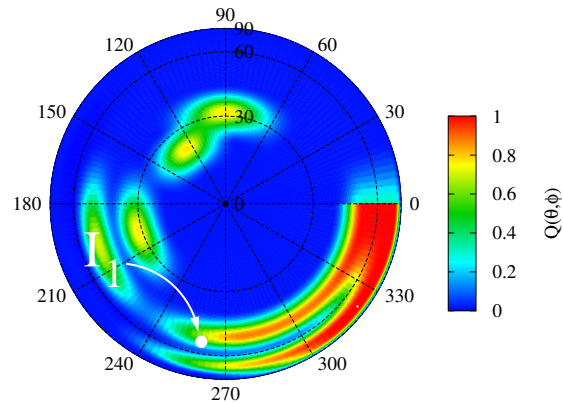
identify the center of the ℓ -th *ARoI* where the signal/signals is/are supposed to impinge. As a matter of fact, the value of the location index reduces from $\zeta^{(1)} = 13.17$ down to $\zeta^{(S_{opt})} = 2.53$ (being $\zeta^{(2)} = 4.10$ and $\zeta^{(3)} = 2.87$). Analogously, $\psi^{(1)} = 2.74$, $\psi^{(2)} = 0.94$, $\psi^{(3)} = 0.36$, until $\psi^{(S_{opt})} = 0.14$. As regards to the whole set of test examples, the statistics of the ‘‘convergence’’ values of the indexes (5.13) and (5.14) are given in the first block of Tab. 5.2.

In order to get an insight into the advantages of the proposed multi-resolution approach over the classification single-step techniques, a bare *DOA SVM*-based method has been considered and applied to the same test example. To fairly compare the two methods, the same training dataset has been used. Moreover, the same angular resolution has been adopted in both cases. Towards this purpose, an angular lattice characterized by a uniform grid whose cell side was equal to the finest discretization of the multi-resolution procedure (i.e., $\Delta\theta = \Delta\theta_{(3)}^{(4)}$ and $\Delta\phi = \Delta\phi_{(3)}^{(4)}$), has been defined over the whole angular investigation domain of the single step *SVM* approach. As it can be observed [Fig. 5.4(a)], although the value of ζ is quite close to that of the *IMSA* strategy (i.e., $\zeta]_{IMSA-SVM} = 2.53$ vs. $\zeta]_{SVM} = 3.14$), the extension of the incidence area turns out to be significantly wider ($\psi]_{IMSA-SVM} = 0.14$ vs. $\psi]_{SVM} = 2.79$). On the other hand, it cannot be neglected that the *CPU*-time of the test phase of the bare procedure is approximately fifty times the one of the *IMSA-SVM* because of the need to obtain a detailed map in the whole investigation area $D_1^{(1)}$ instead of in a limited *ARoI*, $D_1^{(S_{opt})}$, only. As a matter of fact, the number of test points used by the *IMSA* approach turns out to be widely reduced.

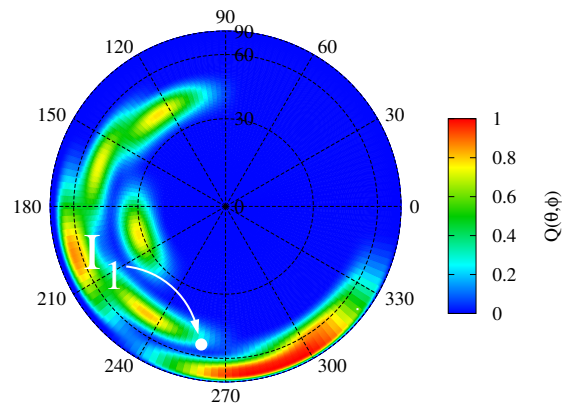
For completeness, the results from other standard nonlinear classification methods, such as the multilayer perceptron (*MLP*) and the radial basis functions (*RBF*) neural network, have been analyzed, as well. More specifically, the *DOA*



(a)



(b)



(c)

Figure 5.4: *Single signal scenario, $I = 1$* - Probability maps obtained with different classification approaches: (a) single-step *SVM*, (b) multi layer perceptron (*MLP*) neural network, and (c) radial basis function (*RBF*) neural network [$\Delta\theta = 1.25^\circ$ and $\Delta\phi = 5^\circ$].

	<i>Min</i>	<i>Max</i>	<i>Avg</i>	<i>Var</i>
<i>Single Signal (I = 1)</i>				
$\hat{\varsigma}$	0.16	43.25	2.81	8.76
$\hat{\psi}$	0.02	9.14	0.25	1.35
<i>Multiple Signals (I = 2)</i>				
$\hat{\varsigma}$	0.31	58.47	4.51	8.56
$\hat{\psi}$	0.007	11.05	0.28	1.54
<i>Multiple Signals (I = 3)</i>				
$\hat{\varsigma}$	0.38	17.35	5.55	2.14
$\hat{\psi}$	0.009	0.37	0.15	0.34
<i>Multiple Signals (I = 4)</i>				
$\hat{\varsigma}$	0.47	70.72	17.29	13.58
$\hat{\psi}$	0.005	1.89	0.17	0.69

Table 5.1: Statistics of the averaged performance indexes ($\hat{\varsigma} = \sum_{i=1}^I \varsigma^{(i)}$ and $\hat{\psi} = \sum_{i=1}^I \psi^{(i)}$) for different signal configurations ($I = 1, 2, 3, 4$).

probability maps obtained with the *MLP*-based and *RBFNN*-based classifiers are reported in Figs. 5.4(b) and 5.4(c), respectively. Whatever the method, the achieved estimate does not appear to be adequate and certainly not comparable neither with that of the *IMSA – SVM* [Figs. 5.4(b)-5.4(c) vs. Fig. 5.3(b)] nor with that of the bare *SVM* [Figs. 5.4(b)-5.4(c) vs. Fig. 5.4(a)] as also confirmed by the values of the location index: $\varsigma]_{RBF} = 10.21$ and $\varsigma]_{MLP} = 25.91$.

The last analysis is concerned with the comparison between the *IMSA – SVM* and those state-of-the-art methods for *DOA* estimation aimed at determining the angular incidence of the signals, namely *MUSIC*, *ESPRIT* (i.e., two one-dimensional *ESPRIT*s independently-applied to the arrays followed by an alignment procedure to associate the estimated azimuth and elevation angle), *2D-unitary ESPRIT* [67], and a support vector regression-based (*SVR*) approach. Towards this end, the azimuthal direction of the actual signal has been fixed to $\phi = 260^\circ$, while the elevation angle has been varied in the range $\theta \in [20^\circ \div 80^\circ]$. Moreover, the *SVR* algorithm has been previously trained with a dataset composed by $T = T_1 = 100$ examples concerned with only one signal ($I = 1$). The methods are then compared by means of the resulting signal location error, ς .

Because of the planar array of isotropic elements and as expected [83], the performances of the *DOA* techniques in θ elevation-estimation turn out to be better at high elevations ($\theta \rightarrow 0^\circ$) [Tab. II], while the ϕ azimuth-estimation is greatest at low elevations ($\theta \rightarrow 90^\circ$). Moreover, the values of the estimation indexes point out that the *IMSA – SVM* (last column - Tab. 4.1) is able to obtain similar

	<i>DOA Method</i>					
θ_1	<i>ESPRIT</i>	<i>2DESCRIT</i>	<i>MUSIC</i>	<i>SVR</i>	<i>IMSA – SVM^(unif)</i>	<i>IMSA – SVM</i>
20°	0.16	0.08	0.34	1.21	0.75	0.52
40°	0.51	0.22	0.59	1.38	1.17	0.83
60°	0.51	0.27	0.68	1.64	1.52	2.22
80°	0.68	0.36	0.74	1.56	1.64	4.93

Table 5.2: *Single signal scenario, $I = 1$ - Comparative assessment. Values of the location index ς when applying *IMSA – DOA*, *SVR*, *MUSIC*, and *ESPRIT*.*

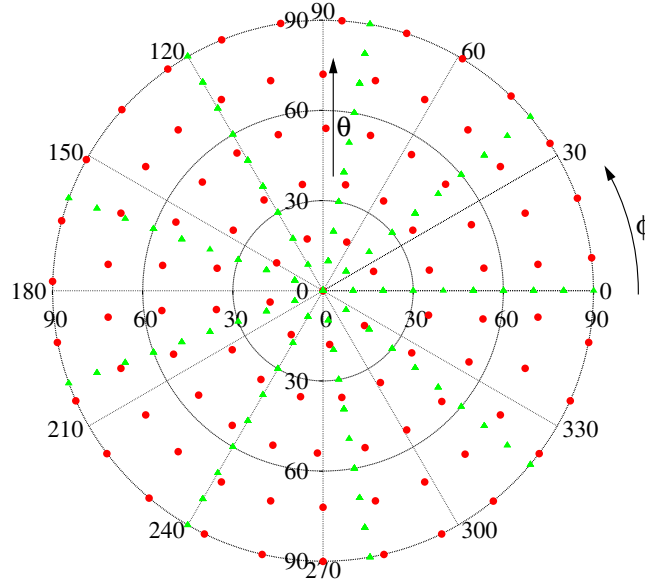


Figure 5.5: *Single signal scenario*, $I = 1$ - Uniform (red points) and non-uniform (green triangles) angular training sets.

results, in terms of angular resolution, than those provided by the *SVR* and of the same order in magnitude of *MUSIC* and *ESPRIT*s except for wider angles ($\theta \geq 60^\circ$), even though these latter need more *CPU*-time (i.e., an optimized *IMSA – SVM* implementation just needs few milliseconds on a *PC* equipped with a 3.0 GHz processor and 2 GHz of *RAM*). As regards to the growing of the location index around 60° , its mainly depends on the training set. As a matter of fact, it can be avoided by modifying the off-line training phase. For instance, the choice of a uniform angular distribution of the training samples (Fig. 5.5), instead of a non-uniform arrangement, allows one to obtain a behavior of ζ almost invariant to θ for medium-high elevations.

In order to point out the generalization capabilities of the proposed approach as well as its robustness to the model tolerances [74][84], the effect of the array failure has been evaluated and the arising results compared to those with *2D-unitary ESPRIT* which demonstrated several advantages over *MUSIC* and the standard *ESPRIT* implementation. Towards this end, an increasing number of array elements has been switched off. Moreover, the *a-priori* information on the failure of some array elements has not been exploited through the definition of an ad-hoc training set, but the same non-uniform set of input-output examples concerned with the unperturbed array structure has been used. The results of the comparative assessment when $(\theta_1 = 53^\circ, \phi_1 = 260^\circ)$ are reported in Fig. 5.6.

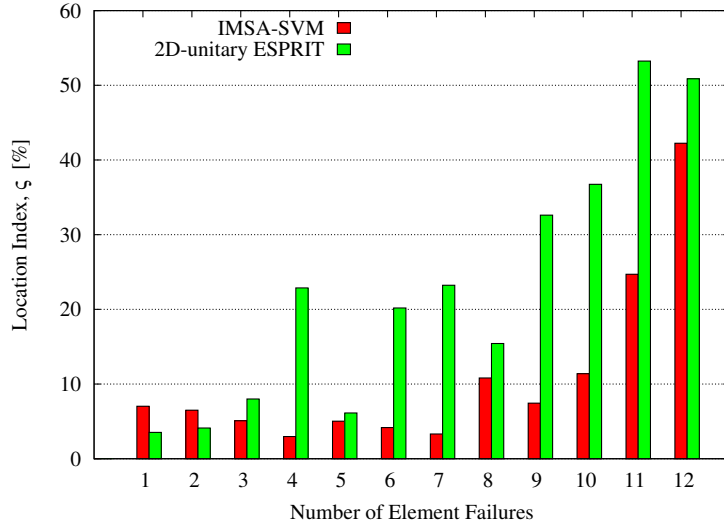


Figure 5.6: *Single signal scenario*, $I = 1$ - Behavior of the location index versus the number of failed array elements.

5.3.2 Complex Scenarios - Performance Analysis

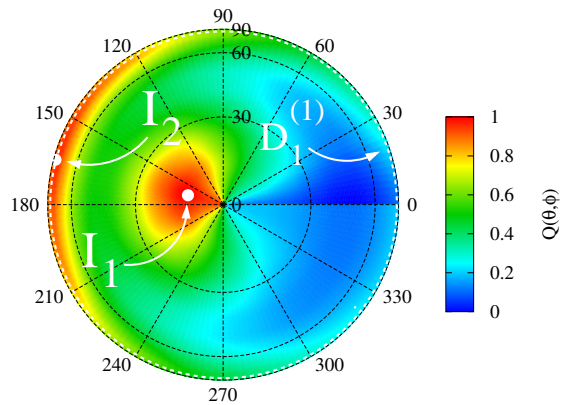
The following experiments are aimed at assessing the effectiveness of the *IMSA-SVM* in detecting the *DOAs* of multiple signals.

Dealing with the detection of two different incidence points, the first example is concerned with test signals coming from $(\theta_1 = 12^\circ, \phi_1 = 165^\circ)$ and $(\theta_2 = 82^\circ, \phi_2 = 165^\circ)$, respectively. The probability maps estimated by the *IMSA-SVM* at different steps are shown in Fig. 7 together with those obtained with the single-step *SVM* classification procedure [Fig. 5.8(d)], the *MLP*-based approach [Fig. 5.8(e)], and the *RBF* technique [Fig. 5.8(f)]. As expected and confirming the outcomes from the study of the single-signal detection, the multi-scaling process allows one to significantly enhance the performances of the single-step classification approaches as pictorially shown in Fig. 5.7 and quantitatively confirmed by the indexes in Tab. 5.3. Moreover, it is worth noting that this conclusion is not limited to a particular configuration of incidence angles, but it holds true whatever the two-signals scenario under test.

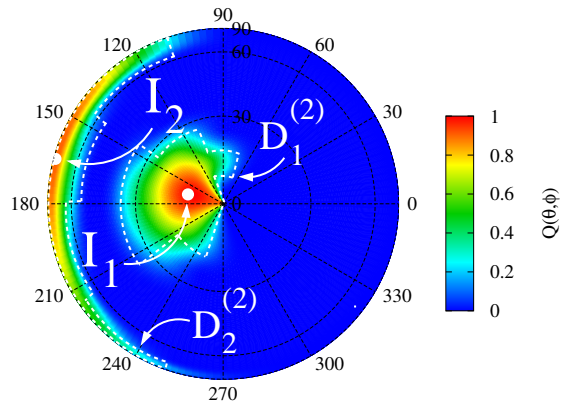
In order to assess the stability of the proposed approach, a test set composed by $T_2^{(test)} = 100$ examples has been considered. The results obtained with the *IMSA-SVM* are summarized in Tab. 5.1 (second block). As expected, the mean values of the averaged performance indexes ($\hat{\zeta}_I \triangleq \sum_{i=1}^I \zeta^{(i)}$ and $\hat{\psi}_I \triangleq \sum_{i=1}^I \psi^{(i)}$) turn out to be very close to those of the previous test example [i.e., $avg(\hat{\zeta}_2) = 4.51$, $avg(\hat{\psi}_2) = 0.28$ versus $\zeta_1^{(S_{opt})} = 4.55$, $\psi_1^{(S_{opt})} = 0.23$ and $\zeta_2^{(S_{opt})} = 3.90$, $\psi_2^{(S_{opt})} = 0.25$].

The second numerical experiment, concerned with multiple incidences, considers

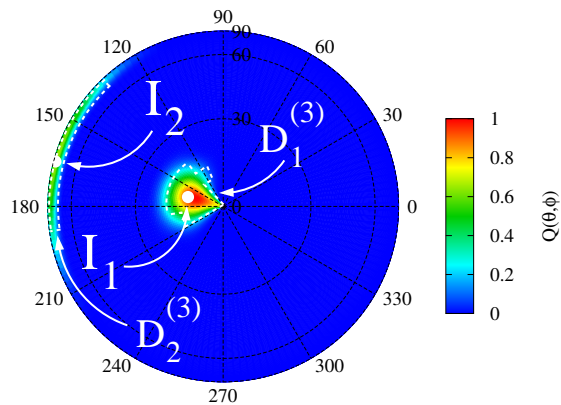
5.3. NUMERICAL SIMULATIONS AND RESULTS



(a)

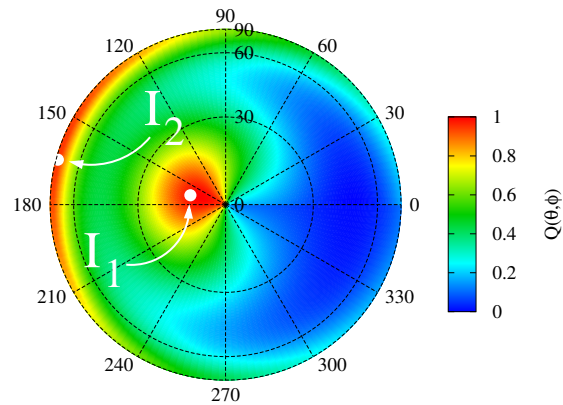


(b)

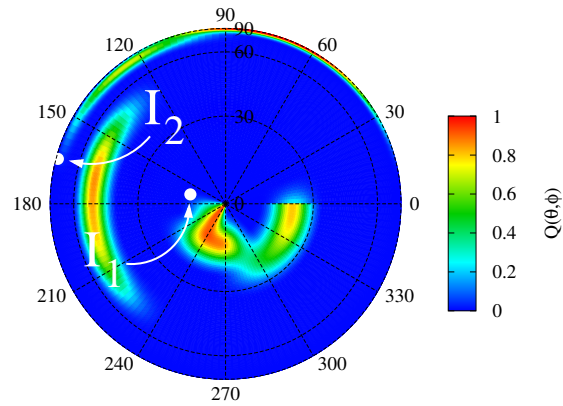


(c)

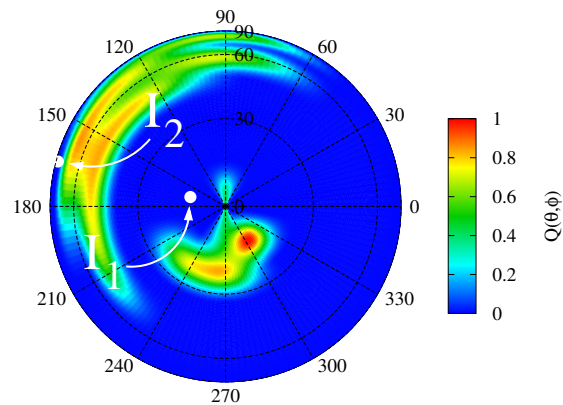
Figure 5.7: *Multiple signals scenario, $I = 2$* - Probability maps obtained with different classification approaches: *IMSA - SVM* [(a) $s = 1$, (b) $s = 2$, (c) $s = S_{opt} = 3$], $[\Delta\theta = \Delta\theta_{(2)}^{(3)} = 2.5^\circ$ and $\Delta\phi = \Delta\phi_{(2)}^{(3)} = 10^\circ$].



(d)



(e)



(f)

Figure 5.8: Multiple signals scenario, $I = 2$ - (d) single-step SVM, (e) multi layer perceptron (MLP) neural network, and (f) radial basis function (RBF) neural network [$\Delta\theta = \Delta\theta_{(2)}^{(3)} = 2.5^\circ$ and $\Delta\phi = \Delta\phi_{(2)}^{(3)} = 10^\circ$].

5.3. NUMERICAL SIMULATIONS AND RESULTS

<i>Method</i>	<i>DOA Indexes</i>			
	ς_1	ψ_1	ς_2	ψ_2
<i>IMSA – SVM</i>				
$s = 1$	8.91	2.33	10.27	3.08
$s = 2$	5.90	0.54	8.46	0.82
$s = S_{opt} = 3$	4.55	0.23	3.90	0.25
<i>Bare SVM</i>	6.04	0.67	16.78	3.78
<i>MLP</i>	17.54	0.27	30.53	2.21
<i>RBF</i>	17.19	0.28	27.77	0.99

Table 5.3: *Multiple signals scenario*, $I = 2$. Performance indexes when applying *IMSA–DOA*, single-step *SVM*, multi layer perceptron (*MLP*) neural network, and radial basis function (*RBF*) neural network.

three-signals configurations. As regards to the results for a test set of $T_3^{(test)} = 50$ three-signals examples, the values in the third block of Tab. 5.1 indicate that the resolution accuracy of the proposed approach does not significantly reduce with respect to the single-signal or two-signals scenarios [$avg(\hat{\varsigma}_3) = 5.55$, $avg(\hat{\psi}_3) = 0.15$ vs. $avg(\hat{\varsigma}_2) = 4.51$, $avg(\hat{\psi}_2) = 0.28$ and $\hat{\varsigma}_1 = 2.81$, $\hat{\psi}_1 = 0.25$]. As an illustrative example, let us consider the case of a set of signals impinging on the array from $(\theta_1 = 8^\circ, \phi_1 = 85^\circ)$, $(\theta_2 = 68^\circ, \phi_2 = 95^\circ)$, $(\theta_3 = 55^\circ, \phi_3 = 290^\circ)$. Starting from the coarse map determined, three different *ARoIs* are successively identified [Fig. 5.9(a)] and better resolved thus iteratively improving the *DOA* resolution accuracy as pointed out by the indexes in Tab. 5.4 where the values estimated by the other classification approaches are reported [Fig. 5.9(b)], as well. By comparing the distribution at the S_{opt} -th step of the *IMSA* and the one from the bare *SVM*, it is evident the improvement guaranteed by the multi-scaling process both in resolving and properly locating a number of *ARoIs* equal to the number of signals (I).

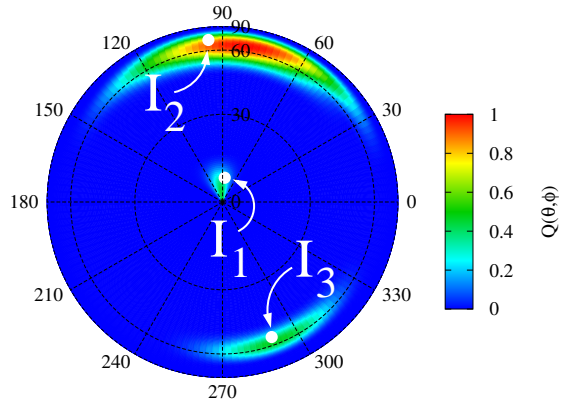
In the third experiment, $I = 4$ ($I = I_{max}$) signals impinge on the planar array. Figure 5.10 shows the results provided by the *IMSA – SVM* and in correspondence with a set of representative examples. More in detail, the first example (*Configuration 1/1/1/1*) refers to a configuration where four separated signals can be recognized [$(\theta_1 = 35^\circ, \phi_1 = 35^\circ)$, $(\theta_2 = 20^\circ, \phi_2 = 115^\circ)$, $(\theta_3 = 70^\circ, \phi_3 = 135^\circ)$, $(\theta_4 = 80^\circ, \phi_4 = 260^\circ)$ - Figs. 5.10(a)-5.10(c)]. The second example [Fig. 5.11(d)] deals with a two-clusters setup [*Configuration 2/2* - $(\theta_1 = 15^\circ, \phi_1 = 75^\circ)$, $(\theta_2 = 25^\circ, \phi_2 = 120^\circ)$, $(\theta_3 = 75^\circ, \phi_3 = 270^\circ)$, $(\theta_4 = 65^\circ, \phi_4 = 300^\circ)$], while a single signal and a cluster of three-signals are present in the last example [*Configuration 1/3* - $(\theta_1 = 15^\circ, \phi_1 = 105^\circ)$, $(\theta_2 = 80^\circ, \phi_2 = 275^\circ)$, $(\theta_3 = 85^\circ, \phi_3 = 300^\circ)$, $(\theta_4 = 75^\circ, \phi_4 = 315^\circ)$]. Whatever the example, the multi-scaling process is able to identify with an ever increasing resolution from $s = 1$ [Fig. 5.10(a)] up to $s = S_{opt} = 3$ [Fig. 5.10(c)] the *ARoIs*

<i>Method</i>	<i>DOA Indexes</i>					
	ς_1	ψ_1	ς_2	ψ_2	ς_3	ψ_3
<i>IMSA – SVM</i>						
$s = 1$	5.50	0.2	5.59	1.43	4.61	1.56
$s = 2$	4.15	0.06	5.42	0.74	4.43	0.55
$s = S_{opt} = 3$	4.24	0.009	5.19	0.33	3.10	0.14
<i>Bare SVM</i>	10.11	0.35	4.34	1.44	16.52	1.55
<i>MLP</i>	2.45	0.6	21.77	1.09	22.82	2.36
<i>RBF</i>	28.31	1.35	37.34	0.49	29.57	0.67

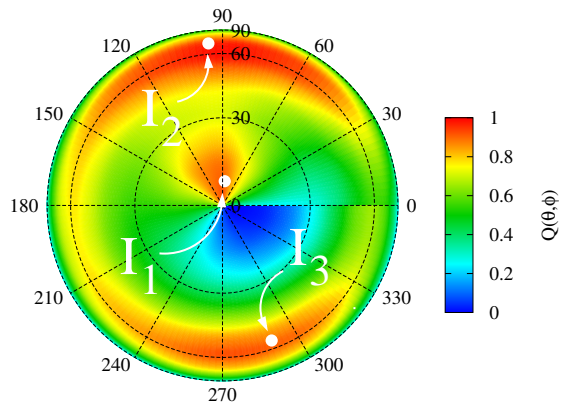
Table 5.4: *Multiple signals scenario, $I = 3$ (Configuration 1/1/1)*. Performance indexes when applying *IMSA – DOA*, single-step *SVM*, multi layer perceptron (*MLP*) neural network, and radial basis function (*RBF*) neural network.

<i>Method</i>	<i>DOA Indexes</i>							
	ς_1	ψ_1	ς_2	ψ_2	ς_3	ψ_3	ς_4	ψ_4
<i>IMSA – SVM</i>								
$s = 1$	6.84	0.40	24.37	0.40	23.31	1.48	25.47	1.56
$s = 2$	5.85	0.31	28.01	0.31	16.96	0.91	8.08	0.68
$s = S_{opt} = 3$	3.44	0.16	29.33	0.16	12.31	0.21	7.42	0.24
<i>Bare SVM</i>	8.37	2.89	24.71	2.89	26.52	2.89	25.68	2.89
<i>MLP</i>	38.98	0.52	8.91	0.52	35.34	1.82	17.46	1.69
<i>RBF</i>	15.19	0.32	18.69	0.32	40.65	1.81	22.01	0.91

Table 5.5: *Multiple signals scenario, $I = 4$ (Configuration 1/1/1/1)*. Performance indexes when applying *IMSA – DOA*, single-step *SVM*, multi layer perceptron (*MLP*) neural network, and radial basis function (*RBF*) neural network.



(a)



(b)

Figure 5.9: *Multiple signals scenario, $I = 3$ (Configuration 1/1/1)* - Probability maps obtained with different classification approaches: (a) *IMSA – SVM* [$s = S_{opt} = 3$] and (b) *single-step SVM* [$\Delta\theta = \Delta\theta_{(2)}^{(3)}$ and $\Delta\phi = \Delta\phi_{(2)}^{(3)}$].

<i>Method</i>	<i>DOA Indexes</i>							
	ς_1	ψ_1	ς_2	ψ_2	ς_3	ψ_3	ς_4	ψ_4
<i>IMSA – SVM</i>								
$s = 1$	15.50	0.89	11.51	0.89	45.50	2.98	57.71	2.98
$s = 2$	12.78	0.39	10.65	0.39	10.80	0.72	24.12	0.72
$s = S_{opt} = 3$	12.91	0.16	10.55	0.16	4.71	0.26	17.01	0.26
<i>Bare SVM</i>	15.46	0.91	11.64	0.91	46.53	3.17	58.66	3.17
<i>MLP</i>	9.35	0.29	8.66	0.29	13.75	1.75	27.43	1.75
<i>RBF</i>	8.06	0.26	8.77	0.26	14.84	0.57	9.50	0.57

Table 5.6: *Multiple signals scenario, $I = 4$ (Configuration 2/2)*. Performance indexes when applying *IMSA – DOA*, single-step *SVM*, multi layer perceptron (*MLP*) neural network, and radial basis function (*RBF*) neural network.

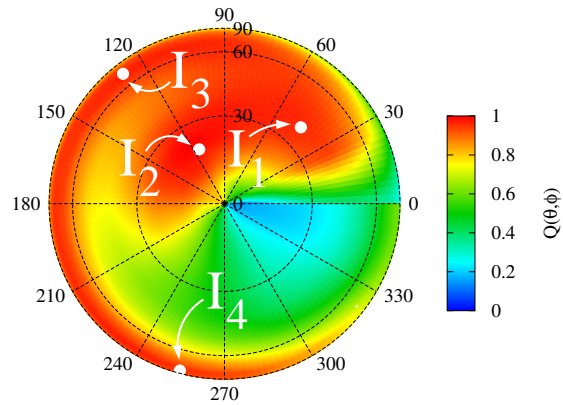
to which the incidence directions of the actual signals belong as pointed out by the numerical indexes $\psi^{(i)}$, $i = 1, \dots, I$ in Tab. 5.5. On the other hand, it should be noticed that the *DOA* estimation process tends to cluster multiple regions-of-incidence in a single *ARoI* when the angular separations among the signals reduce. Such an event takes place also in correspondence with the “*Configuration 2/2*” [Fig. 5.11(d) - Tab. 5.6] where two *ARoIs* are identified. It is even more evident in Fig. 5.11(e) (Tab. 5.7) where the angular incidences of three signals are detected in only one *ARoI*. The “clustering” effect is quantitatively pointed out by the behavior of the averaged localization index (Tab. 5.1 - fourth block) when dealing with the complete test set ($T_4^{(test)} = 50$) to which previous examples belong. As a matter of fact, there is a significant increase of the $avg(\hat{\varsigma})$ compared to the values of the same quantity when $I = 1, 2, 3$ [$avg(\hat{\varsigma}_1) = 17.29$ vs. $avg(\hat{\varsigma}_1) = 2.81$, $avg(\hat{\varsigma}_2) = 4.51$, $avg(\hat{\varsigma}_3) = 5.55$], even though the value of $avg(\hat{\psi})$ remains close to those of other multiple-signals configurations since the estimated *ARoIs* still carefully identify the actual incidence areas.

The fourth and fifth experiments deal with more critical test scenarios since the examples under test are concerned with a number of signals different from that in the training set (i.e., $I \neq 1, 2, 3, 4$). More specifically, let us consider the *Clustered Distribution* of $I = 18$ signals with incidence directions indicated by the white points in Fig. 5.12. It is worth noticing that such a configuration turns out to be not admissible (i.e., $I = 18$ estimates cannot be obtained) for signal subspace-based array processing techniques as *2D-unitary ESPRIT* when the planar array structure at hand is used. As a matter of fact, the maximum number of sources *2D-unitary ESPRIT* can handle is equal to [67]

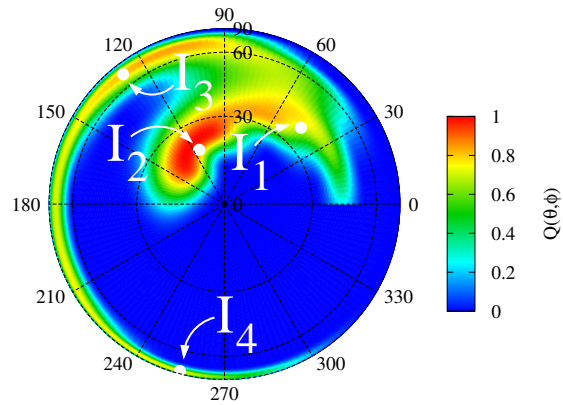
$$I_{max}^{2D\text{ ESPRIT}} = \min \{U \times (V - 1); V \times (U - 1)\} \quad (5.16)$$

being $M = U \times V$. On the other hand, it should be considered that an high

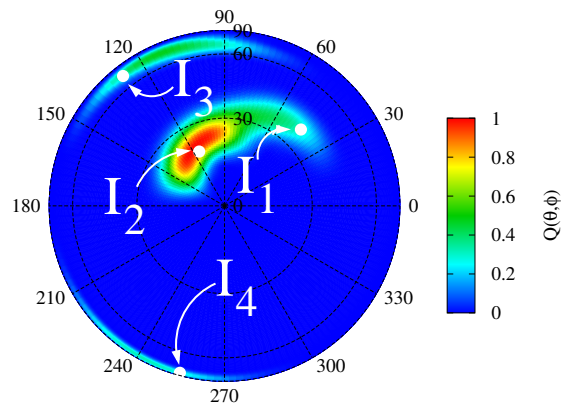
5.3. NUMERICAL SIMULATIONS AND RESULTS



(a)

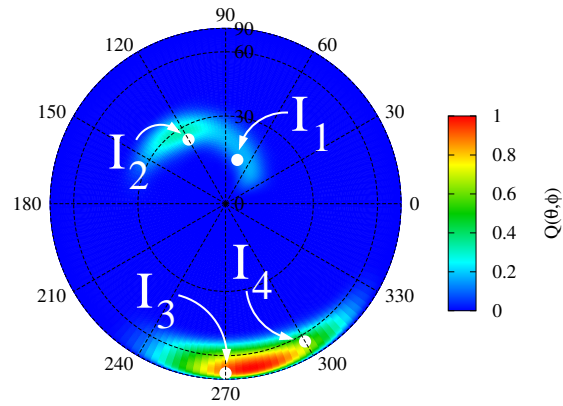


(b)

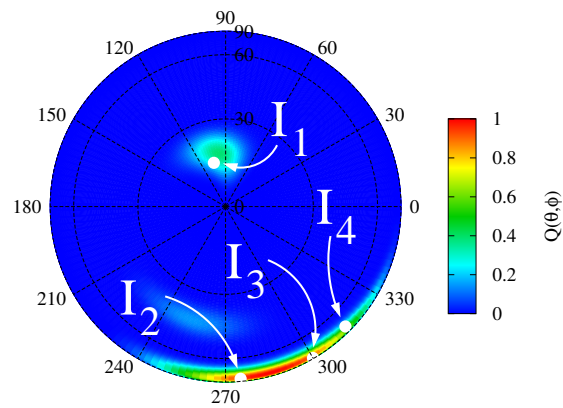


(c)

Figure 5.10: *Multiple signals scenario, $I = 4$* - Probability maps obtained with the *IMSA – SVM*. Configuration 1/1/1/1: step (a) $s = 1$, (b) $s = 2$, and (c) $s = S_{opt} = 3$.



(d)



(e)

Figure 5.11: *Multiple signals scenario, $I = 4$ - Configuration 2/2: step $s = S_{opt} = 3$ (d); Configuration 1/3: step $s = S_{opt} = 3$ (e).*

5.3. NUMERICAL SIMULATIONS AND RESULTS

<i>Method</i>	<i>DOA Indexes</i>							
	ς_1	ψ_1	ς_2	ψ_2	ς_3	ψ_3	ς_4	ψ_4
<i>IMSA – SVM</i>								
$s = 1$	16.98	0.88	39.13	2.81	54.57	2.81	64.78	2.81
$s = 2$	16.51	0.62	6.04	1.70	22.43	1.70	35.70	1.70
$s = S_{opt} = 3$	8.13	0.59	6.18	1.46	11.84	1.46	28.89	1.46
<i>Bare SVM</i>	17.38	0.87	39.45	2.85	54.87	2.85	65.72	2.85
<i>MLP</i>	11.62	0.19	27.46	1.08	11.41	1.08	8.15	1.08
<i>RBF</i>	6.51	0.10	16.85	0.10	3.01	0.10	20.63	0.10

Table 5.7: *Multiple signals scenario, $I = 4$ (Configuration 1/3)*. Performance indexes when applying *IMSA – DOA*, single-step *SVM*, multi layer perceptron (*MLP*) neural network, and radial basis function (*RBF*) neural network.

<i>Method</i>	<i>DOA Indexes</i>	
	$\hat{\varsigma}$	$\hat{\psi}$
<i>IMSA – SVM</i>	1.20	0.21
<i>Bare SVM</i>	2.82	1.94
<i>MLP</i>	13.78	1.66
<i>RBF</i>	13.62	1.21

Table 5.8: *Multiple signals scenario, $I = 18$ (Clustered Distribution)*. Performance indexes when applying *IMSA – DOA*, single-step *SVM*, multi layer perceptron (*MLP*) neural network, and radial basis function (*RBF*) neural network.

dimensional array processing is enabled widening the size of the planar array (i.e., the number of array sensors) at the expense of the computational complexity that, unlike *SVM*-based methods, exponentially grows.

Figure 5.12 compares the “convergence” ($s = S_{opt} = 3$) map provided by the *IMSA – SVM* and the ones from other single-step classifiers. As it can be observed, the multi-scaling process is still able to carefully estimate the *ARoI* to which the actual signals belong with a degree of accuracy higher than that from the other techniques both in terms of localization and area extension (Tab. 5.8). Similar conclusions hold true when dealing with the detection of the signals distribution displayed in Fig. 5.13, although the detection of the single signal on the bottom of the region of analysis appears to be more critical probably because of the absence of similar spatial configurations in the training set.

Finally, the last experiment is concerned with a scenario where there are not signals that impinge on the array and the noise level has been varied from the

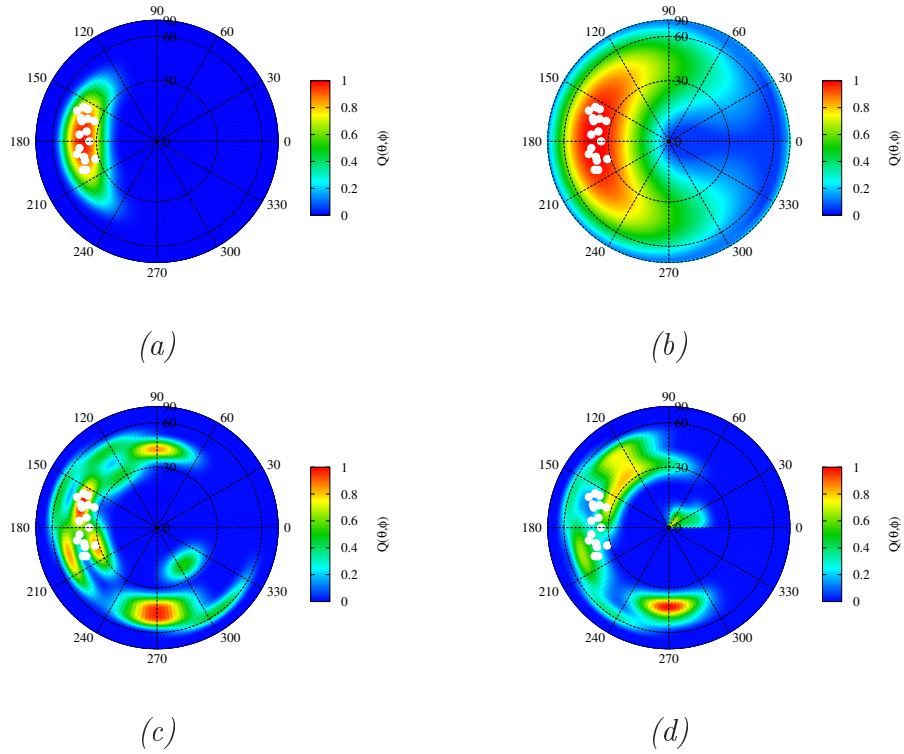


Figure 5.12: *Multiple signals scenario* ($I = 18$ - *Clustered Distribution*) - Probability maps obtained with different classification approaches: (a) *IMSA-SVM* ($s = S_{opt} = 3$), (b) *single-step SVM*, (c) *multi layer perceptron (MLP) neural network*, and (d) *radial basis function (RBF) neural network* [$\Delta\theta = \Delta\theta_{(2)}^{(3)}$ and $\Delta\phi = \Delta\phi_{(2)}^{(3)}$].

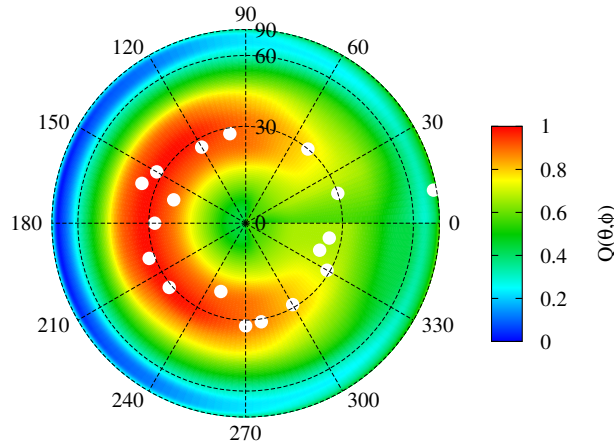


Figure 5.13: *Multiple signals scenario* ($I = 18$ - *Sparse Distribution*) - Probability maps determined by the *IMSA – SVM* at the convergence ($s = S_{opt} = 2$ - $\Delta\theta_{(1)}^{(2)} = 5^\circ$ and $\Delta\phi_{(1)}^{(2)} = 20^\circ$).

reference value used for the *SVM* training [$P_n = 20$ dB (*Test Set*) vs. $P_n = 0$ dB (*Training Set*)] thus further complicating the test case. As a matter of fact, neither the free-case example is present in the training set nor the same noise level has been “learned”. Nonetheless, the *SVM*-based classifier did not detected the presence of any signal thus defining a uniform distribution of probability [Fig. 5.14(a)]. Otherwise, the other methods give color-maps with some “artifacts” [see Figs. 5.14(b)-5.14(c)] although characterized by very small values of the probability of signal incidence.

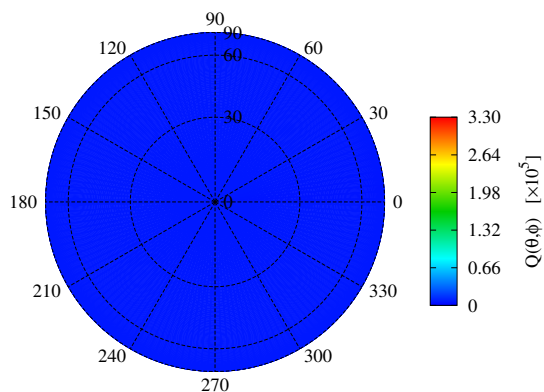
5.3.3 Dipole Array Antenna

In the last experiment, a uniform array of $\frac{\lambda}{2}$ -dipoles is taken into account with dipoles oriented along the x axis. Therefore, the effective length [82] of the array element turns out to be

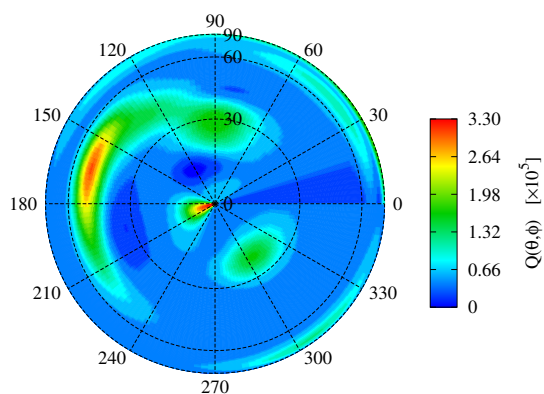
$$\underline{e}_m = \frac{\lambda}{\pi} \left[\frac{\cos\left(\frac{\pi}{2} \sin\theta \cos\phi\right)}{1 - \sin^2\theta \cos^2\phi} \right] [(\cos\theta \cos\phi) \underline{\theta} - (\sin\phi) \underline{\phi}] \quad (5.17)$$

Moreover, the inter-element distance has been chosen equal to $d_x = 0.65\lambda$ and $d_y = 0.5\lambda$ [85]. Then, a subset of the experiments of the previous sections, but with the dipole array, has been dealt with to evaluate the applicability of the *IMSA – SVM* approach to non-ideal electromagnetic scenarios, as well.

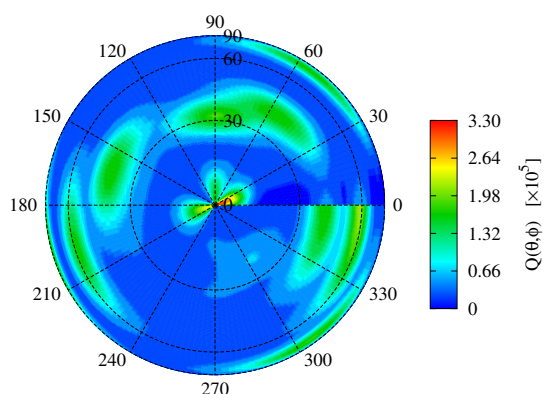
In the first example ($I = 1$), the multi-scaling procedure stops after $S_{opt} = 4$ iterations and the final result is shown in Fig. 5.15. Likewise the case with



(a)



(b)



(c)

Figure 5.14: *No-signals scenario* [$I = 0$; $P_n = 20$ dB (*Test Set*) - $P_n = 0$ dB (*Training Set*)] - Probability maps obtained with different classification approaches: (a) *IMSA-SVM* ($s = S_{opt} = 1$), (b) multi layer perceptron (*MLP*) neural network, and (c) radial basis function (*RBF*) neural network.

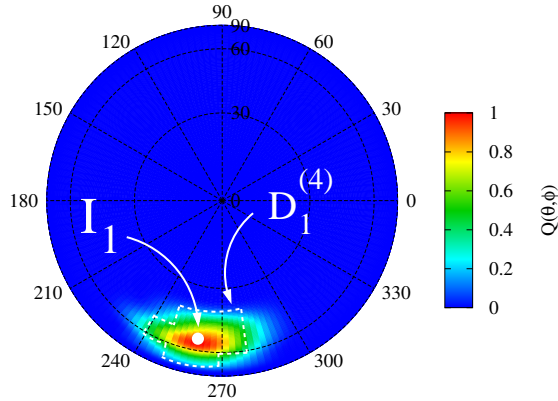


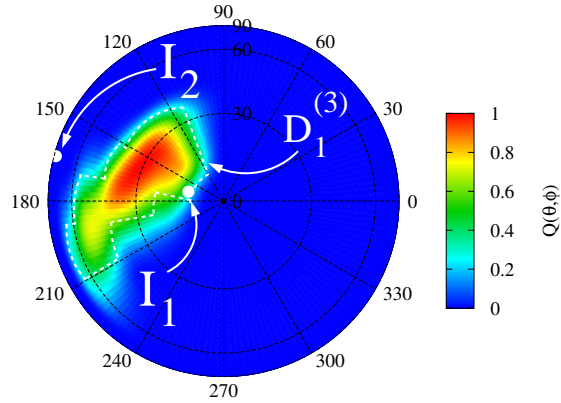
Figure 5.15: *Dipole Array*, $I = 1$ - Probability map determined by the *IMSA – DOA* [$s = S_{opt} = 4$].

point-like sources, the estimations of both the location and the incidence area improve at each iteration starting from $\zeta^{(1)} = 43.19$ and $\psi^{(1)} = 2.48$ down to $\zeta^{(S_{opt})} = 2.96$ and $\psi^{(S_{opt})} = 0.06$, where $\zeta^{(2)} = 12.65$, $\zeta^{(3)} = 5.41$ and $\psi^{(2)} = 0.75$, $\psi^{(3)} = 0.21$. In this case, the performance are comparable to that in Sect. 5.3.1. Different conclusions arise when processing the data of the two-signal scenario [Fig. 5.16(a)]. In such a case, only the I_1 (i.e., the signal with the lowest elevation θ) is detected [Fig. 5.16(a)]. Such an event does not depend on the *DOA* detection method, but from the antenna array at hand. As a matter of fact, the radiation pattern of the array element is omnidirectional in the $z - y$ plane (i.e., $\phi = 90^\circ$ and $\phi = 270^\circ$) with a θ_{3dB} angle of almost 80° degrees [82]. Therefore, the gain of the dipole is lower along the direction with higher θ s, being $\phi_1 = \phi_2 = 165^\circ$. Otherwise, when the actual configuration is described by a set of signals coming from the directions ($\theta_1 = 30^\circ$, $\phi_1 = 60^\circ$) and ($\theta_2 = 30^\circ$, $\phi_2 = 300^\circ$), the *IMSA – SVM* method still gives accurate estimates [Fig. 5.16(b)] although with non-ideal isotropic receiving sensors.

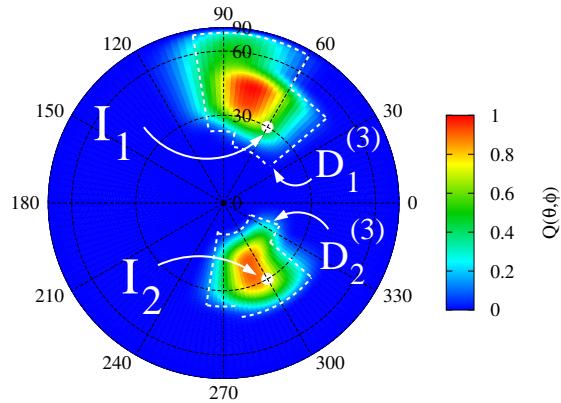
5.4 Conclusions

From the analysis carried out within this research work and summarized in this chapter, the following conclusions can be drawn:

- the use of a classifier based on *SVM* allows one to estimate the *DOA* probability map in real time;
- thanks to the *SVM* generalization capability, the *IMSA – SVM* behaves properly when dealing with complex electromagnetic scenarios non-



(a)



(b)

Figure 5.16: *Dipole Array, $I = 2$* - Probability map determined by the *IMSA – DOA* when (a) $I_1 = (\theta_1 = 12^\circ, \phi_1 = 165^\circ)$, $I_2 = (\theta_2 = 82^\circ, \phi_2 = 165^\circ)$ [$s = S_{opt} = 3$] and (b) $I_1 = (\theta_1 = 30^\circ, \phi_1 = 60^\circ)$, $I_2 = (\theta_2 = 30^\circ, \phi_2 = 300^\circ)$ [$s = S_{opt} = 3$].

5.4. CONCLUSIONS

necessarily belonging to the set of training examples;

- the *SVM*-based approach is able to estimate the *DOAs* of a number of sources greater than the maximum allowed by conventional eigenvalue decomposition methods for a fixed planar array geometry;
- unlike $2-D$ subspace-based algorithms, the computational complexity does not increase with the size of the rectangular array;
- the proposed *LBE* technique adapts to element failure or other source of errors coming from the tolerances in the array structure that cause non-negligible performance degradation in conventional estimation techniques which require highly calibrated antennas with identical radiation properties;
- the *a-priori* knowledge (deterministic or statistical) on the array configuration and radiation pattern characteristics can be easily and usefully exploited by defining suitable *IMSA – SVM* training sets;
- the multi-scaling procedure (*IMSA*) provides good results dealing with both single-signal and multiple-signals configurations with an angular resolution comparable to that of other state-of-the-art *DOA* algorithms;
- system complexity, classifier architecture, and computational costs significantly reduce with respect to the “bare” classification.

Chapter 6

Real-Time Passive Localization and Tracking

An innovative strategy for passive localization of transceiver-free objects is presented. The localization is yielded by processing the received signal strength data measured in an infrastructured environment. The problem is reformulated in terms of an inverse source one, where the probability map of the presence of an equivalent source modeling the moving target is looked for. Towards this end, a customized classification procedure based on a support vector machine is exploited. Selected, but representative, experimental results are reported to assess the feasibility of the proposed approach and to show the potentialities and applicability of this passive and unsupervised technique.

6.1 Introduction

In the recent years, there has been a wide and rapid diffusion of wireless sensor networks (*WSNs*) [86] thanks to the availability of such low-power and pervasive devices integrating on-board sensing, processing, and radio frequency (*RF*) circuitry for information transmission. Usually, short-range communications are at hand since the wireless nodes are generally densely distributed and characterized by low power consumption to ensure a long lifetime. Therefore, *WSNs* have been also profitably used for location and tracking purposes. In such a framework, the main efforts have been devoted to develop ad-hoc systems based on dedicated transponders/sensors [87] or assuming an “active” target equipped with a transmitting device [88][89]. Different properties of the received signal, such as the time of arrival (*TOA*) and the direction of arrival (*DOA*), have been successfully exploited to address the localization problem [90][91]. Other modalities to locate active targets are based on the evaluation of the received signal strength (*RSS*) [92][93][94][95]. This is an easily measurable quantity that has been also used to localize the wireless nodes of the network through effective triangulation strategies [93]. Moreover, the distance between nodes has been estimated thanks to simplified radio propagation models. Although easier than a “passive” localization technique, the main drawback of these approaches is the need of the target to be equipped with an ad-hoc device. Whether such a fact can be considered negligible when tracking either objects or animals (although the costs unavoidably increase), other problems arise when dealing with people (e.g., privacy) and especially with non-cooperative subjects as for elderly people. Moreover, such wearable devices can undergo (casual or voluntary) damages thus limiting the reliability of the tracking system.

Other strategies concerned with transceiver-free targets have been also presented in the scientific literature. State-of-the-art approaches are based on Doppler radar systems able to estimate the distance between the target and the sensor [96]. As a matter of fact, moving targets can be tracked through the analysis of the Doppler signature induced by the object motion [97]. Unfortunately, the arising performance in real environments can be strongly influenced by non-negligible instabilities leading to several false alarms. Furthermore, slow-moving targets [98] are not generally detected.

This paper is aimed at presenting an inversion procedure, preliminary validated in [99], for the localization and tracking of passive objects starting from the measurements of the *RSS* indexes available at the nodes of a *WSN*. Since the transmission of information among the wireless nodes is allowed by *RF* signals, the arising electromagnetic radiations can be also profitably exploited to sense the surrounding environment. Indeed, any target lying within the environment interacts with the electromagnetic waves radiated by the nodes. Therefore, the measurements of the perturbation effects on the other receiving nodes is dealt with a suitable inversion strategy to determine the equivalent source model-

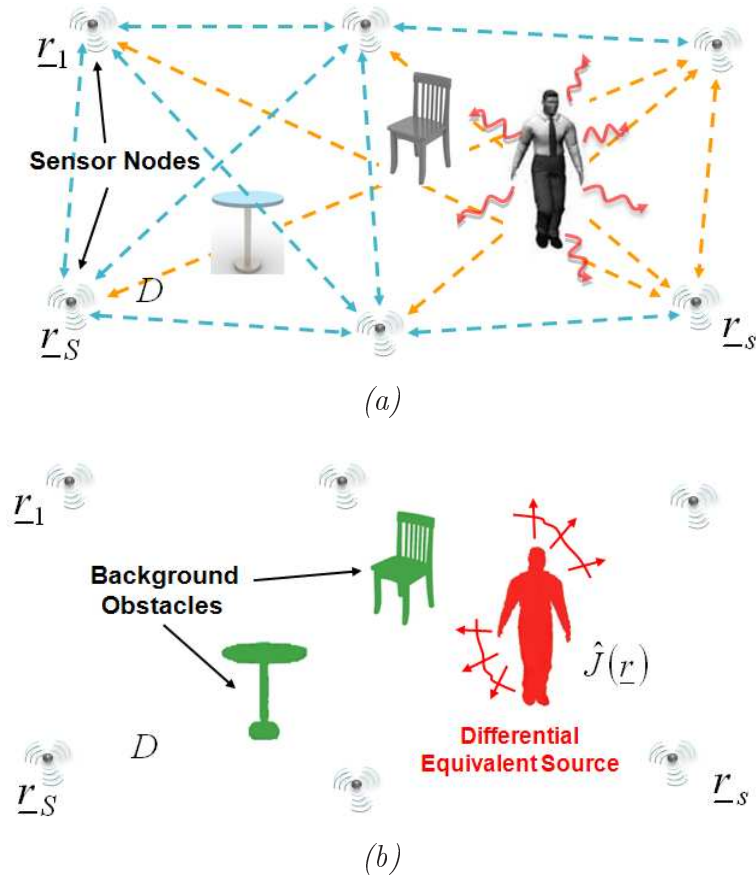


Figure 6.1: *Equivalent Tracking Problem* - Sketch of (a) the tracking scenario and (b) the equivalent inverse problem.

ing the presence of the target/scatterer generating the perturbation itself. By virtue of the fact that the number of nodes in a *WSN* can vary and the need to have a simple and flexible tracking/localization method allowing real-time estimates, a learning-by-examples (*LBE*) strategy based on a Support Vector Machine (*SVM*) is used.

The outline of the chapter is as follows. The mathematical issues concerned with the proposed approach are detailed in Sect. 6.2 where the *SVM*-based method is described, as well. In Sect. 6.3, representative results from a wide set of experiments dealing with the tracking of single as well as multiple targets in both outdoor and indoor *WSN* deployments are shown. Eventually, some conclusions are drawn (Sect. 6.4).

6.2 Mathematical Formulation

Let us consider the two-dimensional ($2D$) scenario shown in Fig. 6.1(a). The investigation domain D is inhomogeneous and constituted by a set of obstacles and moving targets to be localized/tracked all lying in free-space. The known host scenario (i.e., the target-free domain) is described by the object function $\tau_h(\underline{r}) = \varepsilon_h(\underline{r}) - 1 - j\frac{\sigma_h(\underline{r})}{\omega\varepsilon_0}$ where ω is the working angular frequency, $\underline{r} = (x, y)$ is the position vector, ε_h and σ_h being the dielectric permittivity and the conductivity, respectively. Moreover, the target/s is/are identified by the dielectric distribution $\tau_o(\underline{r})$, $\underline{r} \in D_o$. The area under test is infrastructured with a *WSN* and S nodes are deployed at \underline{r}_s , $s = 1, \dots, S$ spatial locations. The s -th wireless node radiates an electromagnetic signal, $\xi_s^{inc}(\underline{r})$ ⁽¹⁾¹, and the field measured by the other $S - 1$ nodes and arising from the interactions of the incident field with the scenario under test is given by

$$\xi_s^{tot}(\underline{r}_m) = \xi_s^{inc}(\underline{r}_m) + \int_D J(\underline{r}') \mathcal{G}_0(\underline{r}', \underline{r}_m) d\underline{r}' \quad (6.1)$$

where \mathcal{G}_0 is the free-space Green's function [100] and \underline{r}_m is the position of the m -th ($m = 1, \dots, S - 1$) receiving node. As a matter of fact, the field induced in D is equivalent to that radiated in free-space by an equivalent current density $J(\underline{r})$ [101] modeling the presence of whatever discontinuity of the free-space (i.e., both the obstacles and the moving targets)

$$J(\underline{r}) = \tau(\underline{r}) \xi^{tot}(\underline{r}), \quad \underline{r} \in D \quad (6.2)$$

where $\tau(\underline{r}) = \tau_o(\underline{r})$ if $\underline{r} \in D_o$ and $\tau(\underline{r}) = \tau_h(\underline{r})$ if $\underline{r} \in D_h = D - D_o$, D_o and D_h being the support of the targets and its complementary area.

Equation (6.1) can be reformulated in a different fashion by defining a differential equivalent current density $\hat{J}(\underline{r})$ radiating in the inhomogeneous host medium [100] [Fig. 6.1(b)]. The radiated field can be then expressed as follows

$$\begin{aligned} \xi_s^{tot}(\underline{r}_m) &= \xi_s^{inc}(\underline{r}_m) + \int_D \tau_h(\underline{r}') \xi_{s,u}^{tot}(\underline{r}') \mathcal{G}_0(\underline{r}', \underline{r}_m) d\underline{r}' + \\ &\quad \int_{D_0} \hat{J}(\underline{r}') \mathcal{G}_1(\underline{r}', \underline{r}_m) d\underline{r}' \end{aligned} \quad (6.3)$$

where $\hat{J}(\underline{r}) = \hat{\tau}(\underline{r}) \xi_{s,p}^{tot}(\underline{r})$ and $\hat{\tau}(\underline{r}) = \tau(\underline{r}) - \tau_h(\underline{r})$ is the differential object function. In (6.3), the second term on the right side is the field scattered from the host medium without targets, $\xi_{s,u}^{tot}$ being the electric field related to ξ_s^{inc} in correspondence with the target-free scenario. Moreover, \mathcal{G}_1 is the inhomogeneous Green's function for the target-free configuration [100], which satisfies the

¹ (1) The scalar case has been considered to simplify the notation. However, the extension to the vectorial case is straightforward.

following integral equation

$$\mathcal{G}_1(\underline{r}, \underline{r}') = \mathcal{G}_0(\underline{r}, \underline{r}') + \int_D \tau_h(\underline{r}') \mathcal{G}_0(\underline{r}, \underline{r}'') \mathcal{G}_1(\underline{r}'', \underline{r}') d\underline{r}''. \quad (6.4)$$

Since the host medium is *a-priori* known, Equation (6.3) can be rewritten as

$$\xi_s^{tot}(\underline{r}_m) = \hat{\xi}_s^{inc}(\underline{r}_m) + \int_{D_o} \hat{J}(\underline{r}') \mathcal{G}_1(\underline{r}', \underline{r}_m) d\underline{r}' \quad (6.5)$$

where $\hat{\xi}_s^{inc}(\underline{r}_m)$ is the field of the scenario without targets and equivalent to an “incident” field on the targets.

With the knowledge of \mathcal{G}_1 (i.e., the knowledge of the target-free scenario) the scattering problem turns out to be the retrieval of the differential source \hat{J} occupying the target domain D_o . The detection of the target position and the definition of the target trajectory in D can be then formulated as the definition of the support of the differential equivalent source, which satisfies the inverse scattering equation (6.5), starting from the measurements of $\xi_s^{tot}(\underline{r}_m)$, $m = 1, \dots, S - 1$. This is possible in a *WSN*-infrastructured environment since the nodes at hand are simple and cheap devices that give an indirect estimate of the field value through the *RSS* index. Accordingly, the *RSS* is measured at the m -th node when the s -th node is transmitting by considering both the target-free scenario [$\hat{\xi}_s^{inc}(\underline{r}_m)$ knowledge] and the presence of targets within D [$\xi_s^{tot}(\underline{r}_m)$ knowledge] and the differential field $\xi_{m,s}^{sct} = \xi_s^{tot}(\underline{r}_m) - \hat{\xi}_s^{inc}(\underline{r}_m)$ could be used for the inversion procedure.

However, it is worth to take into account that the power radiated by the *WSN* nodes can vary due to several factors (e.g., battery level of the *WNS* nodes, environmental conditions) thus “blurring” the data acquisition and, consequently, complicating the solution of the inverse problem at hand. To overcome this drawback, the inversion is statistically recast as the definition of the probability that a target is located in a position of D starting from the knowledge of $\xi_{m,s}^{sct}$, $s = 1, \dots, S$, $m = 1, \dots, S$, $m \neq s$. The arising classification problem is then solved by means of a suitable *SVM*-based approach. More specifically, the region D where the targets are looked for is partitioned into a grid of C cells centered at \underline{r}_c , $c = 1, \dots, C$. Each c -th cell is characterized by its state, χ_c , which can be either empty ($\chi_c = -1$) or occupied ($\chi_c = 1$) whether a target (i.e., the corresponding differential equivalent source) is present or absent. Moreover, the probability that a target belongs to the c -th cell, $\alpha_c = Pr\{\chi_c = 1 | \underline{\Gamma}, c\}$, is given by

$$\alpha_c = \frac{1}{1 + \exp\{p\mathcal{H}[\underline{\varphi}(\underline{\Gamma}, c)] + q\}}, \quad c = 1, \dots, C \quad (6.6)$$

where $\underline{\Gamma} = \{\xi_{m,s}^{sct}; s = 1, \dots, S; m = 1, \dots, S; m \neq n\}$, and p, q are unknown parameters to be determined [6]. In (6.6), the function $\underline{\varphi}(\cdot)$ is a non-linear mapping from the data of the original input space, $\underline{\Gamma}$, to a higher dimensional space (called *feature space*) where the data are more easily separable through a simpler function (i.e., the hyperplane \mathcal{H}).

6.3. EXPERIMENTAL VALIDATION

The hyperplane \mathcal{H} is off-line defined throughout the *training phase* by exploiting the knowledge of a set of T known examples where both the input data ($\underline{\Gamma}$, $t = 1, \dots, T$) and the corresponding maps ($\underline{\chi}_t = \{\chi_{c,t}; c = 1, \dots, C\}$, $t = 1, \dots, T$) are available. Usually, a linear decision function is adopted

$$\mathcal{H} [\underline{\varphi}(\underline{\Gamma}, c)] = \underline{w} \cdot \underline{\varphi}(\underline{\Gamma}, c) + b, \quad c = 1, \dots, C \quad (6.7)$$

\underline{w} and b being an unknown normal vector and a bias coefficient, respectively. The decision function parameters unequivocally define the decision plane and are computed in the training phase by minimizing the following cost function

$$\Psi(\underline{w}) = \frac{\|\underline{w}\|^2}{2} + \frac{\lambda}{\sum_{t=1}^T C_+^{(t)}} \sum_{t=1}^T \sum_{i=1}^{C_+^{(t)}} \eta_{c_+}^{(t)} + \frac{\lambda}{\sum_{t=1}^T C_-^{(t)}} \sum_{t=1}^T \sum_{f=1}^{C_-^{(t)}} \eta_{c_-}^{(t)} \quad (6.8)$$

subject to the separability constraints

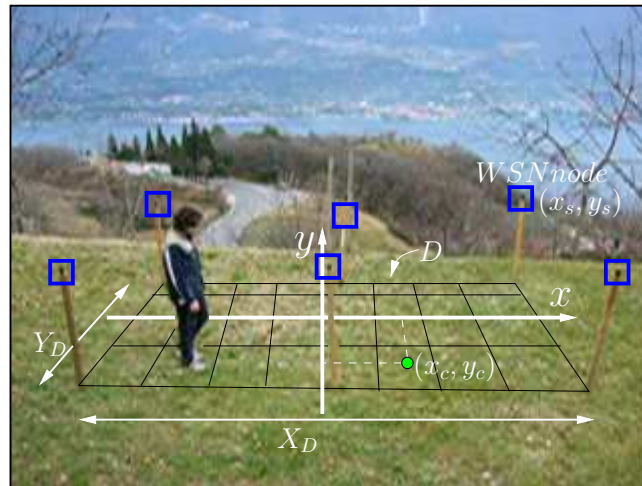
$$\begin{aligned} \underline{w} \cdot \underline{\varphi}(\underline{\Gamma}, c) + b &\geq 1 - \eta_{c_+}^{(t)}, \quad c = 1, \dots, C \\ \underline{w} \cdot \underline{\varphi}(\underline{\Gamma}, c) + b &\leq \eta_{c_-}^{(t)} - 1, \quad c = 1, \dots, C \end{aligned} \quad (6.9)$$

where λ is a user-defined hyperparameter [102] that controls the trade-off between the training error and the model complexity to avoid overfitting. Moreover, $\eta_{c_+}^{(t)}$ and $\eta_{c_-}^{(t)}$ are the so-called *slack variables* related to the misclassified patterns. They are introduced because the training data are usually not completely separable in the feature space by means of a linear hyperplane.

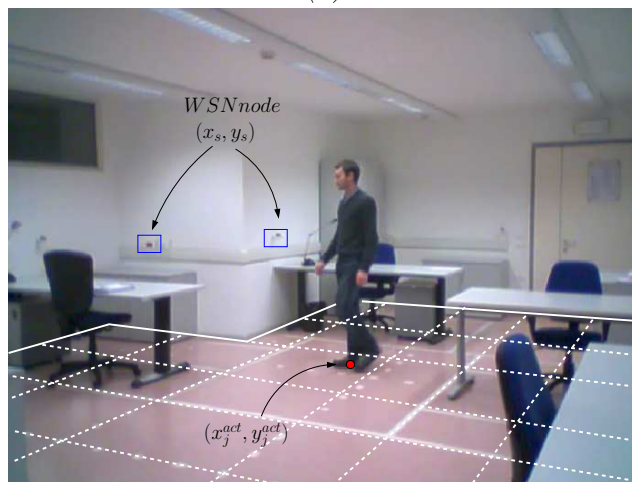
The minimization of (6.8) is performed following the guidelines detailed in [38] and also exploiting the so-called kernel trick method [6].

6.3 Experimental Validation

The feasibility and the effectiveness of the proposed approach have been assessed through an extensive experimental validation carried out in both indoor and outdoor scenarios (Fig. 6.2). The nodes have been placed at fixed positions $\underline{r}_s = (x_s, y_s)$, $s = 1, \dots, S$, on the perimeter of the investigation area D . In all experiments, $S = 6$ Tmote Sky nodes have been used and the region D has been assumed having the same size ($-20\lambda \leq x \leq 20\lambda$ and $-12\lambda \leq y \leq 12\lambda$) whatever the scenario at hand, λ being the free-space wavelength of the wireless signals transmitted by the nodes (e.g., $f = 2.4 \text{ GHz}$). Although the same topology has been adopted for outdoor as well as indoor situations, two different trainings of the *SVM*-based approach have been performed since the arising electromagnetic phenomena significantly differ (e.g., the electromagnetic interferences). Otherwise, the calibration of training examples (T), the separation hyperplane $\mathcal{H}(\lambda)$, and the discretization of the investigation area (C) has been performed only once, namely for the outdoor case, since the format of the data processed by the *SVM* does not change. More in detail, the following setup has been considered:



(a)



(b)

Figure 6.2: *Problem Geometry* - Plots of (a) the outdoor and (b) the indoor environments with WSN-based tracking system.

6.3. EXPERIMENTAL VALIDATION

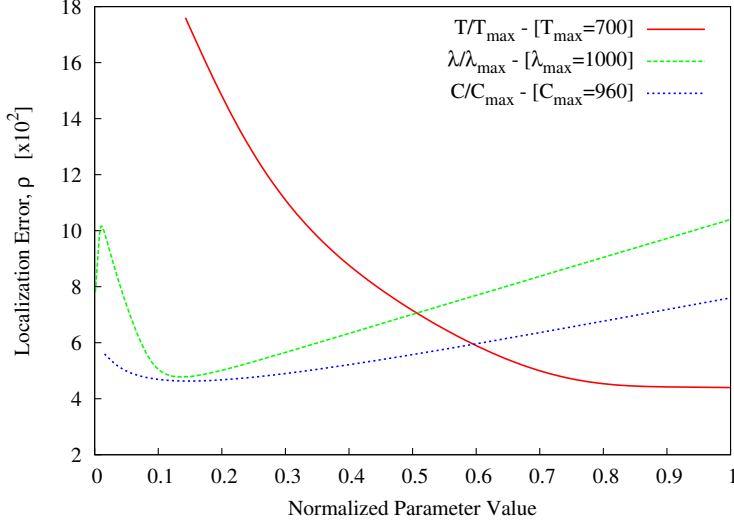


Figure 6.3: *Calibration* - Localization error as a function of the *SVM* control parameters: T ($\lambda = 100$, $C = 60$), λ ($T = 500$, $C = 60$), and C ($T = 500$, $\lambda = 100$).

$T \in [100, 700]$ with step $\Delta T = 100$, $\lambda = 10^i$, $i = \{0, 1, 2, 3\}$, and $C \in [15, 960]$ from a rough discretization with $C = 5 \times 3$ cells of dimension $4\lambda \times 4\lambda$ to the finest one having $C = 40 \times 24$ cells of dimension $\lambda \times \lambda$. These values have been calibrated with reference to single-target experiments by evaluating the behavior of the localization error defined as

$$\rho = \frac{\sqrt{(x_j^{act} - x_j^{est})^2 + (y_j^{act} - y_j^{est})^2}}{\rho_{max}} \quad (6.10)$$

where $\underline{r}_j^{act} = (x_j^{act}, y_j^{act})$ and $\underline{r}_j^{est} = (x_j^{est}, y_j^{est})$ are the actual and estimated positions of the target, ρ_{max} being the maximum admissible location error. As for the test case at hand, it turns out that $\rho_{max} = \sqrt{X_D^2 + Y_D^2}$ and \underline{r}_j^{est} has been calculated from the probability map according to the following relationships

$$\begin{aligned} x_j^{est} &= \frac{\sum_{c=1}^C \alpha_c x_c}{\sum_{c=1}^C \alpha_c} \\ y_j^{est} &= \frac{\sum_{c=1}^C \alpha_c y_c}{\sum_{c=1}^C \alpha_c}. \end{aligned} \quad (6.11)$$

Figure 6.3 gives the normalized values of the location indexes obtained for different combinations of the control parameters. Each plot refers to the variation of a control parameter keeping constant the others ($T^{opt} = 500$, $\lambda^{opt} = 100$, $C^{opt} = 60$).

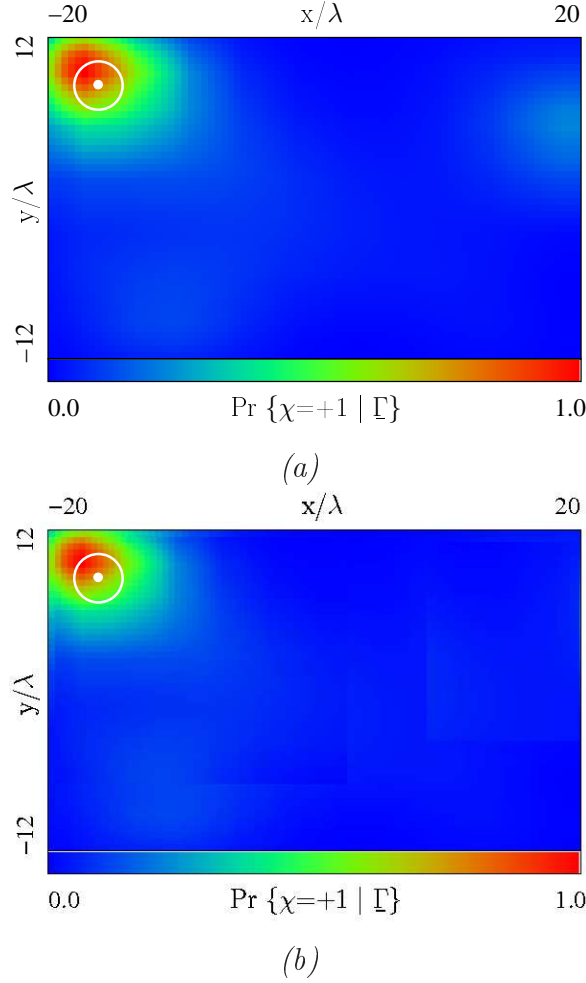


Figure 6.4: *Single target localization - Outdoor Scenario* - Probability maps of the investigation region D obtained when the test data (a) belongs and (b) does not belong to the training data set.

As far as the *SVM* training phase is concerned, the reference measurements have been first collected in the target-free scenarios [i.e., $\hat{\tau}(\underline{r}) = 0 \Rightarrow \xi_{m,s}^{sct} = 0$, $m, s = 1, \dots, S$, $m \neq s$]. Successively, the sets of *RSS* measurements [i.e., $RSS_{m,s}(t)$, $m, s = 1, \dots, S$, $m \neq s$, $t = 1, \dots, T$] have been collected with the target located at T different positions, $\underline{r}_j = (x_j, y_j)$, $j = 1, \dots, T$, randomly selected within D to cover as uniformly as possible the whole area under test.

As regards the *SVM* test step, both single ($J = 1$) and multiple ($J = 2$) target tracking problems have been considered.

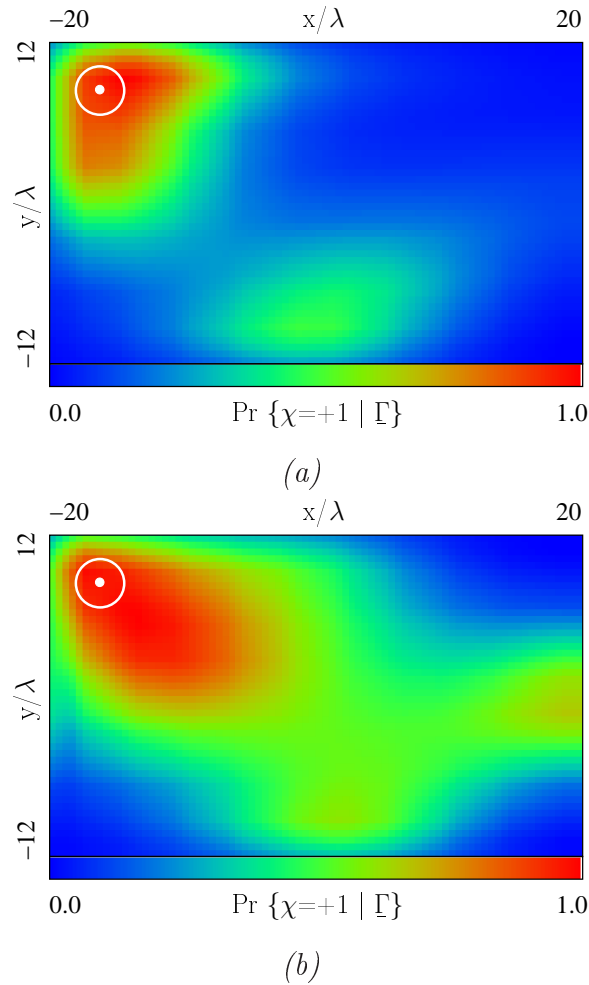


Figure 6.5: *Single target localization - Indoor Scenario* - Probability maps of the investigation region D obtained when the test data (a) belongs and (b) does not belong to the training data set.

6.3.1 Single target tracking

The first experiment deals with the outdoor tracking of a single human being moving inside D . Figure 6.4 shows the probability map estimated when the target is at $\underline{r}_1^{act} = (-16\lambda, 8\lambda)$. The circle gives the actual position. Two different cases have been considered. More specifically, Figure 6.4(a) shows the probability map assuming that the same experiment has been taken into account in the training phase. Differently, the map in Fig. 6.4(b) has been obtained the example not belonging to the training data set. It is worth noting that the target is correctly localized in both maps since the center of the target lies within the region with higher probability. The same experiment has been successively considered for the indoor scenario. The results of the *SVM*-based localization process are shown in

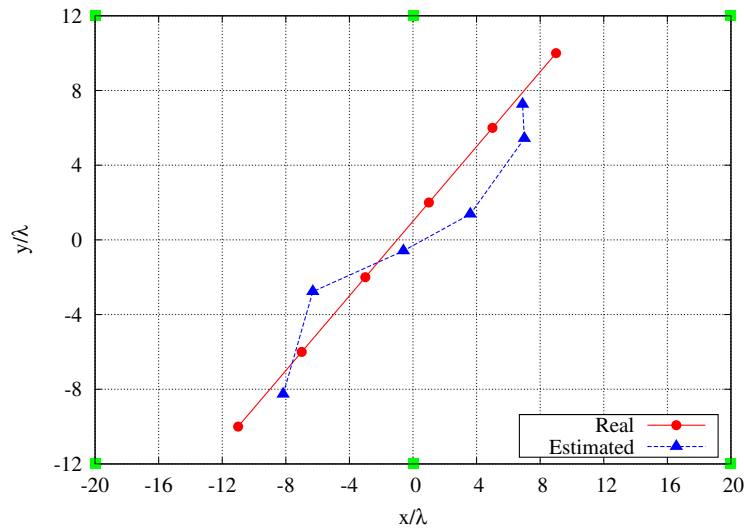


Figure 6.6: *Single target tracking - Outdoor Scenario - Actual and estimated trajectories.*

Fig. 6.5. As for the previous test, the results when the same example has been either considered [Fig. 6.5(a)] or not [Fig. 6.5(b)] in the training phase have been reported. As expected, the values of the localization errors increase whatever the training because of the complexity of the electromagnetic interactions arising from the presence of the walls (i.e., multiple reflections) in indoor environments. Nevertheless, the region with high probability still contains the actual position of the target thus demonstrating a good degree of reliability of the approach also in this case.

Let us now consider a single target moving outdoor inside D along the straight line shown in Fig. 6.6. The *RSS* values have been measured at 6 different time instants, but it is worth to point out that the acquisition time can be further shortened to reach an almost real-time tracking. The samples of the localization maps and the estimated path are reported in Fig. 6.7 and Fig. 6.6, respectively. As it can be observed, there is a good matching between the actual path and the estimated one assessing the effectiveness of the approach in real-time processing, as well. The same analysis has been carried out for the indoor case. Although the moving target is quite carefully localized, the result in Figure 6.8 and the location indexes in Tab. 6.1 confirm the higher complexity of tracking the target as compared to the outdoor case.

6.3.2 Multiple target tracking

In order to deal with the tracking of multiple targets, the *SVM* classifier has been trained with a mixed data-set containing examples with one (T_1 examples with

6.3. EXPERIMENTAL VALIDATION

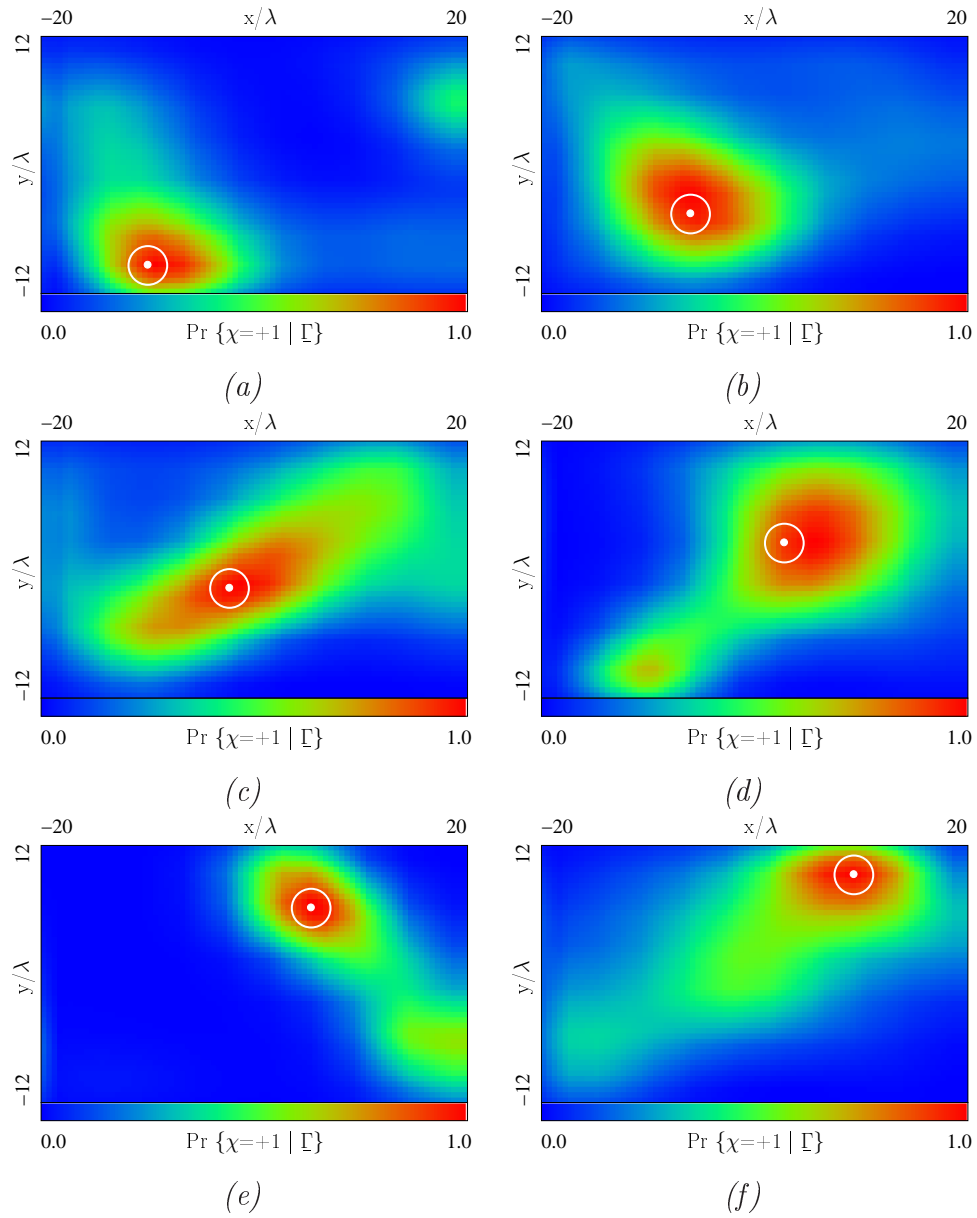


Figure 6.7: *Single target tracking - Outdoor Scenario* - Screenshots of the probability map of the investigation region D acquired during the target motion.

<i>Time Instant</i>	<i>Outdoor</i>		<i>Indoor</i>	
	ρ	$\rho \times \rho_{max} [\lambda]$	ρ	$\rho \times \rho_{max} [\lambda]$
1	0.071	3.32	0.209	9.76
2	0.070	3.30	0.131	6.09
3	0.060	2.78	0.115	5.38
4	0.057	2.67	0.048	2.23
5	0.045	2.09	0.089	4.15
6	0.074	3.46	0.140	6.53
<i>Average Error : $\bar{\rho}$</i>	0.063	2.94	0.122	5.69

Table 6.1: *Single target tracking* - Localization errors for the outdoor and the indoor scenarios.

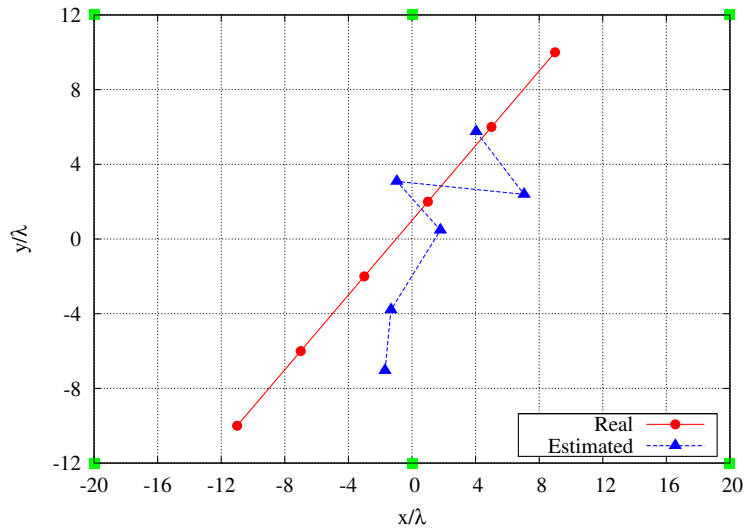


Figure 6.8: *Single target tracking - Indoor Scenario* - Actual and estimated trajectories.

	<i>Single Target</i>		<i>Multiple Target</i>			
	$j = 1$		$j = 1$		$j = 2$	
	ρ	$\rho \times \rho_{max} [\lambda]$	ρ	$\rho \times \rho_{max} [\lambda]$	ρ	$\rho \times \rho_{max} [\lambda]$
(a)	0.044	2.07	0.217	10.12	0.158	7.37
(b)	0.059	2.77	0.196	9.14	0.135	6.31
(c)	0.093	4.34	0.151	7.02	0.074	3.44
(d)	0.150	6.98	0.149	6.96	0.062	2.91
(e)	0.262	12.23	0.063	2.93	0.106	4.94
(f)	0.357	16.67	0.031	1.46	0.063	2.93

Table 6.2: *Multiple target localization - Outdoor Scenario* - Localization errors for the single and multiple target case.

$J = 1$) and two (T_2 examples with $J = 2$) targets. Since $T = T_1 + T_2$ examples have been used also for the single-target training, some experiments have been carried out to analyze the dependence of the localization on the percentage of training samples from T_1 and T_2 . The probability maps in Fig. 6.9 show that the position of one target can be correctly located although a smaller set of single-target examples has been used for the training phase (i.e., $T_1 < T_2$). Vice versa, a larger number of example is needed for an effective localization of the two targets as pointed out by the maps in Fig. 6.10 and quantified by the location indexes in Tab. 6.2. Such a behavior was expected since the number of different combinations with two targets is higher if compared to the single-target case. Therefore, $T_1 = 150$ and $T_2 = 350$ examples have been successively used for the training phase of the following tracking experiments.

As representative examples, two different situations with $J = 2$ have been dealt with. In the former, one target ($j = 1$) is moving within D while the other ($j = 2$) remains immobile in the same position. Instead, both targets are moving in the second example. The actual trajectory and the estimated one are shown in Fig. 6.11 and Fig. 6.12, respectively. Whatever the example at hand, a quite careful indication on the position and path followed by the targets has been obtained as further confirmed by the average values of the localization errors (outdoor: $\bar{\rho}_1 = 0.070$, $\bar{\rho}_2 = 0.061$ - indoor: $\bar{\rho}_1 = 0.101$, $\bar{\rho}_2 = 0.070$).

6.4 Discussions

The localization and tracking of passive targets have been addressed by exploiting the RSS values available at the nodes of a WSN . The problem at hand has been reformulated into an inverse source one aimed at reconstructing the support of an equivalent source generating a perturbation of the wireless links among the WSN nodes equal to that due to the presence of targets within the monitored

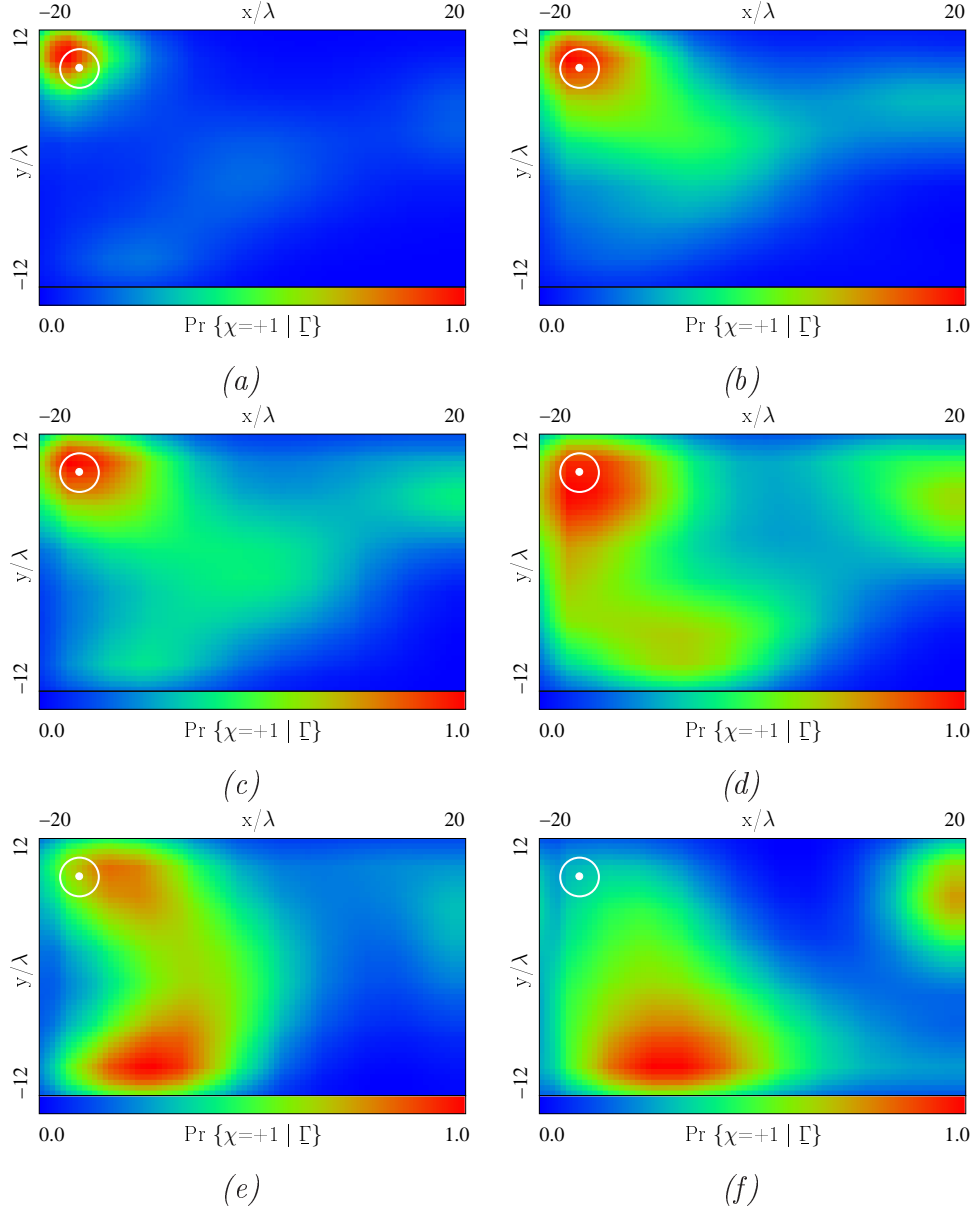


Figure 6.9: *Single target localization - Outdoor Scenario* ($T_1 \in [0, 500]$, $T_2 \in [0, 500]$, $\lambda = 100$, $C = 60$) - Probability maps of the investigation region D when using (a) 100% T_1 and 0% T_2 , (b) 80% T_1 and 20% T_2 , (c) 60% T_1 and 40% T_2 , (d) 40% T_1 and 60% T_2 , (e) 20% T_1 and 80% T_2 , and (f) 0% T_1 and 100% T_2 of samples in the training phase.

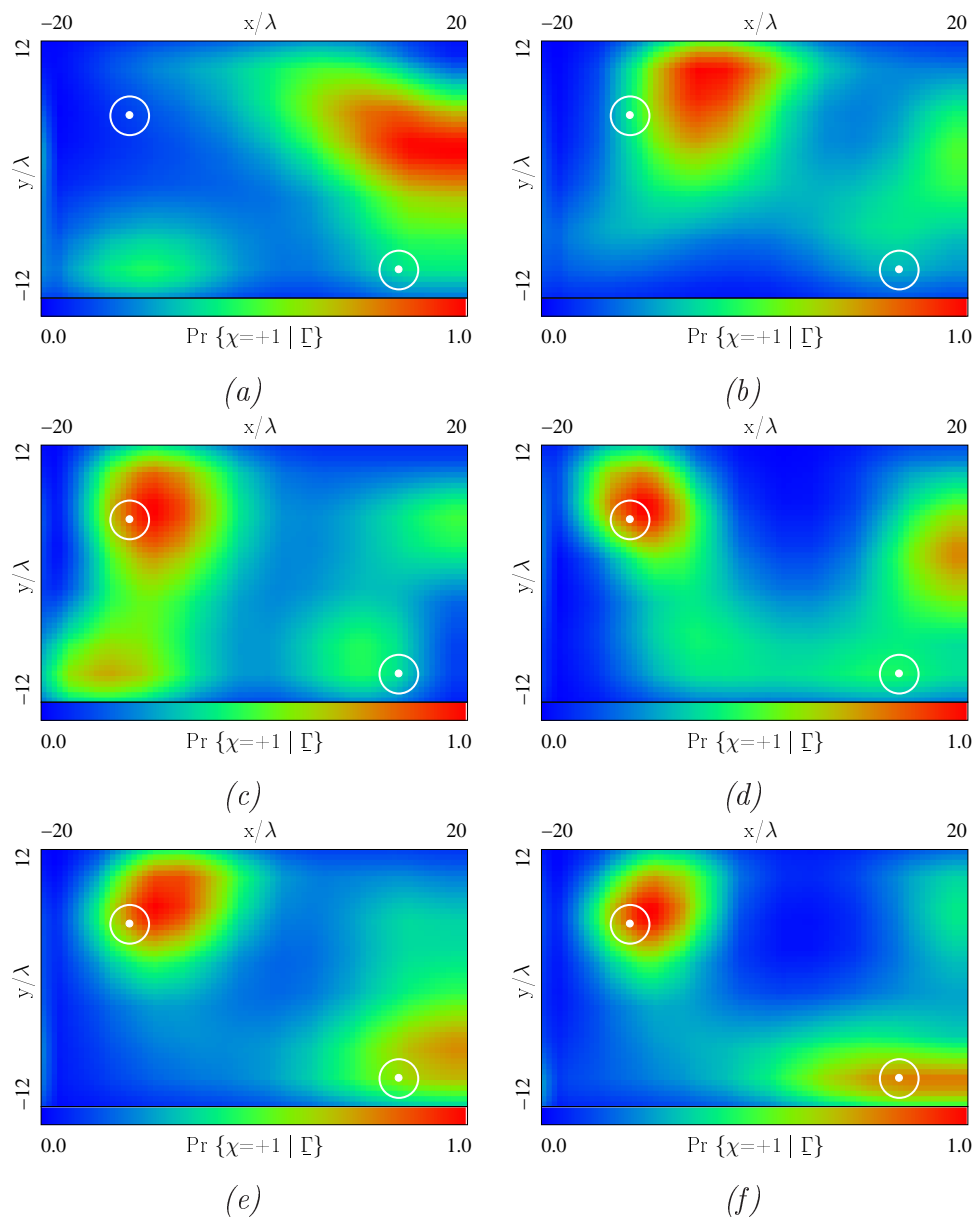


Figure 6.10: *Multiple targets localization - Outdoor Scenario* ($T_1 \in [0, 500]$, $T_2 \in [0, 500]$, $\lambda = 100$, $C = 60$) - Probability maps of the investigation region D when using (a) 100% T_1 and 0% T_2 , (b) 80% T_1 and 20% T_2 , (c) 60% T_1 and 40% T_2 , (d) 40% T_1 and 60% T_2 , (e) 20% T_1 and 80% T_2 , and (f) 0% T_1 and 100% T_2 of samples in the training phase.

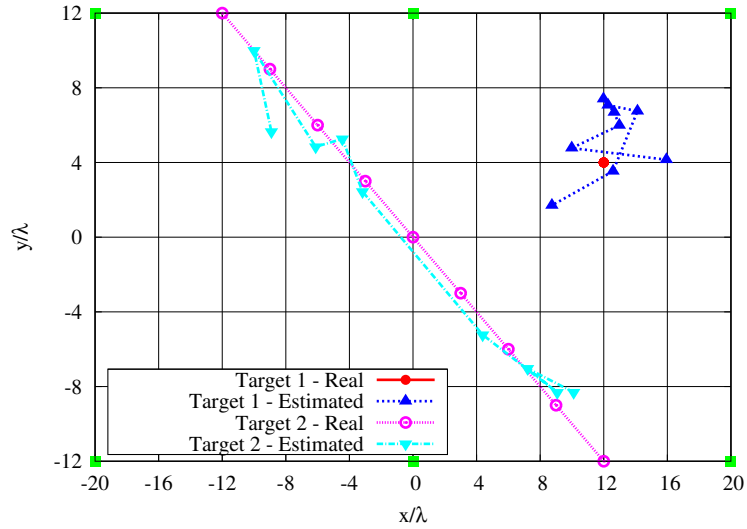


Figure 6.11: *Multiple targets tracking - Outdoor Scenario - Actual and estimated trajectories.*

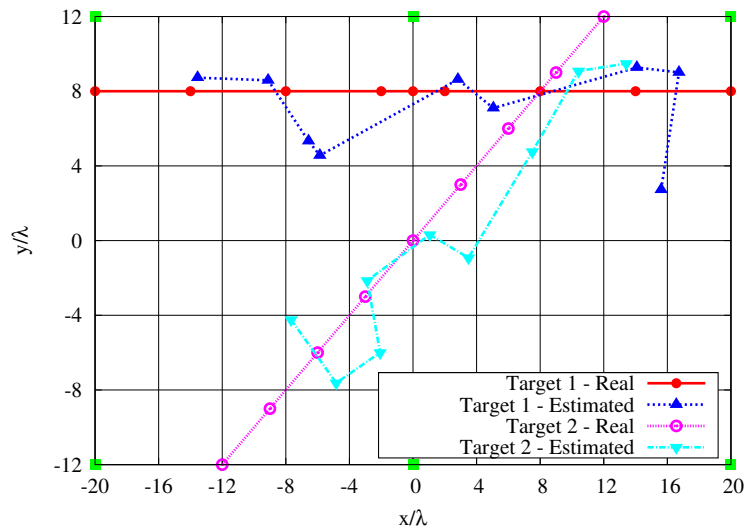


Figure 6.12: *Multiple targets tracking - Outdoor Scenario - Actual and estimated trajectories.*

6.4. DISCUSSIONS

area. The inversion has been faced with a learning-by-examples approach based on a *SVM* classifier devoted to determine a map of the *a-posteriori* probability that a differential equivalent source is present within the investigation domain. Experimental results have assessed the effectiveness and reliability of the proposed approach in dealing with the tracking of single and multiple human beings both in indoor and outdoor environments.

Chapter 7

Conclusions and Future Developments

In this last section, some conclusions are drawn and further advances are envisaged in order to address the possible developments of the proposed technique.

In this thesis, a classification approach for real-time solution of complex electromagnetic problems has been proposed. A suitable SVM-based strategy has been developed for determining the probability of presence and the position of targets starting from the definition of a “risk map” of the considered domain. The effectiveness of the approach has been assessed by considering different application fields, starting from the buried object detection (Chapter 3) up to the passive tracking of targets moving throughout the monitored area (Chapter 6). The obtained results confirmed the generalization capabilities of the method in detecting and locating multiple targets as well as in estimating the presence and the direction of arrival of interferences (Chapter 5). Concerning the methodological novelties of this work, the main contribution is concerned with the following issues:

- the integration of a SVM-based classifier with an iterative multi-scaling procedure to improve resolution accuracy;
- the reliability in dealing with real experiments and three-dimensional scenarios;
- the flexibility in the solution of time-varying scenarios as for the online tracking of moving targets;

Future works, current under development, will be devoted to fully exploit the key-features of the approach as well as to increase autonomy by enabling the system to adapt to changing circumstances. In such a framework, the possibility to move in an autonomous context requires that the proposed approach will be able to adjust itself to allow high flexibility to dynamic and unexpected situations. Incremental learning strategies will be investigated as an on-line method to construct the solution recursively.

References

- [1] B. Scholkopf and A. Smola, *Learning with Kernels*. Cambridge, MA:MIT Press, 2002.
- [2] K. Belkebir, R. E. Kleinman, and C. Pichot, "Microwave imaging-location and shape reconstruction from multifrequency scattering data," *IEEE Trans. on Microwave Theory and Techniques*, vol. 45, pp. 469-476, Apr. 1997.
- [3] S. Caorsi, A. Massa, and M. Pastorino, "A computational technique based on a real-coded genetic algorithm for microwave imaging purposes," *IEEE Trans. on Geoscience and Remote Sensing*, vol. 38, pp. 1697-1708, Jul. 2000.
- [4] R. Mydur and K. A. Michalski, "A neural network approach to the electromagnetic imaging of elliptic conducting cylinders," *Microwave and Optical Technology Lett.*, vol. 28, pp. 303-306, Mar. 2001.
- [5] I. T. Rekanos, "Online inverse scattering of conducting cylinders using radial-basis functions neural networks," *Microwave and Optical Technology Lett.*, vol. 28, pp. 378-380, Mar. 2001.
- [6] V. Vapnik, *Statistical Learning Theory*. Wiley & Sons, 1998.
- [7] Ch. Christodoulou and M. Georgiopoulos. *Application of Neural Networks in Electromagnetics*, Norwood: Artech House, 2001.
- [8] T. Evgeniou, M. Pontil, and T. Poggio, "Regularization networks and support vector machines," in *Advances in Large Margin Classifiers*, A. J. Smola, P. L. Bartlett, B. Scholkopf, and D. Schuurmans (Eds.), MA: MIT Press, 2000.
- [9] Y. Lin, Y. Lee, and G. Wahba, "Support vector machines for classification in nonstandard situations," *Tech. Rep. Univ. Wisconsin-Madison - Dept. Statistics*, no. 1016, 2000.

REFERENCES

- [10] K. Morik, P. Brockhausen, and T. Joachims, "Combining statistical learning with a knowledge-based approach: a case study in intensive care monitoring", *Proc. of the 16th Int. Conf. on Machine Learning*, MA: MIT Press., 1999.
- [11] N. Cristianini and J. Shawe-Taylor. *An Introduction to Support Vector Machines*. Cambridge: University Press, 2000.
- [12] V. N. Vapnik. *The Nature of Statistical Learning Theory*, New York: John Wiley & Sons, 1999.
- [13] J. Platt, "Fast training of support vector machines using sequential minimal optimization," in *Advances in Kernel methods - Support Vector Learning*, B. Scholkopf, C. J. C. Burges, and A. J. Smola (Eds.), MA: MIT Press, 1999.
- [14] K. -R. Muller, S. Mika, G. Ratsch, K. Tsuda, and B. Schölkopf, "An introduction to Kernel-Based Learning Algorithms," *IEEE Trans. on Neural Networks*, vol. 12, no. 2, pp. 181-201, Mar. 2001.
- [15] G. Wahba, "Support vector machines, reproducing kernel Hilbert spaces and the randomized GACV," in *Advances in Kernel methods - Support Vector Learning*, B. Scholkopf, C. J. C. Burges, and A. J. Smola (Eds.), MA: MIT Press, 1999.
- [16] T. Hastie and R. Tibshirani, "Classification by pairwise coupling". Technical Report, Stanford University and University of Toronto, 1996 (<http://www.stat.stanford.edu/trevor/Papers/2class.ps>).
- [17] J. Platt, "Probabilistic outputs for support vector machines and comparison to regularized likelihood methods," in *Advances in Large Margin Classifiers*, A. J. Smola, P. Bartlett, B. Scholkopf, D. Schuurmans (Eds.), MA: MIT Press, 1999.
- [18] H.-T. Lin, C.-J. Lin, and R. C. Weng, "A note on Platt's probabilistic outputs for support vector machines," May 2003, available at <http://www.csie.ntu.edu.tw/~cjlin/>.
- [19] Y. Yu, and L. Carin, "Three-dimensional Bayesian inversion with application to subsurface sensing," *IEEE Trans. Geosci. Remote Sens.*, vol. 45, no. 5, pp. 1258-1270, May 2007.
- [20] R. Firoozabadi, E. L. Miller, C. M. Rappaport, and A. W. Morgenthaler, "Subsurface sensing of buried objects under randomly rough surface using scattered electromagnetic field data," *IEEE Trans. Geosci. Remote Sens.*, vol. 45, no.1, pp. 104-117, Jan. 2007.

-
- [21] E. L. Miller, M. Kilmer, and C. M. Rappaport, "A new shape-based method for object localization and characterization from scattered field data," *IEEE Trans. Geosci. Remote Sens.*, vol. 38, no. 4, pp. 1682-1696, Jul. 2000.
- [22] T. Dogaru and L. Carin, "Time-domain sensing of targets buried under a rough air-ground interface," *IEEE Trans. Antennas Propag.*, vol. 46, no. 3, pp. 360-372, Mar. 1998.
- [23] E. Pasolli, F. Melgani, and M. Donelli, "Automatic analysis of GPR images: a pattern recognition approach," *IEEE Trans. Geosci. Remote Sens.*, vol. 47, no. 7, pp. 2206-2217, Jul. 2009.
- [24] T. J. Cui, Y. Qin, Y. Ye, J. Wu, G. L. Wang, and W. C. Chew, "Efficient low-frequency inversion of 3-D buried objects with large contrasts," *IEEE Trans. Geosci. Remote Sens.*, vol. 44, no. 1, pp. 3-9, Jan. 2006.
- [25] I. Catapano, L. Crocco, and T. Isernia, "Improved sampling methods for shape reconstruction of 3-d buried targets," *IEEE Trans. Geosci. Remote Sens.*, vol. 46, no. 10, pp. 3265-3273, Oct. 2008.
- [26] Q. Liu, X. Liao, and L. Carin, "Detection of unexploded ordnance via efficient semisupervised and active learning," *IEEE Trans. Geosci. Remote Sens.*, vol. 46, no. 9, pp. 2558-2567, Sept. 2008.
- [27] N. Geng, K. E. Baum, and L. Carin, "On the low-frequency natural response of conducting and permeable targets," *IEEE Trans. Geosci. Remote Sens.*, vol. 37, no. 1, pp. 347-359, Jan. 1999.
- [28] K. C. Ho, L. Carin, P. D. Gader, and J. N. Wilson, "An investigation of using the spectral characteristics from ground penetrating radar for landmine/clutter discrimination," *IEEE Trans. Geosci. Remote Sens.*, vol. 46, no. 4, pp. 1177-1191, Apr. 2008.
- [29] M.E. Kilmer, E. L. Miller, D. A. Boas, and D. Brooks, "A shape-based reconstruction technique for DPDW data, Invited paper," *Opt. Express*, vol. 7, no. 13, pp. 481-491, Dec. 2000.
- [30] D. Anguita, A. Boni, and S. Ridella, "A digital architecture for support vector machines: theory, algorithm and FPGA implementation," *IEEE Trans. Neural Netw.*, vol. 14, no. 5, pp. 993-1009, Sept. 2003.
- [31] B. Wohlberg, D. M. Tartakovsky, and A. Guadagnini, "Subsurface characterization with support vector machine," *IEEE Trans. Geosci. Remote Sens.*, vol. 44, no. 1, pp. 47-57, Jan. 2006.

REFERENCES

- [32] B. Scheers, M. Piette, and A. V. Vorst, "The detection of ap mines using UWB GPR," *2nd Int. Conf. detection of abandoned land mines*, pp. 50-54, Oct. 1998.
- [33] A. Aliamiri, J. Stalnaker, and E. L. Miller, "Statistical classification of buried unexploded ordnance using nonparametric prior models," *IEEE Trans. Geosci. Remote Sens.*, vol. 45, no. 9, pp. 2794-2806, Sept. 2007.
- [34] Y. Zhang, L. Collins, H. Yu, C. E. Baum, and L. Carin, "Sensing of unexploded ordnance with magnetometer and induction data: theory and signal processing," *IEEE Trans. Geosci. Remote Sens.*, vol. 41, no. 5, pp. 1005-1015, May 2003.
- [35] B. Zhang, K. O'Neill, J. A. Kong, and T. M. Grzegorzczuk, "Support vector machine and neural network classification of metallic objects using coefficients of the spheroidal MQS response modes," *IEEE Trans. Geosci. Remote Sens.*, vol. 46, no. 1, pp. 159-171, Jan. 2008.
- [36] S. Caorsi, D. Anguita, E. Bermani, A. Boni, M. Donelli, and A. Massa, "A comparative study of NN and SVM-based electromagnetic inverse scattering approaches to on-line detection of buried objects," *J. Appl. Comput. Electromagn. Soc.*, vol. 18, no. 2, pp. 1-11, Jul. 2003.
- [37] E. Bermani, A. Boni, S. Caorsi, and A. Massa, "An innovative real-time technique for buried object detection," *IEEE Trans. Geosci. Remote Sens.*, vol. 41, no. 4, pp. 927-931, Apr. 2003.
- [38] A. Massa, A. Boni, and M. Donelli, "A classification approach based on SVM for electromagnetic subsurface sensing," *IEEE Trans. Geosci. Remote Sens.*, vol. 43, no. 9, pp. 2084-2093, Sept. 2005.
- [39] M. S. Bazaraa, H. D. Sherali, and C. M. Shetty. *Nonlinear programming: theory and algorithms*. Wiley, second ed., 1993.
- [40] H.-T. Lin, C.-J. Lin, and R. C. Weng, "A note on Platt's probabilistic outputs for support vector machines," *Machine Learning*, vol. 68, no. 3, pp. 267-276, Oct. 2007.
- [41] A. A. Lestari, A. G. Yarovoy, and L. P. Ligthart, "Ground influence on the input impedance of transient dipole and bow-tie antennas," *IEEE Trans. Antennas Propagat.*, vol. 52, no. 8, pp. 1970-1975, Aug. 2004.
- [42] V. Kovalenko, A. G. Yarovoy, and L. P. Ligthart, "A novel clutter suppression algorithm for landmine detection with GPR," *IEEE Trans. Geosci. Remote Sens.*, vol. 45, no. 11, pp. 3740-3751, Nov. 2007.

-
- [43] W. R. Scott and G. S. Smith, "Measured electrical constitutive parameters of soil as functions of frequency and moisture content," *IEEE Trans. Geosci. Remote Sens.*, vol. 30, no. 3, pp. 621-623, May 1992.
- [44] Committee on Technologies for the Early Detection of Breast Cancer, *Mammography and Beyond: Developing Technologies for the Early Detection of Breast Cancer*, S. Nass, I. Henderson, and J. Lashof, Eds. Washington, DC: Nat. Cancer Policy Board, Inst. Med., Commission Life Stud, Nat. Res. Council, 2001.
- [45] E. Zastrow, S. Davis, and S. Hagness, "Safety assessment of breast cancer detection via ultrawideband microwave radar operating in pulsed-radiation mode," *Microw. Opt. Technol. Lett.*, vol. 49, no. 1, pp. 221-225, Jan. 2007.
- [46] P. Meaney, M. Fanning, D. Li, S. Poplack, and K. Paulsen, "A clinical prototype for active microwave imaging of the breast," *IEEE Trans. Microw. Theory Tech.*, vol. 48, no. 11, pp. 1841-1853, Nov. 2000.
- [47] E. J. Bond, X. Li, S. C. Hagness, and B. D. Van Veen, "Microwave imaging via space-time beamforming for early detection of breast cancer," *IEEE Trans. Antennas Propag.*, vol. 51, no. 8, pp. 1690-1705, Aug. 2003.
- [48] C. Yu, M. Yuan, J. Stang, E. Bresslour, R. T. George, G. A. Ybarra, W. T. Joines, and Q. H. Liu, "Active microwave imaging II: 3-D system prototype and image reconstruction from experimental data," *IEEE Trans. Microw. Theory Tech.*, vol. 56, no. 4, pp. 991-1000, Apr. 2008.
- [49] T. Rubaek, P. M. Meaney, P. Meincke, and K. D. Paulsen, "Nonlinear microwave imaging for breast-cancer screening using gauss-newton's method and the CGLS inversion algorithm," *IEEE Trans. Antennas Propag.*, vol. 55, no. 8, pp. 2320-2331, Aug. 2007.
- [50] M. El-Shenawee and E. Miller, "Spherical harmonics microwave algorithm for shape and location reconstruction of breast cancer tumor," *IEEE Trans. Med. Imag.*, vol. 25, no. 10, pp. 1258-1271, Oct. 2006.
- [51] S. Caorsi, A. Massa, M. Pastorino, and A. Rosani, "Microwave medical imaging: potentialities and limitations of a stochastic optimization technique," *IEEE Trans. Microw. Theory Tech.*, vol. 52, no. 8, pp. 1909-1916, Aug. 2004.
- [52] D. A. Woten, J. Lusth, and M. El-Shenawee, "Interpreting artificial neural networks for microwave detection of breast cancer," *IEEE Microw. Wireless Compon. Lett.*, vol. 17, no. 12, pp. 825-827, Dec. 2007.

REFERENCES

- [53] A. Takemura, A. Shimizu, K. Hamamoto, "Discrimination of breast tumor in ultrasonic images using an ensemble classifier based on the adaboost algorithm with feature selection," *IEEE Trans. Med. Imag.*, in. press.
- [54] D. Voth, "Using AI to detect breast cancer," *IEEE Intell. Syst.*, vol. 20, no. 1, pp. 5-7, Jan./Feb. 2005.
- [55] X. Li and S. C. Hagness, "A confocal microwave imaging algorithm for breast cancer detection," *IEEE Microw. Wireless Compon. Lett.*, vol. 11, no. 3, pp. 130-132, Mar. 2001.
- [56] W. C. Chew, *Waves and Fields in Inhomogeneous media*. Piscataway, NJ: IEEE Press, 1995.
- [57] C. Yu, M. Yuan, J. Stang, E. Bresslour, R. T. George, G. A. Ybarra, W. T. Joines, and Q. H. Liu, "Active microwave imaging II: 3-D system prototype and image reconstruction from experimental data," *IEEE Trans. Microw. Theory Tech.*, vol. 56, no. 4, pp. 991-1000, Apr. 2008.
- [58] H.-T. Lin, C.-J. Lin, and R. C. Weng, "A note on Platt's probabilistic outputs for support vector machines," *Machine Learning*, vol. 68, no. 3, pp. 267-276, Oct. 2007.
- [59] S. Caorsi, M. Donelli, D. Franceschini, and A. Massa, "A new methodology based on an iterative multiscaling for microwave imaging," *IEEE Trans. Microw. Theory Tech.*, vol. 51, no. 4, pp.1162-1173, Apr. 2003.
- [60] T. Rubaek, P. M. Meaney, P. Meincke, and K. D. Paulsen, "Nonlinear microwave imaging for breast-cancer screening using Gauss-Newton's method and the CGLS inversion algorithm," *IEEE Trans. Antennas Propag.*, vol. 55, no. 8, pp. 2320-2332, Aug. 2007.
- [61] M. Chryssomallis, "Smart antennas," *IEEE Antennas Propag. Mag.*, vol. 42, no. 3, pp. 129-136, Jun. 2000.
- [62] E. L. Hines, M. S. Leeson, M. M. Ramon, M. Pardo, E. Llobet, D. D. Iliescu, and J. Yang, *Intelligent Systems: Techniques and Applications*. Shaker publishing, 2008.
- [63] S. P. Applebaum, "Adaptive arrays," *IEEE Trans. Antennas Propag.*, vol. 24, no. 5, pp. 585-598, May 1976.
- [64] D. S. Weile and E. Michielssen, "The control of adaptive antenna arrays with genetic algorithms using dominances and diploidy," *IEEE Trans. Antennas Propag.*, vol. 49, no. 10, pp. 1424-1433, Oct. 2003.

-
- [65] R. Roy and T. Kailath, "ESPRIT-Estimation of signal parameters via rotational invariance techniques," *IEEE Trans. Acust., Speech, Signal Process.*, vol. 37, no. 7, pp. 984-995, Jul. 1989.
- [66] F. Gao and B. Gershman, "A generalized ESPRIT approach to direction-of-arrival estimator," *IEEE Signal Process. Lett.*, vol. 12, no. 3, pp. 254-257, Mar. 2005.
- [67] M. D. Zoltowski, M. Haardt, and C. P. Mathews, "Closed-form 2-D angle estimation with rectangular arrays in element space or beamspace via unitary ESPRIT," *IEEE Trans. Signal Process.*, vol. 44, no. 2, pp. 316-328, Feb. 1996.
- [68] R. O. Schmidt, "Multiple emitter location and signal parameter estimation," *IEEE Trans. Antennas Propag.*, vol. 34, no. 3, pp. 276-280, Mar. 1986.
- [69] A. Swindlehurst and T. Kailath, "A performance analysis of sub space-based methods in the presence of model errors. I. The MUSIC algorithm," *IEEE Trans. Signal Process.*, vol. 40, no. 7, pp. 1578-1774, Jul. 1992.
- [70] I. Ziskind and M. Wax, "Maximum likelihood localization of multiple sources by alternating projection," *IEEE Trans. Acust., Speech, Signal Process.*, vol. 36, no. 10, pp. 1553-1560, Oct. 1988.
- [71] P. Stoica and A. B. Gershman, "Maximum-likelihood DOA estimation by data-supported grid search," *IEEE Signal Process. Lett.*, vol. 6, no. 10, pp. 273-275, Oct. 1999.
- [72] A. H. El Zooghby, C. G. Christodoulou, and M. Georgiopoulos, "Performance of radial-basis function networks for direction of arrival estimation with antenna arrays," *IEEE Trans. Antennas Propag.*, vol. 45, no. 11, pp. 1611-1617, Nov. 1997.
- [73] A. H. El Zooghby, C. G. Christodoulou, and M. Georgiopoulos, "A neural network-based smart antenna for multiple source tracking," *IEEE Trans. Antennas Propag.*, vol. 48, pp. 768-776, May 2000.
- [74] M. Martinez-Ramon and C. G. Christodoulou, *Support Vector Machines for Antenna Array Processing and Electromagnetics*. Synthesis Lectures on Computational Electromagnetics Lecture #5, Morgan & Claypool Publishers, 2006.
- [75] E. Bermani, A. Boni, S. Caorsi, M. Donelli, and A. Massa, "A multi-source strategy based on a learning-by-examples technique for buried object detection," *Progress In Electromagnetic Research, PIER*, vol. 48, pp. 185-200, 2004.

REFERENCES

- [76] D. Anguita, A. Boni, and S. Ridella, "A digital architecture for support vector machines: theory, algorithm and FPGA implementation," *IEEE Trans. Neural Netw.*, vol. 14, no. 5, pp. 993-1009, Sep. 2003.
- [77] M. Pastorino and A. Randazzo, "A smart antenna system for direction of arrival estimation based on a support vector regression," *IEEE Trans. Antennas Propag.*, vol. 53, no. 7, pp. 2161-2168, Jul. 2005.
- [78] M. Pastorino and A. Randazzo, "The SVM-based smart antenna for estimation of the directions of arrival of electromagnetic waves," *IEEE Trans. Instrum. Meas.*, vol. 55, no. 6, pp. 1918-1925, Dec. 2006.
- [79] A. Randazzo, M. A. Abou-Khousa, M. Pastorino, and R. Zoughi, "Direction of arrival estimation based on support vector regression: experimental validation and comparison with MUSIC," *IEEE Trans. Antennas Wireless Propag. Lett.*, vol. 6, pp. 379-382, 2007.
- [80] S. Caorsi, M. Donelli, D. Franceschini, and A. Massa, "A new methodology based on an iterative multiscaling for microwave imaging," *IEEE Trans. Microw. Theory Tech.*, vol. 51, no. 4, pp.1162-1173, Apr. 2003.
- [81] L. C. Godara, "Applications of antenna arrays to mobile communications - Part I: Performance improvement, feasibility, and system considerations," *Proc. IEEE*, vol. 85, pp. 1031-1060, Jul. 1997.
- [82] C.A. Balanis, *Antenna theory: Analysis and design*. New York: Wiley, 2005.
- [83] A. Manikas, A. Alexiou, H. R. Karimi, "Comparison of the ultimate direction-finding capabilities of a number of planar array geometries," *IEE Proc. Radar, Sonar Navig.*, vol. 144, no. 6, pp. 321-329, Dec. 1997.
- [84] C. G. Christodoulou and M. Georgiopoulos, *Applications of Neural Networks in Electromagnetics*. Artech House Inc., Boston, MA, USA, 2001.
- [85] W. Chen, J. Jen, and S. M. Zhang, "Planar dipole arrays with equal element input impedances," *Electron. Lett.*, vol. 31, no. 24, pp. 2061-2062, 1995.
- [86] C.-Y. Chong and S. P. Kumar, "Sensor networks: evolution, opportunities, and challenges," *Proc. IEEE*, vol. 91, no. 8, pp. 1247-1256, Aug. 2003.
- [87] Z. Li, W. Dehaene, and G. Gielen, "A 3-tier UWB-based indoor localization system for ultra-low-power sensor networks" *IEEE Trans. Wireless Commun.*, vol. 8, no. 6, pp. 2813-2818, Jun. 2009.
- [88] G. Latsoudas and N. D. Sidiropoulos, "A fast and effective multidimensional scaling approach for node localization in wireless sensor networks,"

-
- IEEE Trans. Geosci. Remote Sens.*, vol. 55, no. 10, pp. 5121-5127, Oct. 2007.
- [89] C.-T. Huang, C.-H. Wu, Y.-N. Lee and J.-T. Chen, "A novel indoor RSS-based position location algorithm using factor graphs," *IEEE Trans. Wireless Commun.*, vol. 8, no. 6, pp. 3050-3058, Jun. 2009.
- [90] K. Pahlavan, X. Li, and J. P. Makela, "Indoor geolocation science and technology," *IEEE Commun. Mag.*, vol. 40, no. 2, pp. 112-118, Feb. 2002.
- [91] A. Catovic, and Z. Sahinoglu, "The Cramer-Rao bounds of hybrid TOA/RSS and TDOA/RSS location estimation schemes," *IEEE Commun. Lett.*, vol. 8, no. 10, pp. 626-628, Oct. 2004.
- [92] X. Li, "RSS-based location estimation with unknown pathloss model," *IEEE Trans. Wireless Commun.*, vol. 5, no. 12, pp. 3626-3633, Dec. 2006.
- [93] X. Li, "Collaborative localization with received-signal strength in wireless sensor networks," *IEEE Trans. Veh. Technol.*, vol. 56, no. 6, pp. 3807-3817, Nov. 2007.
- [94] F. Cabrera-Mora and J. Xiao, "Preprocessing technique to signal strength data of wireless sensor network for real-time distance estimation," *2008 IEEE Int. Conf. Robotics Automation*, Pasadena, CA, USA, May 19-23, 2008, pp. 1537-1542.
- [95] M. Saxena, P. Gupta, B. N. Jain, "Experimental analysis of RSSI-based location estimation in wireless sensor networks," *2008 IEEE Conf. Commun. System Software and Middleware (COMSWARE)*, Bangalore, India, pp. 503-510, Jan. 2008.
- [96] W. Butler, "Design considerations for intrusion detection wide area surveillance radars for perimeters and borders," *2008 IEEE Int. Conf. Tech. Homeland Security*, Waltham, MA, USA, May 12-13, 2008, pp. 47-50.
- [97] A. S. Bugaev, V. V. Chapurski, S. I. Ivashov, V. V. Razevig, A. P. Sheiko, and I. A. Vasilyev, "Through wall sensing of human breathing and heart beating by monochromatic radar," *2004 Int. Conf. Ground Penetrating Radar*, Delft, Netherlands, Jun. 21-24, 2004, vol. 1, pp. 291-294.
- [98] P. Withington, H. Fluhler, and S. Nag, "Enhancing homeland security with advanced UWB sensors," *IEEE Microw. Mag.*, vol. 4, no. 3, pp. 51- 58, Sept. 2003.
- [99] F. Viani, L. Lizzi, P. Rocca, M. Benedetti, M. Donelli, and A. Massa, "Object tracking through RSSI measurements in wireless sensor networks," *Electron. Lett.*, vol. 44, no. 10, pp. 653-654, 2008.

REFERENCES

- [100] W. C. Chew, *Waves and Fields in Inhomogeneous Media*. New York: Van Nostrand Reinhold, 1990.
- [101] A. Ishimaru, *Electromagnetic Wave, Propagation, Radiation and Scattering*. Englewood Cliffs, NJ: Prentice-Hall, 1991.
- [102] K. Morik, P. Brockhausen, and T. Joachims, “Combining statistical learning with a knowledge-based approach - A case study in intensive care monitoring,” *1999 Int. Conf. Machine Learn. (ICML 1999)*, June 27-30, 1999, Bled, Slovenia, pp. 268-277.